On The Removal of Material for Polishing Aspheric Optics

A Thesis Submitted for the Degree

of

Doctor of Philosophy of the University of London

by

Do Hyung Kim

Optical Science Laboratory

Department of Physics and Astronomy

University College

University of London

2000

ProQuest Number: U644140

All rights reserved

INFORMATION TO ALL USERS
The quality of this reproduction is dependent upon the quality of the copy submitted.

In the unlikely event that the author did not send a complete manuscript
and there are missing pages, these will be noted. Also, if material had to be removed,
a note will indicate the deletion.

ProQuest U644140

Published by ProQuest LLC(2016). Copyright of the Dissertation is held by the Author.

All rights reserved.
This work is protected against unauthorized copying under Title 17, United States Code.
Microform Edition © ProQuest LLC.

ProQuest LLC
789 East Eisenhower Parkway
P.O. Box 1346
Ann Arbor, MI 48106-1346

To my Family

Abstract

Spherical surfaces for precision optical instruments have long been preferred over aspheric surfaces due to ease of manufacture. Aspheric surfaces have been far more difficult to manufacture despite known advantages in system performance, size, and weight. Lack of generic testing methods, and non-deterministic nature of optical polishing process are still the main hurdles to cost-effective aspheric surfaces. However, recent developments in testing and manufacturing techniques are gradually stimulating the use of aspherics. The thesis starts with a historical review of optical manufacturing methods. The main body of the thesis explores theoretical and experimental work towards efficient polishing of aspheric surfaces. Firstly, material removal experiments using a sub-diameter pitch tool under active control are described, investigating the relationship between the removal rate and mechanical polishing parameters. Secondly, the characteristics of spinning compliant tools for rapid aspheric production are investigated, and the feasibility of using the spinning compliant tool for efficient aspheric polishing is assessed. Thirdly, a numerical index representing the manufacturing difficulty for aspheric is reviewed and further developed. The thesis concludes with an overview of the prospects for the manufacture and use of aspherics in the future, together with the research required to make this a reality.

Contents

List of Tables

List of Figures

Glossary

AIP	American Institute of Physics
CCD	Charge-Coupled Device
CCOS	Computer-Controlled Optical Surfacing by Litton Itek
CCPM	Computer-Controlled Polishing Machine
CGH	Computer-Generated Holography
CIR	Central Intensity Ratio
CMP	Chemical-Mechanical Polishing (Planarisation)
CNC	Computer Numerically Controlled
COM	Center for Optics Manufacturing, Univerity of Rochester
CPSMA	Commission of Physical Sciences, Mathematics, and Application
DIPOS	Dedicated Intelligent Polishing Operation Software by OGL
FEA	Finite Element Analysis
FJP	Fluid Jet Polishing
IDT	Integrated Dwell Time
IOM	Index Of Manufacturability
IR	Infra Red
IRP-600	A CCPM by OGL
KAIST	Korea Advanced Institute of Science and Technology
LVDT	Linear Variable Differential Transformer
MATLAB	A matrix calculation software
MF	Material removal Function
MMT	Multi Mirror Telescope Observatory, The Smithsonian Institution and the University of Arizona

MRF	Magneto-Rheological Finishing by COM and QED
NASA	National Aeronautics and Space Administration
OGL	Optical Generics Limited
OGLP-400	A prototype CCPM by OGL
OPD	Optical Path Difference
OSL	Optical Science Laboratory, Department of Physics and Astronomy, UCL
OTF	Optical Transfer Function
PSI	Phase Shifting Interferometry
QED	A spin-off company from COM
REOSC	A French optics fabrication company
RMS	Root Mean Square
RPM	Rotations Per Minute
SaTReC	Satellite Technology Research Center, KAIST
SCT	Spinning Compliant Tool
SimPol	Simulator for Polishing
SPIE	Society of Photo-optical Instrumentation Engineers
SPDT	Single Point Diamond Turning
TEM	Transmission Electron Microscopy
TNO	Netherlands Organisation for Applied Scientific Research
TPT	Total Polishing Time
UCL	University College London
ULE	Ultra Low Expansion glass ceramic by Corning
UV	Ultra Violet
VLT	Very Large Telescope, ESO

Chapter 1

Introduction

1.1 Background

From the Galilean telescope[59] of the 17th century to the Hubble Space Telescope[69], astronomical telescopes have evolved greatly in terms of the performance to study the heavenly body. Compared to the progress in the performance, the manufacturing technology of optical components does not seem to have progressed as much. Newton[82] was well aware of the fact that optics manufacturing requires highly experienced craftsmanship.

> ... nothing is wanting to perfect these Telescopes but good Workmen who can grind and polish Glasses truly spherical.
> *Sir Isaac Newton, Opticks (1721)*

Manufacturing of a refractive or reflective optical surface essentially consists of two key purposes. One is to remove the workpiece material, converging to a designed surface *form*, and the other is to reduce the surface *roughness*, or more recently referred as surface *texture*, both satisfying the optical tolerances. For manufacturing high precision optics, particularly aspheric surfaces which are the ultimate concern of this thesis, the situation has not changed greatly from the Newton's days. Among the manufacturing processes, the last process of removing material, or optical polishing/figuring, has been regarded arguably as a *craft* rather than a scientific technique due to the indeterministic nature of material removal. Hence, optical polishing and figuring typically requires numerous iterations of polishing and testing. For the past 100 years, many theories were presented to explain the physics of glass polishing, but none so far describes the phenomenon clearly. Today, the most widely accepted perspective is that polishing is a chemical-mechanical process.[60]

Besides the intrinsic difficulties in polishing optics in general, the lack of generic testing methods, and the added complexity in the polishing work, were the main hurdles to manufacturing aspheric optics, despite the inherent advantages of aspheric designs. However, recent developments in testing and manufacturing techniques are gradually stimulating the use of aspherics.

Not only in astronomy, but also in numerous applications such as military, industrial production, space, medical, and optoelectronics, the needs for precision optics including aspheric optics have been ever increasing.[18] Immediate examples other than astronomy are, precision guided munitions, optical measurement systems, satellite remote sensing telescopes, endoscopes, optical telecommunications, and semiconductor lithography machines. The overall market size of various applications integrating precision optics is estimated at $31 billion for 1991, and forecasted to be more than $100 billion by 2001[32], while the size of the world wide aspheric lens market alone is estimated[86] to be at least $200 million in 1999.

1.2 Why aspherics?

Aspheric optics can be defined as any optical surface that is non-spherical (a flat is a special case of a sphere with $R = \infty$). Traditionally, aspheres referred were to mostly on-axis or off-axis conic sections or conic sections with higher order polynomials. However, as optics design and manufacturing techniques evolve, non-rotationally symmetric surfaces such as saddle-shaped surfaces are also emerging as important aspheres. These find application, e.g. in television projection systems.

By using aspheric surfaces, the image defects caused by spherical surfaces such as coma, astigmatism, and distortions, can be avoided, with resulting advantages such as an improved OTF(Optical Transfer Function) or the realisation of particular field curvatures.[32, 37] The reason aspheric optics can increase the optical system performance is that the aspheric terms give mathematically more degrees of freedom for the

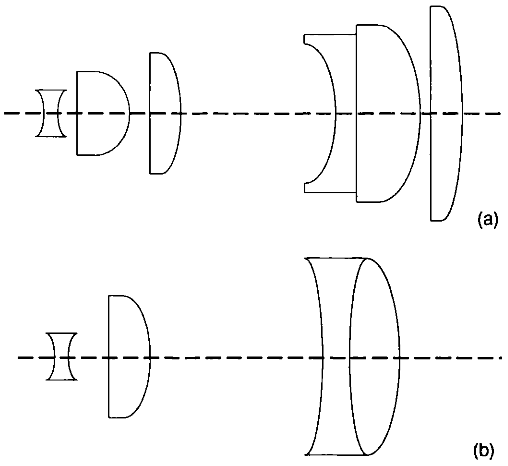

Figure 1.1: Comparison of (a) spherical and (b) aspheric designs for a Galilean telescope (designed by R. Bingham, OSL)

optimisation. The addition of definable high order terms to the usual second-order spherical surface permits independent correction or balancing of various aberrations.

The number of surfaces can be reduced when using aspheric surfaces, which is essential to making hardware lighter and more compact. It is crucial to reduce the weight and size of the optics in projects such as space camera or any hand-held system. As the number of surfaces is reduced, the loss caused by unwanted surface reflections is also reduced. One drawback with aspheres is the increased sensitivity to misalignment, but it can be largely avoided through good optomechanical design and fixturing.

Figure 1.1 illustrates an example of an all-spherical lens design (a) and an aspheric-included design (b), and the two designs give virtually identical optical system performances. The aspheric design (b) shows clear advantages in the number of elements, thus the system size and weight.

Nevertheless, despite all the advantages, spherical surfaces historically have long been preferred over aspheric surfaces due to ease of manufacture. The complexity of the optical form has made aspheres difficult to produce, thus more time-consuming and costly. Aspheric surfaces require sub-diameter tools due to the varying radius of curvature, which slow the polishing process. The characteristic that makes an asphere useful in optical design is the very cause of the manufacturing difficulties. Only relatively affluent projects such as large astronomy telescopes or military reconnaissance systems could afford high precision aspheric optics in the past.

Today, the story is beginning to change thanks to many efforts to develop techniques to produce affordable high precision aspherics. Single Point Diamond Turning (SPDT) machines are already being used to produce aspheric infrared optics[32] which require less accuracy in the surface texture, and computer-controlled diamond grinding machines are being commercialised[96] to grind aspheric surfaces. Computer-controlled polishing machines using compliant materials[34] as the polishing tool are also being developed as well as the spinning compliant tool polishing technique demonstrated in this thesis. Low to medium precision molded plastic or glass aspheres are being produced, since one aspheric mould can produce a large number of lenses, e.g. in low-end commercial cameras. Testing of aspheric surface is also a crucial but less developed area, and various approaches[77, 58] are under research.

1.3 Author's contributions and summary of the thesis

The work in this thesis deals with the development of techniques to polish relatively small aspheric optics efficiently. The contents of the thesis can be largely divided into two parts. The first half is regarding the theoretical and empirical work for pitch tool polishing, and the second half is concerning the polishing demonstration of a novel concept of tool, which is *spinning* in order to give high removal rate, and *compliant* for conformality to aspheric surfaces.

When the author joined OSL (Optical Science Laboratory) in the Department of Physics and Astronomy, UCL (University College London) in October 1995, the preliminary work in pitch tool optical polishing on an optical glass had been undertaken by Dr. S.-W. Kim[54], then the honorary research fellow of OSL. Part of the work in this thesis is a continuing investigation in material removal of pitch tool polishing in OSL. The research on rapid material removal with novel spinning compliant tool was possible with the cooperation from OGL (Optical Generics Limited), a spin-off company from OSL, which specialises in computer-controlled optical polishing machines.

The work in this thesis was funded by SaTReC (Satellite Technology Research Centre), KAIST (Korea Advanced Institute of Science and Technology), as an international joint research program between UCL and KAIST. Contributions to the research were also made by UK Higher Education Funding Council for the optical testing apparatus.

1.3.1 Author's contributions

The author has made the following contributions in this research.

Comparisons are made for the state-of-the-art techniques in aspheric optics polishing.

A systematic material removal experiment using the active pressure servo mode with a sub-diameter pitch tool was carried out by using a CCPM (Computer-Controlled Polishing Machine)[85]. During the pitch tool polishing experiment, the data reduction and analysis routines of the testing data from the static interferometric testing were developed, and the initial surfaces were prepared by hand polishing. From the extensive pitch tool polishing experiment, the minimum prediction accuracy was calculated for a point on the surface.

Based on the pitch tool polishing, the requirements for a novel concept of polishing tool for aspheric polishing, the spinning compliant tool were defined. A spinning compliant tool was manufactured including the electronics for the spinning compliant tool motor driver. The contact pressure of compliant materials for spinning compliant tool polishing was measured, and the tool velocity vectors due to the tilted spinning were calculated. Several polishing cloths were tested with the spinning compliant tool to test the achievable surface texture before the selection, and a way of tailoring the polishing cloth was designed to be attached to the spherical tool.

Surface texture characteristics were investigated in the spinning compliant tool polishing, under various tool spinning RPM, pressure and discrete precession angle. A surface texture simulator was created using a statistical model of the abrasive particles, and the influence of discrete precession angle was simulated and also empirically observed.

Before the form control experiment with the spinning compliant tool, a polishing simulator (SimPol) incorporating the tilted spinning of the tool, and the distributed pressure. An algorithm to calculate the dwell time and total polishing time was developed and applied to a ⌀50 mm BK7 sample, demonstrating the feasibility of the spinning compliant tool for aspheric polishing.

An intuitive index of manufacturability is proposed, which inherently encompasses wider kinds of aspheric design. It is ideal to be used with the spinning compliant tool presented in this thesis.

1.3.2 Aims and executive summary of the thesis

The aims of this thesis are: firstly, to perform a series of systematic pitch tool polishing experiments with a CCPM to investigate the macroscopic material removal of pitch tool polishing, secondly, to develop a spinning compliant tool technique to achieve the surface texture comparable to that of pitch tool polishing, with higher material removal rate, and to develop a form figuring method using this tool, and lastly, to develop a novel method to classify aspheric surfaces so one can predict how difficult it is to make an aspheric surface design is compared to another,

The contents of the thesis can be summarised as follows.

- Chapter 2 presents the historical background for optics fabrication, and surveys and compares the current state-of-the-art techniques for polishing/figuring aspheric optics.

- Chapter 3 describes the active pressure servo mode sub-diameter pitch tool polishing experiments with the CCPM, focusing on the macroscopic material removal rate on a point of the workpiece.

- Chapter 4 defines the requirements for spinning compliant tools and describes the construction and characterisation of the spinning compliant tools.

- Chapter 5 suggests a theoretical method to calculate microscopic removal of material, or surface texture, and introduces a surface texture simulator.

- Chapter 6 describes the the surface texture experiment with the spinning compliant tools under various polishing conditions.
- Chapter 7 presents the dwell time control algorithm applied to a spinning compliant tool, and demonstrates the feasibility of form figuring control using the spinning complaint tool.
- Chapter 8 proposes a novel index of manufacturability for polishing aspheric surfaces with spinning compliant tools.
- Chapter 9 briefly summarises the work in this thesis and ends with the feasible future work on polishing aspheric optics

Chapter 2

Precision optics fabrication

2.1 Introduction

Newton is known to be the first to design and build a successful reflecting telescope in 1668.[107] He had been aware that every colour had its own degree of refraction, and by using reflective surfaces rather than lenses, he could reduce chromatic aberrations. He himself was a skilful craftsman and he ground and polished a spherical speculum mirror as the primary mirror of his first telescope. (It is an irony that the Newtonian telescope is known as a telescope with a *paraboloid* rather than a sphere nowadays.)

In fact, it was Gregory who conceived a reflective telescope in prior to Newton, but it could not be built at the time because the concave ellipsoidal mirror essential to the design was beyond the manufacturing skills of the day.[5] Historically, due to the difficulties in the measurement and manufacturing of aspherics, optical elements of spherical surfaces were widely used despite the advantages of aspheric design. Either testing methods did not give sufficient quantitative measurements (e.g. conventional knife-edge test), or each aspheric required different null lens to test with, which required extra production of testing optics. Even if a testing method was ready, since the nature of polishing is not deterministic, numerous iterative polishing and testing cycles were often required. Where aspheric designs were used, for instance in astronomical telescopes, the manufacturing process was often slow and time-consuming, thus expensive.

The situation is gradually changing as pointed out in the previous chapters. Firstly, testing methods for aspherics have been improved. Testing itself is indispensable in aspheric production along with material removal techniques. Besides stylus profilometers testing symmetric aspheric optics, novel aspheric testing methods such as computer generated holography (CGH) [77, 119], and computerised quantitative knife-edge test [110, 58] have been developed and are revolutionising aspheric measurement. However, since the testing is not of main interest in this thesis, the focus is on the manufacturing side. Secondly, the manufacturing process has been improved in diversified areas. For instance, moulding techniques[3, 39] have been developed since 1920s to mass-produce aspherics for relatively low precision optics, and the single point diamond turning (SPDT)[80, 74] technique has been developed for IR optics since 1980s, and today, approximately one third of IR lenses produced are reported to be turned aspherics.[32]

In this chapter, the brief history and typical processes of precision optics fabrication are reviewed, as well as the current state-of-the-art optics manufacturing and testing techniques being developed world-wide for aspheric production for comparison.

2.2 Brief history of precision optics fabrication

2.2.1 Manual polishing

It appears that Newton's publication[82] was also the first to introduce the use of pitch as polishing tool, an innovation of the very great importance at the time. Before the use of pitch, cloth was used to polish mirrors but with not much success due to resulting scratches. It is indeed ironic that a range of advanced manufacturing tooling today uses cloths (e.g. Multitex) combined with modern polishing consumables for optical polishing. Historically, manual grinding and polishing methods were used with pitch polishing tool and putty powder. Hand polishing is still used in many modern professional optics shops for final polishing, not to mention amateur telescope makers.

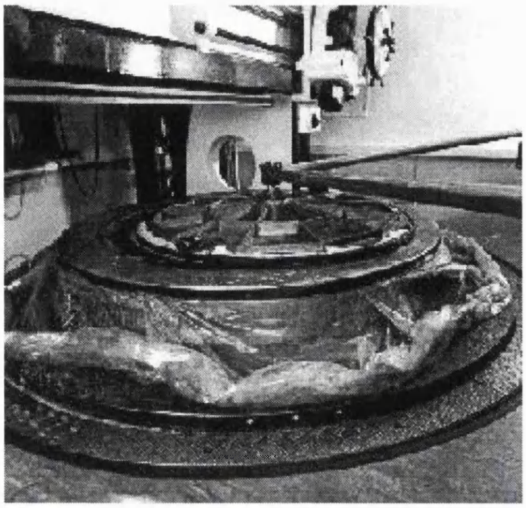

Figure 2.1: Primary mirror of the Birr Telescope, being manufactured in OSL

2.2.2 Mechanised production: A historical perspective

Some optical grinding and polishing machinery appears to have been made and used early in the seventeenth century by Descartes, Huygens, Hooke, and others. William Herschel presented a short paper to the Royal Society in 1789, in which he vaguely reports that he has completed a polishing machine with a steam engine, but not much of the mechanism was revealed.[107]

In 1845, William Parsons, or Lord Rosse, described before the Royal Society a machine for polishing large specula which uses a steam-engine, with which he polished the 6 ft primary of the Birr Telescope in Ireland, then the world's largest telescope for more than half a century.[106] Intriguingly, after some 150 years, OSL has recently completed manufacturing the primary mirror as shown in Figure 2.1[1] for the reconstruction of the Birr Telescope, in which a replica telescope of the same size is being built, but with modern technologies.

Aluminium alloy is used for the mirror substrate, unlike the wide-spread glass ceramic mirror for modern telescopes.[51] Most of modern telescopes use glass ceramic substrate for low thermal expansion with aluminised coating, but in Lord Rosse's days the chemical silver deposition process had not been discovered. Speculum (copper-tin alloy) was used as substrate without coating. Another intriguing point

---

[1] Reproduced from http://www.birrcastle.com/birr/astronomy/astframetext.html

is that the large optics grinding and polishing machine used to manufacture the primary mirror is from the Grubb-Parsons company which is founded by Charles Parsons, one of William Parsons' sons, who is famous for inventing the marine steam turbine which revolutionised the world's navies.

Other large telescopes such as Mount Wilson 60-inch (1.5-metre) telescope (1908)[66], Mount Palomar 200-inch (5-metre) telescope (1947)[26] were built with classical grinding/polishing machines before the computer era. Although there had been developments in engines for grinding and polishing machinery, there had not been much development of optics production in principle. Preston[91] published a principle of glass polishing in 1922, but it was still largely relying on the dexterity of experienced opticians for aspheric optics.

2.2.3 Computer-controlled production and intelligent control algorithms

Nowadays, CNC (Computer numerically control) machines[83, 89] are used for the mass production of optics but fundamentals of material removal of optical glass is not entirely understood. Diversified techniques both lap based and non-lap based have been developed. In the later sections, modern polishing and figuring methods such as stressed-lap polishing, active lap polishing, dwell time control method, ion beam figuring, laser ablation, magnetorheological finishing, and fluid jet polishing are reviewed.

As for the software which runs the CNC optics fabrication machines, software that can monitor and control the polishing parameters are used.[85, 33] Recently, semiconductor industry has been using to a technique called CMP (Chemical-mechanical planarisation or polishing) to planarise the silicon wafer in chip fabrication. The principle of the CMP is essentially identical to that of optical polishing.[102, 105, 97, 88, 99] Although the CMP process does not require polishing and figure the wafer surface other than flat yet, the intelligent algorithms to predict the material removal and control the CMP machines might be applicable to optical manufacturing machines.[7, 100]

2.3 Optical materials

According to Karow[50], optical materials can be classified as optical glass, IR materials, optical crystals, optical plastics, metal optics, and ceramic materials. Since The primary interest of this thesis is the material removal of brittle glass, the chemical composition and physical structure of brittle materials are briefly reviewed.

Glass is rigid, amorphous, vitreous inorganic solids which has been slowly cooled from the molten state, without crystallising.[60, 44] Basic chemical compositions of typical glasses are silicon dioxide (SiO_2), or better known as quartz, plus certain alkali, and calcium. In addition to the basic compositions, other oxides such as barium oxide (BaO), boron oxide (B_2O_3), lanthanum oxide (La_2O_3), and lead oxide (PbO) might be added.[50]

One of the basic physical structure models of oxide glass by Zachariasen[126] postulates that the Si-O network in oxide glass is built up of like polyhedra joined only at the corners with the structure being open and containing relatively large voids.

2.4 Typical stages of optics fabrication

From a heap of sand to a lens, the conventional optics fabrication procedure is[41, 50] as follows.

1. Melting the raw materials in a crucible
2. Casting of the glass block
3. Inspection for flaws
4. Cutting and edging bevelling
5. Rough grinding
6. Fine grinding
7. Polishing and figuring
8. Cleaning

9. Coating

The conventional surface material removal process involves the four core stages. 1) Bound-abrasive grinding for rough grinding, 2) Loose-abrasive grinding for fine grinding, and finally 3) optical polishing and figuring. As the process goes on, not only the abrasive sizes decrease, but also the mechanism of material removal changes. In this thesis, the focus is on the polishing and figuring stage as it is one of the least known and the most time consuming stages.

2.4.1 Bound-abrasive grinding

This is a rough shaping mode where glass blank is shaped towards the best-fit sphere. Typically, 10-12 μm diamond particle embedded grinding tools are used. The tools typically rotate at 1000-2000 RPM on a mechanical spindle. The tools may be in the form of disks cutting on the periphery, or cupped cutting on the face.

This production step is characterised by a high material removal rate, which leaves a rough surface with a highly stressed layer of subsurface damage. Glass is removed by load on the abrasive, which exceeds the surface-fracturing limit of glass.[40]

Lambropolous[65] has reported on deterministic microgrinding using bound-abrasive diamond ring tool, and the surface roughness was found to be correlated to a material crack length scale, involving the hardness and fracture toughness of the glasses.

2.4.2 Loose-abrasive grinding

This is a fine grinding mode also referred to as *lapping.* This is the stage during which rough ground surface is transformed into semi-specular surface for polishing, also targeting to achieve the best-fit sphere. It also removes the majority of the subsurface damage produced in grinding cycle, which in turn reduces the long polishing cycle. Usually, diamond particles of 0.75-3 μm with brass tooling[35] or carborundum of various grades with ceramic tile on pitch tool[10] are used for loose-abrasive grinding.

Water is known to play an important role in glass fracture in loose-abrasive grinding.[78] Although brittle mode grinding, which is a fracture and chipping process, is the primary type of removal, ductile mode (also known as shear mode) grinding, which is a ploughing and planing process, (as in metal machining) is possible by changing the chemistry of the slurry.[65] Ductile mode grinding process is much slower than brittle grinding process but it produces little subsurface damage.

2.4.3 Optical polishing and figuring

Polishing and figuring are traditionally the most non-deterministic, and painstakingly time consuming among all fabrication stages. The term 'polishing' is usually used to indicate final stage of material removal to meet the surface texture and surface form target. Also the term 'finishing' is used in this sense. 'Figuring' seems to focus more on the surface form rather than the texture.

Typically, the target of optical polishing and figuring in precision optics fabrication is to shape the workpiece to within a tolerance prescribed by the optical designer, to remove subsurface damage created by previous grinding operations, and to reduce the peak-to-valley surface roughness less than 5 nm. The form tolerance may be anywhere between a few microns in a non-critical application, to $\lambda/50$ for a UV photo-lithography lens.

The mechanism of glass removal, although not entirely understood, is generally accepted as a chemical-mechanical process.[60, 21, 44] Izumitani[43] concluded that the optical glass polishing proceeds by the formation of a hydrated layer by means of a chemical reaction between the glass surface and water, and then the removal of this hydrated layer by the abrasive particles. The hydrated layer of an optical glass surface is usually produced by ion-exchange between hydrogen (or hydronium) ions and alkali (or alkaline earth) ions.

For example, barium crown optical glass has composition range of SiO_2 40-60, Na_2O+K_2O 5-10, BaO 15-30 in mole percentage, and it relies on the hydration of alkali earths, such as Na, K and Ba.[105] Kirk and Wood[60] concluded that local plastic deformation, melting and flow of the hydrated layer results in mechanical removal when it is rubbed against harder abrasives. Cerium oxide(CeO_2) and ZrO_2 are the most common polishing agents with mean particle sizes ranging from 0.01 to 3 μ. Subsurface damage is not created during the polishing of glass because there is no fracturing of the surface, unlike grinding. The polish layer usually differs in chemical composition from the bulk glass and is predominantly silica.[40]

2.4.4 Surface metrology

The optical figuring procedure mainly comprises a time consuming iterative process of polishing (or grinding) and testing, and surface testing is as important as polishing. Surface testing itself is an active field of optics study. Since this thesis focuses on the material removal in polishing techniques, only typical testing methods are briefly described below among numerous others. Further information on optical testing can be found in Malacara.[70]

At each stage of grinding and polishing, different testing methods are used to measure surface roughness (high spatial frequency) and/or surface form (low spatial frequency). Largely, surface testing methods can be divided into two groups, and examples of each method are described as follows.

Contact testing methods

- Spherometer: Measures how concave or convex a surface is by measuring the radius of curvature of a region on the surface. This method is used when rough/fine grinding a best-fit sphere. A crude estimate of form can be achieved by measuring curvature at different zones of the workpiece.

- Multiple contact profilometer: By using a linear array of, for instance, linear variable differential transformers (LVDT) over the diameter of the optics surface, this can sample a relatively coarse profile (typical sampling spatial frequency of 10 cm). It is used during the rough or fine grinding process on large aspheric optics as it was used to measure the ⌀830 mm hyperboloid convex mirror.[54]

- Stylus profilometer: This measures surface form or surface roughness. A diamond or ruby tip is either continuously scanned, or it intermittently samples points across the surface. The height information is determined, for example, interferometrically by counting the number of fringes according to the optical

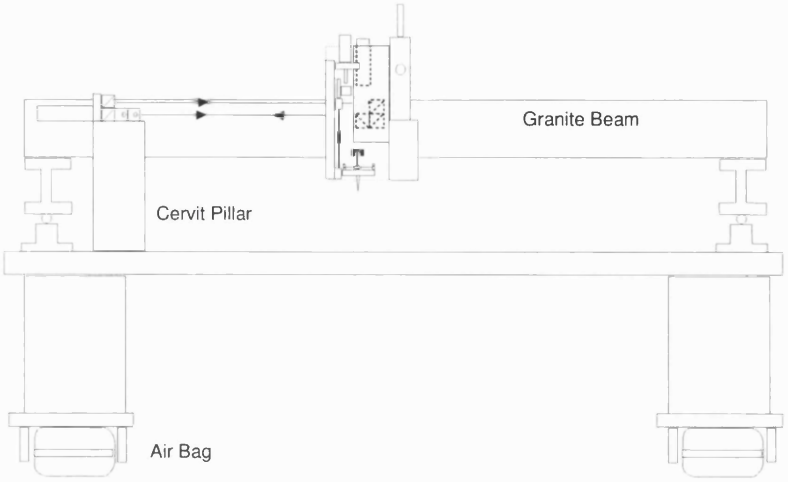

Figure 2.2: A profilometer for measuring the form of large optics, being developed by H. S. Yang, OSL[125]

path length difference (OPD).[103] Profilometry is used in the process of fine grinding or polishing stage of optics. It is generally used to measure the profile of symmetric aspheric surfaces. A stylus profilometer for large optics has been developed recently in OSL, which can measure aspheric optics up to 1 m diameter as shown in Figure 2.2.[42, 125]

Non-contact testing methods

- Knife edge test and wire test: The knife edge test is also known as the Foucault test, these testing methods are relatively simple, but sensitive geometric tests.[70] If light is launched from the centre of curvature of an ideal concave spherical mirror, the light would converge back to the centre of curvature. When a knife edge, or wire is placed at the centre of curvature, the light can be blocked. However, if the mirror surface has some irregularities, the light would not converge back to the nominal centre of curvature and the irregularities - bump or valley - can be found at least qualitatively from viewing the shadow pattern in the pupil. This method can also be used to measure the radii of curvature at different locations of the mirror quantitatively from which the form can be integrated. The principle of the knife edge is illustrated in Figure 2.3

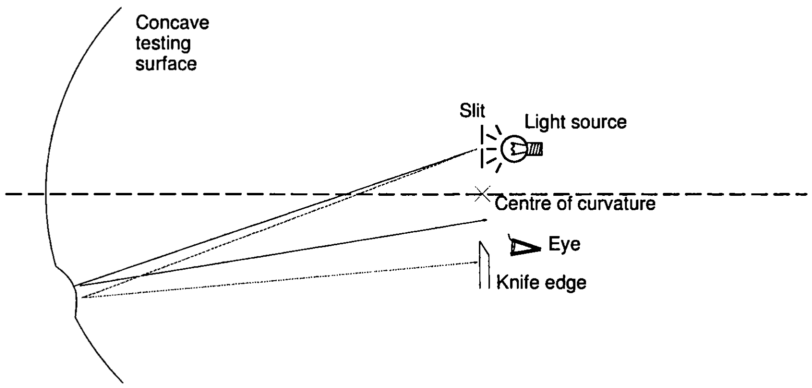

Figure 2.3: A schematic diagram of knife edge test (reproduced from [58])

Despite the high qualitative sensitivity, obtaining the quantitative results of these tests has not been easy. Recently, a computerised version of knife edge test, which uses automated knife edges in x and y directions, and a CCD camera to measure the 3D surface map over the entire workpiece surface in *quantitative* way, has been developed in OSL.[58]

- Newton interferometer: Generically called by Malacara[70] as Newton interferometer, this simple test consists of source light illuminating the workpiece and reference surface ('test plate') with relatively small air gap (several wavelengths) in between. The interferogram shows the relative height information of the workpiece surface. Similar to contour lines of a map, each fringe represents an equal-height line, and the height information gives the optical path differences. By removing the height caused by tilt between the test and reference surface, the 3D map of the test surface can be obtained. This fringe analysis is also referred as *static* fringe analysis, in contrast to the analysis for a phase shifting interferometer. This method was used for the pitch tool polishing experiments of this thesis, and the details are described later in the Chapter 4.

- Scatter plate interferometer: Scatter plate interferometer is one of the common-path interferometers. Unequal-path interferometers (e.g., Twyman-Green[70]) often make measurements difficult because the reference and test beams follow widely separated paths which affect the beams differently. It is particularly true with optical systems of large aperture.[70] The main advantages of this

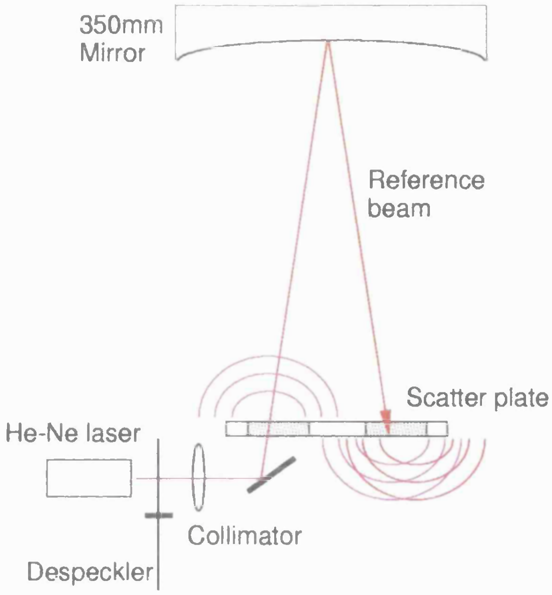

Figure 2.4: Schematic diagram of the OSL scatter plate interferometer

test are that the reference and test beams have the same path; the reference beam does not have to be the size of the test optic and thus it can measure relatively large optics without expanded beams. One disadvantage is the hot spot area in the interferogram can not be measured accurately. OSL has been using a home-made scatter plate interferometer as in Figure 2.4.

- Lateral shearing interferometer: This is yet another type of interferometer using static fringe analysis. The basic method of lateral shearing interferometry consists of displacing the aberrated wavefront laterally by a small amount and obtaining the interference pattern between the original and the displaced wavefronts.[70]

  There are various physical arrangements to obtain lateral shear. A modification[13] to the Jamin interferometer has been used in OSL. The OPD extracted from the interferogram is proportional to the wavefront slope. Thus the wavefront form may be calculated by integration. Usually interferograms from the horizontal and vertical orientations of the workpiece are taken to integrate in x and y direction. However, due to the way in which the interferograms are formed, this method can not measure the entire surface at a time.

- Phase shifting interferometer: This is a technique usually used with Fizeau or

Mirau interferometers. Unlike the interferometers based on static fringe analyses, PSI (phase shifting interferometer) technique[70] enables accuracy (peak-to-valley) of better than $\lambda/100$ with repeatability surpassing $\lambda/1000$.[112] With a microscope-like interferometer[114], PSI can be used for surface roughness, which can measure up to vertical resolution of 0.1 nm.

Depending on the wavelength of the light source with a PSI interferometer, the surface form of different range of surface roughnesses can be tested. For example, the surface form of non-specular surfaces in rough or fine grinding stage can not be measured interferometrically with He-Ne (0.633μm) light source due to the scattering. However, by using 10.6 μm IR light as the light source[113], non-specular surfaces such can be tested without stylus profilometer.

2.5 Modern techniques of optical polishing and finishing aspherics

Manufacturing of aspheric surfaces require three main processes: machining, polishing, and testing. Machining is the process of generating form of designed surfaces which need to be polished. SPDT (Single-point diamond) technology or computer-controlled grinding are the modern machining processes. Polishing is to remove the sub-surface damage left from the machining process and make the surface specular. This process also gives finer form correction. Testing, or metrology, is required to compare the current surface and the target surface to plan for the next polishing run and to assess quality on completion. The technology deficit is known to be most severe in testing, followed by polishing, and least severe in the machining process.[20]

Optical polishing remains still a challenging finishing operation. It is primarily because of uncontrolled chemical factors and associated chemomechanical interactions.

In this thesis, the primary focus is on development of novel optical polishing technology for more economical convergence - i.e. fewer polishing and testing cylces for aspheric production. In the following subsections, today's state-of-the-art optical finishing techniques competitively being developed throughout the world are discussed. Today's techniques mostly incorporate computer-controlled capabilities and can be largely divided into lap based finishing techniques and non-lap tool techniques.

Due to the indeterministic nature of optical polishing, there have been many efforts to develop deterministic machining techniques such as grinding or single-point diamond turning (SPDT) to reduce the polishing time.

However, studies on bound-abrasive grinding[65], and single-point diamond turning[92, 47] show that these operations still require further polishing to have conventionally acceptable optical surface quality, due to the subsurface damage. There is an interesting economic trade-off between grinding and polishing. Bound-abrasive grinding in precision machining generally produces features on the workpiece that degrade the surface roughness with subsurface damages. Conversely, the optimal method of achieving good surface roughness is through the use of dedicated specialised loose-abrasive fine grinding and polishing tools, which result in excellent surface roughness but poor surface form. Therefore, the problem is to balance the economics of the two processes, in order to manufacture a successful optical surface in terms of both the surface roughness and surface form accuracy required by the manufacturing tolerances.

The modern state-of-the-art polishing or finishing techniques mainly for aspheric optics are reviewed as follows.

2.5.1 Lap based finishing techniques

Lap based finishing technology is basically *rubbing* of a polisher on a glass workpiece with abrasives in between. It has been long known that pitch is the best material for polisher used with Cerium oxide(CeO_2) to give finest surface quality. It is because pitch is an extremely viscous material which is almost like solid, and it conforms to the optics surface when put on workpiece several hours in room temperature.

In the next sections, pitch tool polishing techniques for aspheric surfaces with different approaches to control glass removal are introduced.

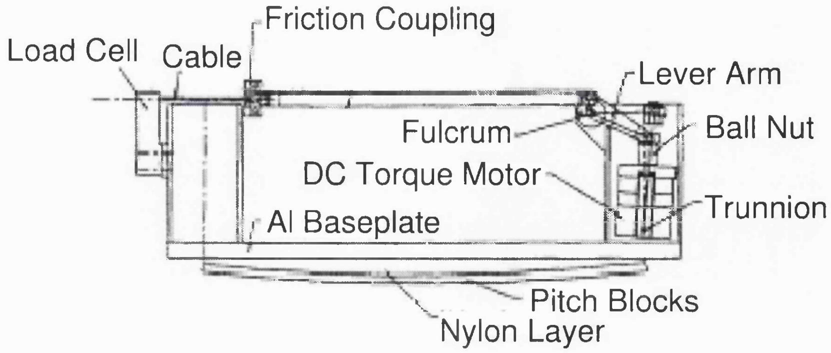

Figure 2.5: Cross-section of the Steward Observatory Mirror Lab's stressed-lap for aspheric polishing[2]

Stressed-lap polishing

Stressed-lap from Steward Observatory Mirror Lab of University of Arizona has been developed from late 1980s, which is an actively stressed lap.[120] The principle of stressed-lap is to control the aspheric form of the tool by deforming the tool. Computer combines the real time position and orientation of the tool, and the geometry of the mirror to control the lap shape. The idea is that the optician can polish highly aspheric surface as if he were polishing a sphere. West[121] has reported polishing a 1.8 m, f/1.0 primary mirror to a surface error of 17 nm rms and 170 nm peak-to-valley. The lap is 60 cm in diameter with 12 tension band actuators and, is reported to perform below 4 μm rms for shape repeatability. The stressed-lap is shown in Figure 2.5

More recently, actuators to control polishing pressure and pressure gradients were added to the original concept to polish the MMT primary mirror (6.5 m f/1.25 paraboloid).[71] However, the authors do not reveal whether the stressed-lap monitors the *in situ* polishing pressure on the workpiece, which is believed to be an essential parameter to monitor, in order to control and to predict the removal rate as pointed out by Kim.[54] Although the shape of the tool and pressure are controlled over the workpiece, it is reported that they still had to use small conventional stiff passive tools for local figuring.

Stressed mirror polishing

This method is used to polish the 1.8 m hexagonal segment mirrors for the primary mirror of Keck Observatory, Hawaii. Similar to the Steward Observatory Mirror Lab's stressed-lap polishing, but in this case, the mirror blank itself is deformed with a special vise. The mirror is bent just enough to permit the polishing of a spherical depression or figure using an ordinary spherical pitch tool. With the vise forces released, the mirror is "relaxed" into its desired asymmetrical shape. It has been reported [72] that the achieved surface form error was 0.25 μm RMS. However, analogous to Steward Observatory Mirror Lab's stressed-lap polishing, the stress information was needed on the *mirror blank*, using intensive finite element analysis and strain gauge to develop the special vice.

Dwell-time control polishing

Jones[48, 49] showed that CCOS (Computer-Controlled Optical Surfacing) technique from Litton Itek Optical Systems can polish large (4 m) but thin (1.7 cm) ULE segment to 35 nm rms surface error and 0.8 nm surface roughness. CCOS machine consists of a sub-diameter (20 cm square) tool with holes for vacuum suction. Vacuum suction was used to prevent the print-though effect of the support system on relatively thin mirrors. The CNC unit moves a rapidly orbiting (420 rpm) tool across the optics. Based on the difference between measurement and target surface, the computer controls the removal rate by applying different dwell-times of the tool on different places of the workpiece.

However, the CCOS machine uses substantially small sized pitch tool which means more polishing time to cover the whole area of the workpiece, and less efficiency in removing high spatial frequency errors of the surface profile compared with a full size tool. More importantly, as in the stressed-lap, the CCOS machine does not monitor nor actively control the polishing pressure during polishing. Since the control loop is primarily based on dwell-times, not the fundamental physics of material removal, it could be less efficient in terms of convergence rate and time. For instance, when there is a high bump somewhere on the workpiece, CCOS would simply exert longer dwell-time rather than giving higher polishing pressure to remove the bump, which would understandably take longer.

Large flexible lap polishing

Geyl and Paseri[30] from REOSC reported a successful polishing of the VLT 8.2 m f/1.8 hyperboloidal primary mirror on a 175 mm thickness Zerodur workpiece. The surface error was not disclosed as a target surface quality, but CIR (Central Intensity Ratio) was targeted to be greater than 0.80, and surface roughness less than 2 nm. All were reported to be met.

The REOSC computer-controlled figuring technique uses flexible laps of various shapes and dimensions ranging from 1-4 m. While Geyl and Paseri[30] do not clearly address the mechanism of their polishing tool itself, they claim they could precisely control the amount of material removed on each point of the surface by combining the pressure exerted on the tool, turntable rotation speed, arm oscillation speed, amplitude and orientation. The mirror support system consists of 150 pneumatic actuators, and each one was equipped with a load cell for controlling pressure with 2 N accuracy. The actuators can maintain any pressure distribution all over the rear face through a computer-control polishing operation. Another 8 m class telescope primary mirror was manufactured by REOSC using similar workpiece support, but again this paper does not reveal any of the polishing technique itself.[17]

Active lap polishing

OSL's original approach to optical polishing, called the *active lap polishing*, was developed applying a fundamentally different concept.[116] As the development is described in detail in[54], the ⌀830 mm active lap consists of 22 active load cells evenly distributed among 61 load cells. The active lap is shown in Figure 2.6.

The main distinctive feature of OSL's active lap is that it monitors and actively controls the polishing pressure. By combining the polishing pressure, relative tool speed, and dwell-time all at once in real time for each position on the workpiece surface, the actual physical phenomena of material removal can be observed better than by relying on the change of tool shape or dwell-time. The original idea was to control the pressure distribution exerted by the active lap as it traversed the

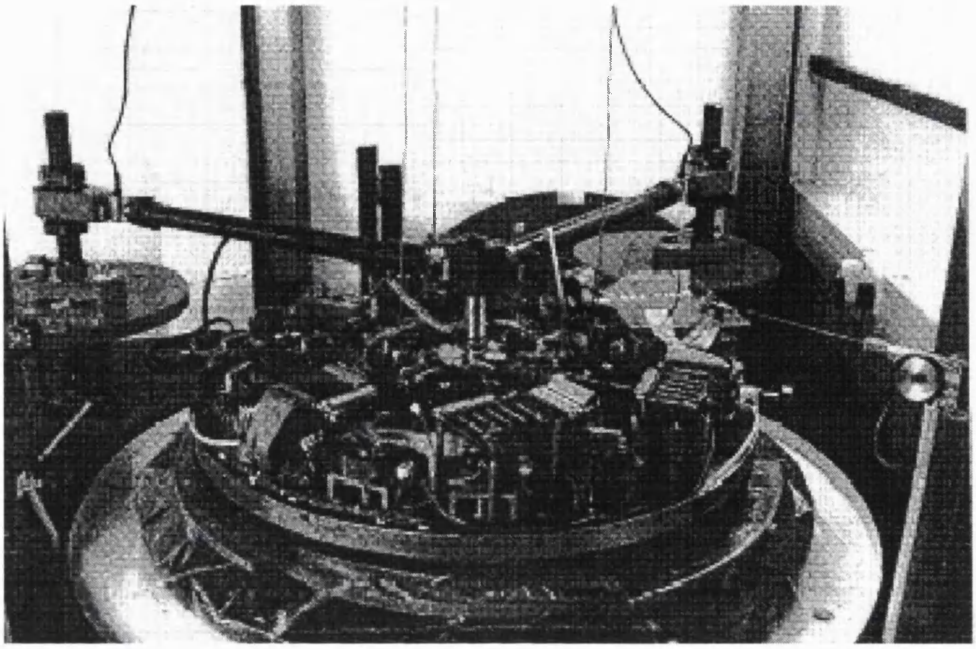

Figure 2.6: Active lap to polish a convex hyperboloid secondary mirror (scaled down model of Gemini secondary mirror) developed in OSL[57]

workpiece surface. However, it was reported that the effective way to polish with the active lap was to make the pressure distribution within the tool so that it gives a static Gaussian-like pressure distribution, and rock this “hot spot” across the surface.[116] It was this discovery that led to the concept of the pressurised membrane tool described in this thesis.

Results on fabrication of an 83 cm scaled down model of f/7 Gemini secondary mirror is in[57] which reports about 10% improvement in each polishing run, which is comparable to about 11-13% improvement achieved by the stressed-lap polishing. The surface form accuracy is reported to reach 0.4 μm peak-to-valley in a defined set of polishing runs.

Based on the active lap polishing technique, OGL was spun-off to make computer-controlled polishing machines for smaller optics based on the membrane tool principle. As in the active lap polishing, the OGL’s CCPM[57] uses a proprietary software to combine parameters such as real time tool pressure, relative tool speed, and dwell-time to predict the material removal.

Miscellaneous lap-based methods

Other lap-based polishing techniques which do not use pitch have also been developed. Using various types of polishing cloths ranging from synthetic rayon to velvet, but with abrasives do not seem to provide surface quality comparable to that obtained by pitch and cerium oxide.[11, 52]

Plastic surfaces are also used for optical polishing. For example, using a polytetrafluorethylene plastic (Teflon) as a substitute to pitch on Zerodur substrates was reported[68] to give an optical flat surface. Flatness was maintained to better than $\lambda/10$, and surface roughness was achieved less than 1 nm rms.

Recently a possible use of bound-abrasive as *polisher*, not as grinder has been reported.[31] The main advantage is that it can be used on the same bound-abrasive *grinding* machine to give high removal rate. Proprietary polishers are also available that use an epoxy resin which has cerium oxide particles embedded with erosion promoters to expose fresh cerium oxide as the polishers wear out. These were demonstrated[31] to polish approximately from 400 nm surface roughness down to 1 nm in 30 minutes. However, the issue of surface figure correction during polishing has not been resolved.

2.5.2 Non-lap based finishing techniques

Optical surface techniques which do not use laps are also being aggressively developed. Since the tool is not based on a hard lap, it has inherent advantages in polishing aspheric optics which have varying radii of curvature. The following techniques use more innovative methods in the way in which glass is removed compared with conventional lap based technologies. However, all of the following techniques are regarded as a complementary techniques to lap based techniques since none of them is wholly satisfactory for optical finishing yet.

Ion figuring

A number of places have been developing ion beam figuring systems for different optics size, including NASA and Eastman Kodak.[22, 1]

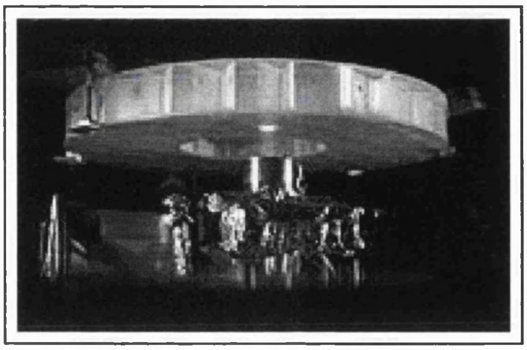

Figure 2.7: The ion figuring system developed by Kodak

The Kodak's ion figuring process removes material by transferring kinetic energy from impinging neutralised argon ions. Although it is a finishing technique, it is basically a *figuring* technique, which is an issue of surface form error, not surface roughness. It requires a well polished surface before ion figuring can begin. The ion figuring technique is regarded as a complementary method to pitch tool polishing technique. Kodak's ion figuring system is shown in Figure 2.7[2] and it is reported routinely to achieve surface form error less than 30 nm peak-to-valley, and 6 nm rms. Kodak's system has been used to make segmented primary mirrors of the Hobby-Eberly Telescope and W. M. Keck Telescopes.

The technique is known to be highly deterministic and repeatable but also very slow since removal energy is transferred indirectly, unlike lap based polishing. However, it has advantages of not loading the workpiece as much as lap-based polishing and can avoid print-through effects or edge roll-off problems.

Magnetorheological finishing

The COM (Center for Optics Manufacturing) of the University of Rochester has been developing the magnetorheological finishing (MRF) technique.[45, 61, 34] MRF uses a magnetorheological fluid mixed with abrasive slurry as a compliant replacement for a conventional rigid sub-aperture polishing lap. As shown in Figure 2.8[3], the fluid's viscosity is magnetically manipulated to stiffen while in contact with a portion of

---

[2] Reproduced from http://www.kodak.com/US/en/government/ias/optics/ion.shtml

[3] Reproduced from http://www.opticam.rochester.edu/content/combrochure/finishing.htm

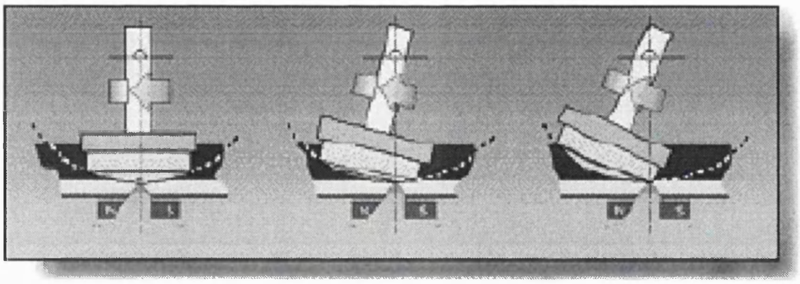

Figure 2.8: The magnetorheological finishing method to polish aspheric optics

the workpiece surface, thus effectively creating a sub-aperture polishing tool that conforms to the optical surface. Since the "polishing tool" is compliant it can in principle be used for concave, convex, or aspheric workpiece. However, there is a limit in the radius of curvature for convex optics. QED, a spin-off company from COM developed a commercial MRF machine and their polishing results are reported in [33].

The MRF technique is essentially a dwell-time controlling technique. In other words, it is basically a smaller version of Litton Itek's CCOS technique but with a "virtual" tool which enables it to handle various shapes of optics surface.

Laser ablation

Laguarta[63, 64] showed that optical surfaces traditionally polished on conventional glasses with high coefficients of thermal expansion, may also be polished by irradiation with a space and time controlled uniform CO_2 laser beam. They showed that a 80 cm^2 area on heated TRC-33 glass could be polished from initial 500 nm to 10 nm rms in surface roughness. To find out the conditions for successful and reliable use of the technique, the laser-driven heating process is monitored by means of the surface and depth temperature distributions.

Although it is still at early stage and has not reached the stage of controlling the surface form as well as surface roughness over larger area, it may eventually prove to be a competitive alternative to conventional polishing techniques for appropriate substrates.

Single-point diamond turning ductile grinding

Possibility of using SPDT (single-point diamond turning) ductile grinding technique as optics finishing technique was studied by Puttick *et al*[92] in which they conclude that, below the critical depth of cut predicted by a fracture mechanics analysis, glass material is removed in ductile-regime. Kim and Nam[53] also reports the similar results with an experiment on brittle ferrite.

However, Jeynes and Puttick[47] point out the optical material and electronic applications of such techniques depend, not only on the surface finish, but also on the depth and nature of the subsurface damage. TEM (Transmission Electron Microscopy) has shown that the turning damage extends below the surface to a depth of some 300 nm, which may cause a critical problem for refractive optics elements for the visible band. Currently, the SPDT ductile grinding technique is mostly being used to manufacture IR optics[32] which do not require as low a surface roughness as visible or UV optics.

Fluid jet polishing

Fähnle[36, 25, 23] reported early results from what he calls fluid jet polishing (FJP). It uses a jet stream of fluid abrasive on the workpiece to remove material. Unlike conventional high pressure (70-5400 bar) abrasive slurry jet systems, it applies less than 6 bar (=0.6 N/mm^2), resembling the usual polishing pressures. It was demonstrated that FJP can be used to polish a BK7 workpiece from a surface roughness of 350 nm to 25 nm RMS.

Since the tool is fluid as in the MRF technique, FJP also shows an inherent advantage of conformality to polish aspheres. The FJP can have some advantages over MRF in terms of the more variable polishing spot shape and size depending of the slurry nozzle geometry, therefore can be optimised Fähnle noted. However, Fähnle's work is yet at its early stage, as is the laser ablation technique, which only demonstrated the polishing capability for a limited area on the workpiece, let alone the capability of form control of an optical surface.

2.6 Conclusion

A number of modern polishing and figuring techniques for large and small optics were reviewed in the previous sections. The key techniques from the previous sections are summarised in Table 2.9 and Table 2.10 to compare and contrast. Table 2.9 summarises the polishing and figuring techniques for larger optics. It can be seen that the Kodak's ion figuring offers the best surface form error, but it takes longer than other techniques. OSL's active lap shows a feasibility of most rapidly converging to a targeted surface, because it is supposed to control three main polishing parameters, namely the tool pressure, speed, and dwell time. Table 2.10 shows the optical polishing and figuring (or machining) technique for small optics. The COM's MRF technique gives the best surface form controllability and surface roughness.

	Description	Advantages	Disadvantages	Achieved form error	Achieved surface roughness
Stressed-lap (Steward Observatory Mirror Lab)	Sub-diameter Pitch tool. Aspheric shape controlled according to different radius of curvature on workpiece.	Tool is conformal to the changing workpiece radius of curvature, thus optician can polish as if the workpiece is spherical.	Complex tool bending mechanism. Requires separate tools for concave & convex workpiece. No monitoring of polishing pressure.	170 nm p-v, 17 nm rms	Pitch tool polishing quality (1.2nm rms)
Stressed mirror polishing (Keck Observatory)	Spherical tool. The mirror blank is stressed to spherical form by special vice, released after polishing	The workpiece is spherical while polishing, thus optician can polish as if the workpiece is spherical	Complex mirror blank bending mechanism. Requires intensive mirror stress research with FEA and strain gauges. No monitoring of polishing pressure.	250 nm rms	Pitch tool polishing quality
CCOS (Litton Itek Optical Systems)	Small sub-diameter pitch tool rapidly orbiting around an axis. Tool dwell time is controlled on workpiece. Vacuum suction between the tool and workpiece.	Vacuum suction for the tool enables no print-through effect for thin optics. 2D dwell time control over the workpiece area, non-symmetric asphere such as off-axis paraboloid can be polished.	Complex vacuum and orbiting mechanism. Tool has to be relatively small to give orbital strokes. No monitoring of polishing pressure.	0.035 microns rms	0.8 nm (rms)
Active lap (OSL)	Full size pitch tool with load cells and actuators to monitor and control the polishing pressure in real time.	Full size tool, thus higher removal rate. Distributed pressure for less furrow effect. Can control three (P,S,T) polishing parameters simultaneously, feasibly for rapid form convergence	Complex load cell & actuator mechanism. Requires separate tools for concave & convex workpiece. Only passive servo mode demonstrated.	0.4 microns p-v	Pitch tool polishing quality
Ion beam figuring (Kodak)	Bombardment of ion particles removes the material.	Highly deterministic. No print through effect, no edge roll-off problems	Slow ablation. Requires pitch polished surface, complex ion apparatus.	0.018 microns p-v	As pitch tool pre-polished

Figure 2.9: The optical polishing and figuring techniques of today for large optics

Figure 2.10: The optical polishing and figuring techniques of today for small optics

	Description	Advantages	Disadvantages	Achieved form error	Achieved surface roughness
Single-point diamond turning	Below the critical depth of cut, ductile grinding occurs rather than brittle fracture. Used to make IR optics.	High material removal rate. Simple diamond tip can turn concave & convex aspheres.	Subsurface damage insufficient for the visible optics. High infeed resolution of diamond tip required to achieve form error of nm.	N.A.	2-3 nm rms
Laser ablation	CO_2 laser fire causes local melting and plastic flow of the heated workpiece of high coefficient of thermal expansion.	Not an abrasive process. Removes subsurface damage, and gives good surface roughness. Possibly achieve very high polishing rate if the whole workpiece surface is fired.	Can not yet control the form and requires pre-figured surface. Surface roughness result reported on a small area ($80cm^2$)	N.A.	10 nm rms
Magnetorheological (COM)	Rotating magnetorheological fluid abrasive is stiffened by magnetic field to polish spinning workpiece by control the dwell time.	Tool conformal to complex aspheric surface. No tool wear as with pitch or cloth. High material removal rate. Asymmetric asphere also can be polished.	Limit in polishing deep concave surface due to the rotation radius of the MRF fluid.	$0.16\ \lambda$ p-v	0.1 nm rms
Fluid jet polishing (TNO)	Applies fluid abrasive jet with than 6 bar (87psi) of pressure to remove material. Similar to ion figuring except the energy transfer medium is liquid.	Similar advantages as MRF. Different nozzle geometry and angle can give different polishing spot shape and size.	Still in early stage and surface form control not reported.	N.A.	1.6 nm rms

Chapter 3

Material removal experiment with active servo mode pitch tool polishing

3.1 Introduction

It was discussed in the previous chapters that sub-diameter pitch tools are required in order to polish an asphere, due to the varying radius of curvature on the aspheric surface. The work in this chapter is continued from the previous work in OSL[54, 57] on optical polishing and figuring. Then, the passive servo mode, in which the pressure distribution was pre-configured for the tool, rather than updated in real time, was used to demonstrate an encouraging form improvement factor in the previous work. The material removal rate in pitch tool polishing is further investigated with a more systematic approach using a computer-controlled polishing machine (CCPM). The *active* servo mode, in which the polishing pressure is monitored and controlled in real time, is demonstrated for the experiments in this chapter, with a smaller scale optics and a sub-diameter pitch tool.

Knowing the material removal characteristic is the key to the successful control of a surface form, particularly an aspheric design, towards the rapid convergence to a target form. Polishing parameters such as the tool pressure and relative tool speed are controlled by the CCPM, and the material removal behaviour is observed and analysed. Although the results of this chapter can not be directly compared with the results from the passive servo mode polishing in the previous work[54, 57], the work in this chapter grounds the work for the spinning compliant tool polishing in the following chapters.

Among many attempts to explain the physical or chemical phenomena in optical polishing as briefly introduced in Chapter 2, Preston's equation is still one of the simplest and most widely used theory of optical polishing. A series of pitch tool polishing runs are analysed, based on the Preston's theory in this chapter. As well as the original Preston's equation, a modified Preston's equation are empirically fitted to the material removal rate measurements. By repeatedly carrying out the experiments with the identical polishing parameters, the material removal prediction accuracy, defined as measured material removal over predicted material removal, is estimated. The focus is on the surface *form*, not the surface roughness, due to the limit of the interferometric testing equipment used for the experiment in this chapter.

3.2 Preston's equation

Optics community has been using the Preston's equation [90][91], which states

$$\Delta m = kL\rho\Delta S, \tag{3.1}$$

where Δm = removed mass along the track of the lap movement (g), k = material removal coefficient (cm^2/dyne), L = normal load (dyne), ρ = density of the glass ($\mathrm{g/cm}^3$), ΔS = length of lap movement.

The mass of total removed material is proportional to the normal load on the tool, density of the workpiece, and the stroke distance. A modification to the above equation leads to

$$\frac{dz}{dt} = k\frac{L}{A}\frac{dS}{dt}, \tag{3.2}$$

where $\frac{dz}{dt}$ is the material removal rate,which is the removed depth per unit time, k is the material removal coefficient, A is the footprint area of the polishing tool, and $\frac{dS}{dt}$ is the relative speed of the polishing tool on the workpiece. It can be re-written as

$$W = kPS, \tag{3.3}$$

where W = rate of removed depth (mm/sec), k = material removal coefficient ($\mathrm{mm^2/N}$), P = applied tool pressure ($\mathrm{N/mm^2}$, also in kPa, where 1 $\mathrm{N/mm^2}$=10^3kPa), S = relative tool speed between the workpiece and tool (mm/s).

3.3 Material removal experiment

A series of experiments were carried out to investigate the relationship between the material removal rate under various polishing parameters. Tool pressure and sliding speed was controlled as the main parameters in the equation. A set of different pressure and speed combinations (four pressures × four speeds) was applied on a glass ceramic workpiece to observe the relationship between material removal rate, and tool pressure pressure and the relative tool speed. Three identical sets(A, B, and C) were carried out to investigate the repeatability.

A systematic approach in controlling the pressure and speed parameters by utilising a computer controlled polishing machine (CCPM). For each combination of the parameters, annular groove was made on a ⌀155 mm Astrositall blank. To measure the integrated material removal rate, the depth of groove was measured by interferometric method and divided by the integrated dwell time sampled by the CCPM.[85] The material removal rate was plotted against the applied pressure and speed.

3.3.1 Testing set-up

The experiments in this chapter were carried out before the automated phase shifting interferometer (PSI)[112] was equipped in OSL, and a interferometer had to be built to measure the polished surfaces. The homemade interferometer is used with an interferogram analysis software which can handle static fringes[122] in OSL. Among the following candidates a simple contact interferometer was developed for this experiment.

A primitive interferometer comprising a reference flat, test surface, and a Hg lamp as light source had been used by pressing the reference flat against the test surface for the previous work[57]. However, it required two people for the measurement - one pressing the reference flat on top of the workpiece, and the other operating computer for running the fringe analysis programme at the same time. It also consumed much time to have right number and orientation of fringes by pressing the optical flat by hands. Therefore a more efficient way of testing polished surfaces was required for a large number of polishing experiments.

Firstly, a Michelson interferometer was proposed but soon discarded from the concept stage. Due to the size of the workpiece(∅155 mm), the size of the beam-splitter had to be large enough to cover the whole surface of the workpiece which was excessively expensive for the project budget. When the workpiece size is ∅155 mm, the beam-splitter needs to be at least $155\times\sqrt{2} = 219$ mm to cover the workpiece surface with 45° angle.

Secondly, a Fizeau interferometer was attempted as shown in Figure 3.1, but was discarded in the middle of construction for the following reasons. The design was based on a commercial version of the Fizeau interferometer introduced in Malacara.[70] A 1.5 W He-Ne laser was used as the light source for longer coherence length. The convenience of larger air gap between the reference and test surfaces was anticipated so that the test piece can be put and removed easily. The idea was to put the test piece on the bottom plate without any alignment, and to adjust the reference flat with three alignment nuts. A 10.7 m long single mode optical fibre was used as the wave guide to remove the speckles caused by the fibre optic, but the beam quality was still poor with many visible speckles when the image was seen from the camera side.

More critically, it was found that the thread of the studs supporting the reference flat was not fine enough thus could not align the reference flat in accuracy of order of wavelengths. In order to see the fringes the reference and test surfaces had to be set parallel and then wedged in the order of the wavelength which is 632.8 nm for He-Ne laser. The three supporting studs were M8 with pitch to pitch distance of 1.25 mm, and the thread was larger than the required accuracy for aligning the reference flat. The fringes made by the two surfaces of beam splitter itself were visible, but the fringes from the reference and testing surfaces could not be seen.

Finally, it was decided to return to the simple interferometer due to the complexity

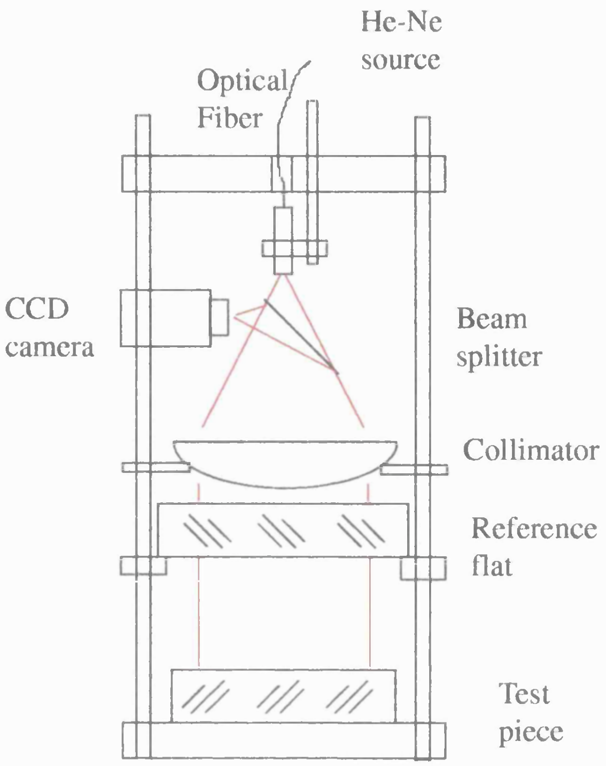

Figure 3.1: A diagram of proposed Fizeau type interferometer

of the proposed Fizeau set-up. An improved holding mechanism of reference flat was adopted as in Figure 3.2. Three micrometers were used as legs to support the reference flat just above the workpiece, which made it easier to manipulate the number and orientations of fringes. The height and tilt of the reference flat were adjusted with micrometers and could be kept for relatively longer time enabling one person to run the whole measurement process. The micrometers had the minimum reading of 10 μm and they satisfied the required accuracy to control the fringes. Typically less than a couple of minutes were needed to grab one image of fringes. A dedicated test rig was built for the testing flat mirrors as shown in Figure 3.3, which comprises of a CCD camera to feed into the static fringe analysis software.

3.3.2 Workpiece

For the choice of a workpiece, glass ceramic blank was chosen because of its availability. It was a spare blank for the secondary mirror of SaTReC camera breadboard model[67]. Due to its thermal characteristics, glass ceramic materials take an impor-

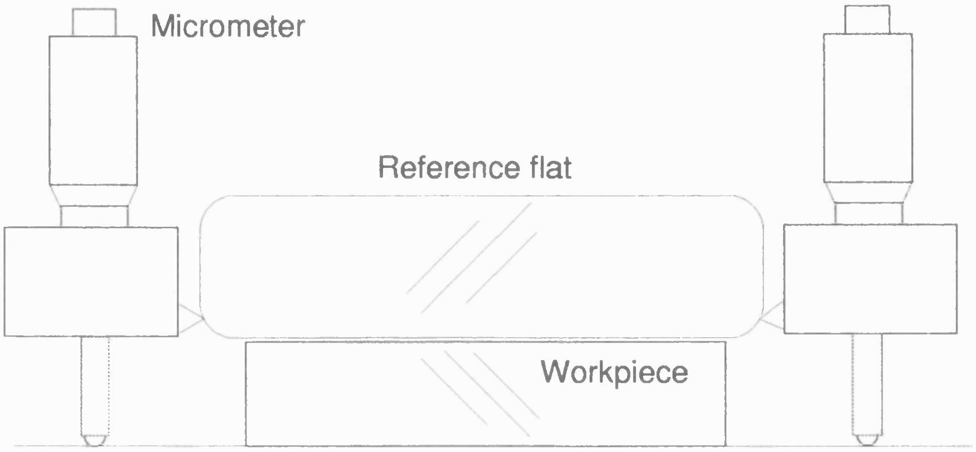

Figure 3.2: Simple Newton interferometer for surface form measurement (the third micrometer leg not shown)

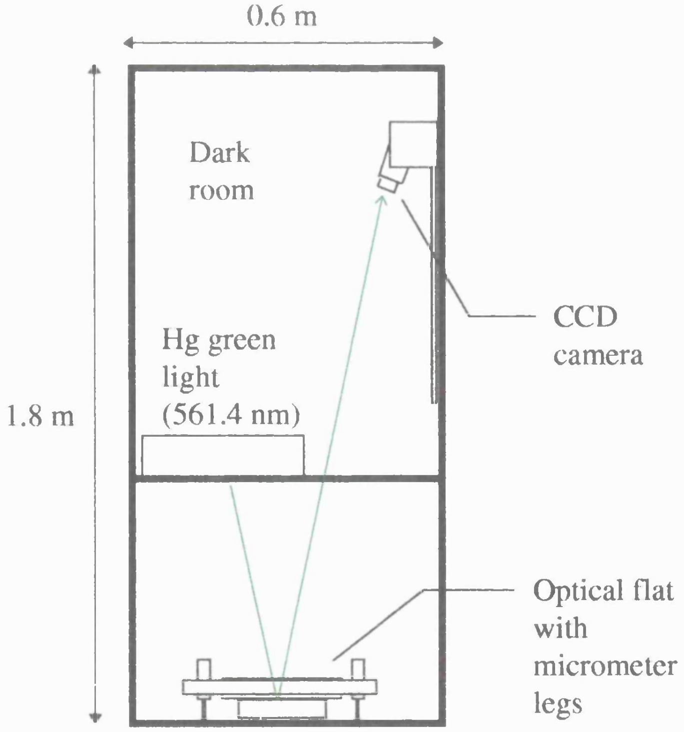

Figure 3.3: Test rig dedicated for flatness measuring

	Coeff. Therm. Exp.	Density	Poisson coeff.	Diam.	Thickn.
Sitall S0115M (Astrositall)	0±0.5 × 10^{-7}/K (-60 - 60°C)	2.46 (g/cm^3)	0.28	Ø155.0 +2.0mm	25.0 +2.0mm
Zerodur (Schott)	0±0.2 × 10^{-7}/K (0 - 50°C)	2.53 (g/cm^3)	0.243		

Table 3.1: Thermo-mechanical properties of glass ceramic materials

tant role in astronomical and space optical instruments. In glass ceramic materials, positive coefficient of thermal expansion of amorphous substances is compensated by negative coefficient of thermal expansion of crystalline at room temperature[75]. Some thermo-mechanical properties of glass ceramic and the dimensions of the workpiece are listed in Table 3.1. Astrositall had been chosen over Zerodur and ULE due to the availability and the cost of the camera project.

The workpiece was taped around the periphery with masking tape for marking purpose. The markings were used for identical positioning of the workpiece on the turntable and on the test rig.

Initial surfaces were made with CCPM to make the workpiece flat enough to make fringe analyses easier when grooves were made on the surface. After numerous trial and error sessions for selecting the tool and polishing method, a Ø190 mm pitch tool was placed on the turntable and the workpiece was put on top of it for planarisation. The typical form accuracy of the initial surfaces was $\frac{1}{2}\lambda$ excluding the turned down edge which was not used. The best result achieved was $\frac{1}{4}$ fringes, thus $\frac{1}{8}\lambda$. The minimum fabrication time was two hours of total polishing time with the CCPM, and total of twelve of initial surfaces were made.

3.3.3 Pitch tool

A number of pitch tools with sizes between 19 mm and 24 mm were made on a 25 mm aluminium alloy base throughout the experiment. The pitch tools had circular footprint with no grooves on the contact surface to calculate the contact area easily. The hardness was changed by adding turpentine to the pitch crucible while it was heating. When the pitch was too hard it gave high pitch noise during the polishing, and when it was too soft the tool deformed during the polishing. One pitch tool was made for each set. The safe hardness was measured by an indentation tool as 0.03-0.06 in/5 min. In order to calculate the effective contact area for the set A and C four different diameters around the periphery were measured and averaged , because the pitch tool shape was not exactly a circle. It was measured before each polishing run to see the pressure influence on tool size. For the set B, the tool deformed to an elliptical shape during the polishing and it caused changes in effective pressure applied to the tool and the integrated dwell time sampled by CCPM due to the reduced contact area. The effect of tool deformation was compensated later.

3.3.4 Abrasive and other environmental factors

Cerium oxide(Regipol 788) was used as the polishing abrasive. Cerium oxide powder was suspended in distilled water to make 100.46 g/l abrasive for set A and B, and 100.05 g/l for set C. It was reported in [54] that abrasives evaporated as polishing goes on and gave sharp rise in friction coefficient when polishing. The abrasive was supplied sufficiently to minimise the evaporation effect of water in the abrasive.

The acidity of the abrasive was measured with pH test paper and it consistently stayed in pH 7-9 throughout the experiment. The ambient temperature was measured and it was within 27 ± 1 °C for set A, $21\sim24$ °C for set B, and 21 ± 0.5°C. The humidity was not measured in this experiment.

3.4 Controlling polishing parameters with CCPM

Figure 3.4 shows the CCPM used in this experiment, which was developed by Optical Generics Limited (OGL), the spin-off company from OSL.

It has a ⌀600 mm turntable for the workpiece, and X,Y,Z cantilever to move the polishing head. The polishing head has load cells inside to read the real time polishing pressure. A PC controls the polishing strokes, turntable RPM, tool pressure and speed, and another PC displays the real time prediction of material removal.

The tool pressure and speed were systematically controlled by the CCPM so that

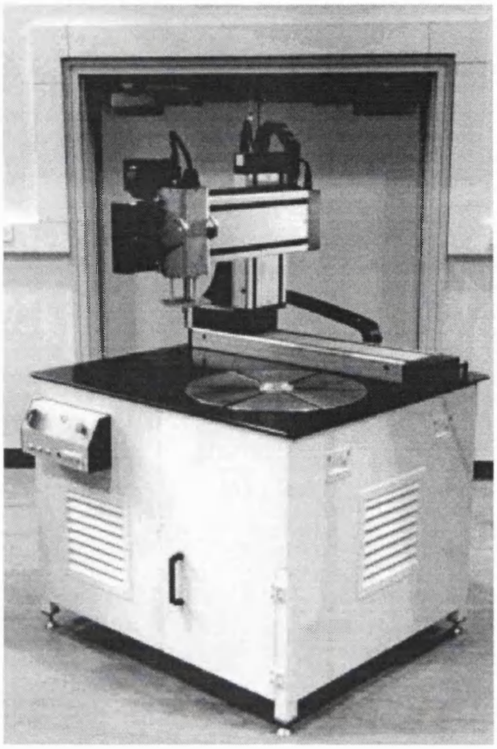

Figure 3.4: Picture of the CCPM used in the thesis

the material removal rate can be plotted against pressure and speed.

3.4.1 Tool pressure

With the CCPM's pressure servo mode, it could sample and update the pressure in 5 Hz, but it showed deviations from a nominal pressure depending on the input pressure and turntable RPM. Pressures higher than 0.12 N/mm^2 caused irregular frictions when polishing, and gave abnormally high pressures giving warnings of 90% of maximum load.

Pressure deviations were recorded for several pressures (0.02, 0.05, 0.07, 0.10 N/mm^2) with turntable RPM (5, 10, 15, 20, 25), and typical pressure deviation was about ±10 % at worst and ±3 % at best. It tended to have less deviation towards higher pressure and lower speed. 0.06 N/mm^2 was the minimum pressure which showed pressure deviation no higher than ±10 %.

3.4.2 Turntable RPM and tool sliding speed

Since the only moving part was the turntable, the tool sliding speed was determined by the turntable RPM and the radius of the locus of the centre of the tool. When the turntable was rotating with an RPM, the relative speed s of the centre of the tool at radius R away from the centre of the workpiece was

$$s = \frac{2\pi \times RPM}{60} \times R, \tag{3.4}$$

with s in unit of mm/s. Pressure readings from the CCPM pressure sensor were unstable when the turntable exceeds 25 RPM. The suitable turntable RPM range was found to be between 5-24 RPM. Since one rotation of turntable was angularly encoded with 2500 units, the deviation of the RPM was regarded less than 1%.

3.4.3 Choice of pressure and speed

Among the operational pressure and turntable RPM range of the CCPM, finally following set of pressure and speed values were carefully chosen for the tool (⌀19-24 mm).

- Pressure : 0.06, 0.08, 0.10, 0.12 N/mm^2
- Speed : 25, 50, 75, 100 mm/s.

Pressure versus speed values are plotted in Figure 3.5 and indexed according to the row and column numbers. (e.g., speed = 25 mm/s and pressure = 0.12 N/mm^2 is row 1 column 1, and coded r1c1) The workpiece was put on the turntable with a set RPM for desired speed of the tool. The tool was then fixed at an off-centred position with a constant pressure, thus the only moving part was the turn table.

3.5 Polishing and measurement

One set consisted of 16 polishing runs according to the pressure and speed parameters selected as in the Figure 3.5. Total of three sets were done to see the repeatability. Each polishing and measurement cycle was comprised of the following steps as in Figure 3.6.

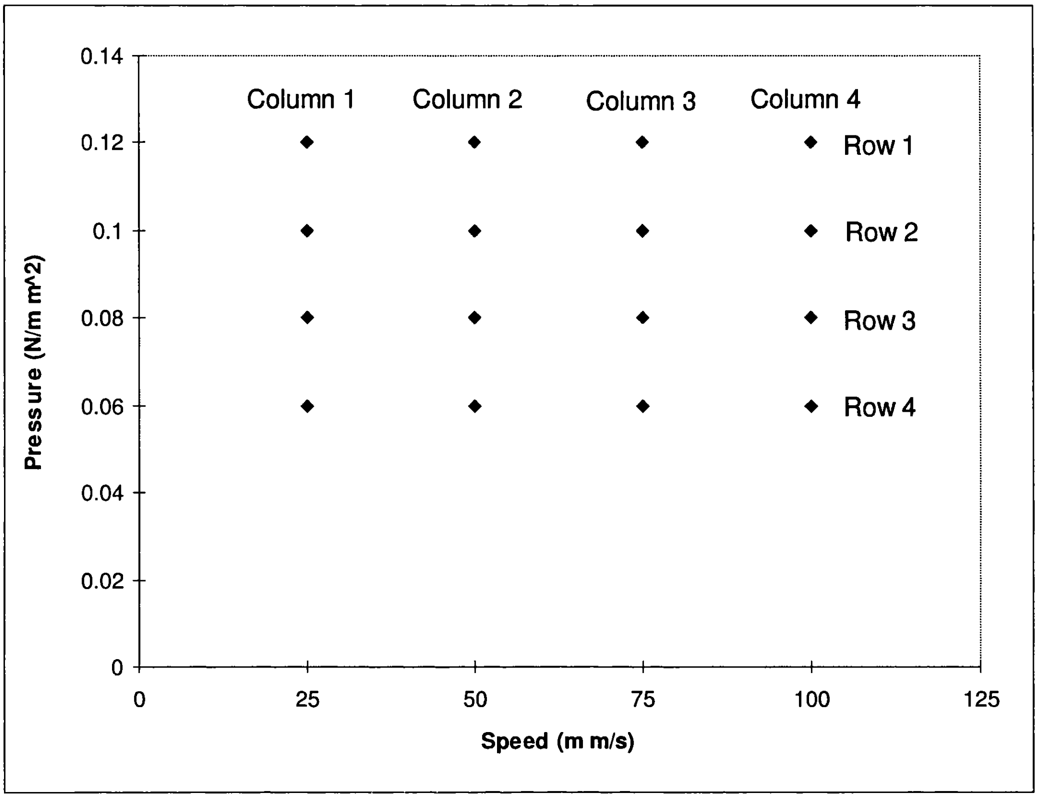

Figure 3.5: Pressure and speed values used for polishing indexed

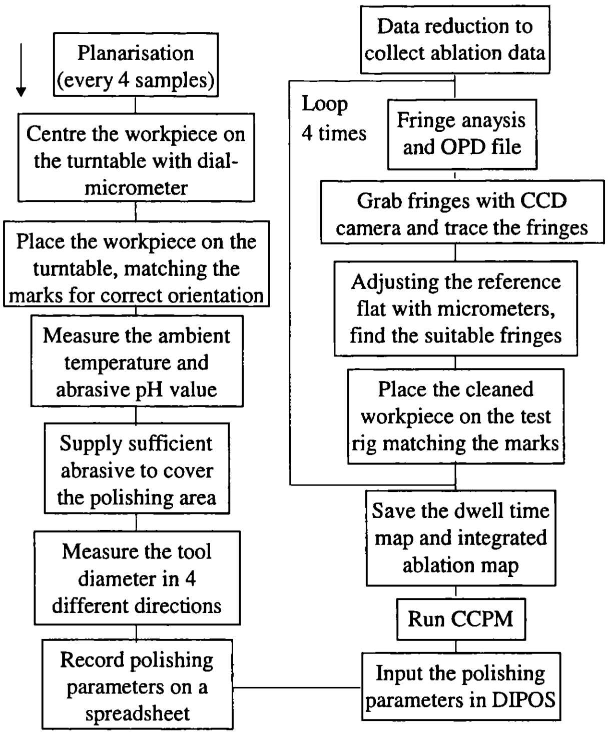

Figure 3.6: Flow chart for the material removal experiment with pitch tool

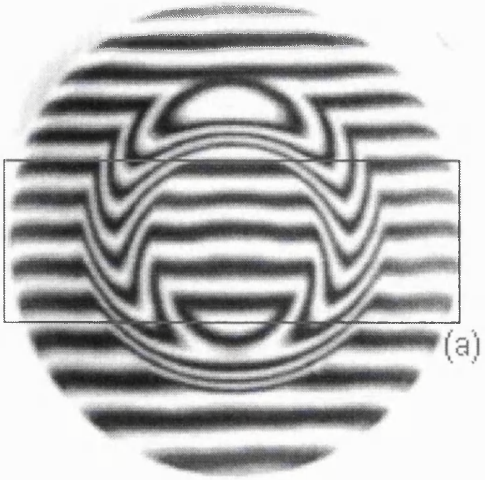

Figure 3.7: Typical fringes showing an annular groove and a horizontal fiducial as a solid rectangle

When the depth of the groove was more than one fringe deep, it was discovered that the software could not comfortably analyse the fringes. Thus the total polishing time for each run was carefully chosen so that with the given set of pressure and speed, four polishing runs could be done on one initial surface without exceeding the limit of the fringe analysis software.

3.6 Data reduction

With the given pressure, speed and integrated dwell time, the material removal rate needed to be data reduced as follows.

3.6.1 Observed material removal data

For either horizontal or vertical fringes, it was found that not whole workpiece area could be analysed with straight line fringes. Analysis could be done safely only at where fringes intersect the groove perpendicularly due to the limitation of the static fringe analysis software. Figure 3.7 shows horizontal fringes with an annular groove. Only the horizontal fiducial like (a) could be used for horizontal fringes to analyse the groove.

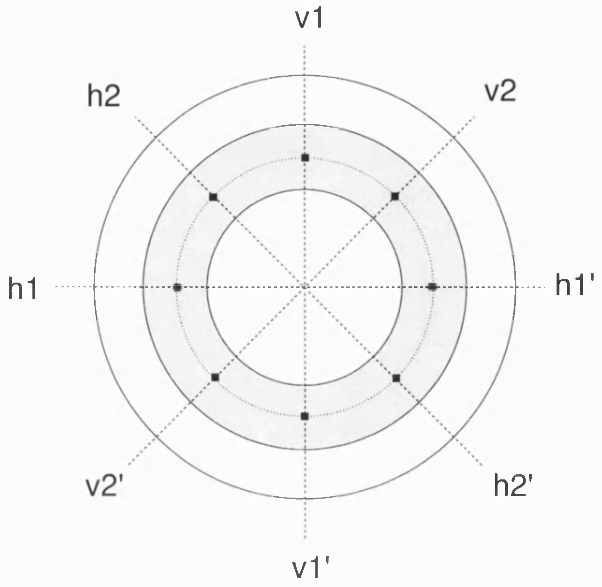

Figure 3.8: Eight sampling points on the workpiece surface

Each fiducial was sized so that it could include four or five fringes. By rotating the workpiece by 45°, four fiducials were used to take eight sample points as shown in Figure 3.8. The eight observation points on the trajectory of the centre of the tool were chosen to calculate the averaged material removal. Since the tool was not touching a sample point continuously during a polishing run, the total material removal on the sample point occurred intermittently. The total amount of material removal was measured as the surface depth of a point subtracted by the depth at the point after one polishing run ($\Delta A = A_{before} - A_{after}$).

During the static fringe analysis, the edges of white fringes were traced. However, due to the limitation to the software algorithm finding the centre of the fringes, the traced points were often two or three pixels away from the true edges of the fringes. Usually the deviation was about ±10% of the half fringe, thus in terms of height difference, about $\pm 0.025\lambda = \pm 14$ nm in height as shown in Figure 3.9.

3.6.2 Removing the residual off-set and tilt

Each measurement of profile had slightly different relative height, i.e. off-set even where no material removal had taken in place as shown in Figure 3.10, such as the middle and edge part of the workpiece. It shows an example of a series of

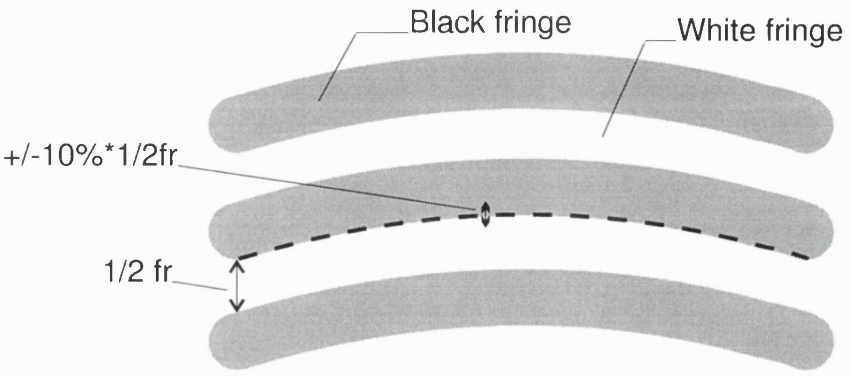

Figure 3.9: Inherent measurement errors with static fringe analysis

profiles where each profile is measured after one polishing run. Annular grooves can be seen near pixel co-ordinate 30 and 90. Different off-sets can be seen for each profile. Although the fringe analysis software removed the tilt term in the OPD, it was discovered that there still remained off-sets. This was due to the slightly different wedge angles formed by the test and reference surface for each testing. In the orthogonal way to the tilt, similar reason was the cause for residual tilts for profile of the surface under the tool.

Figure 3.11 shows the magnified section under the tool (the groove around pixel index 30 in Figure 3.10 before polishing (a), and after polishing (b). By comparing the two base lines of the profiles, not only different off-set but also different tilt can be seen among the profiles. A simple method to remove the off-set and residual tilt was devised as follows and was applied for all polished surfaces to calculate more accurate material removal values.

In each profile, degrees of off-set in y direction are not the same over the x direction. It implies there have been tilt differences in x direction as well for each measurement. In Figure 3.11, line 1 was drawn between the two end points of the profile (a), and line 2 was drawn likewise for the profile (b). The difference (line1-line2) was added to profile (b) to produce the compensated profile (c). Each profile of polished surfaces was compensated to the initial surface for calculation of ΔA.

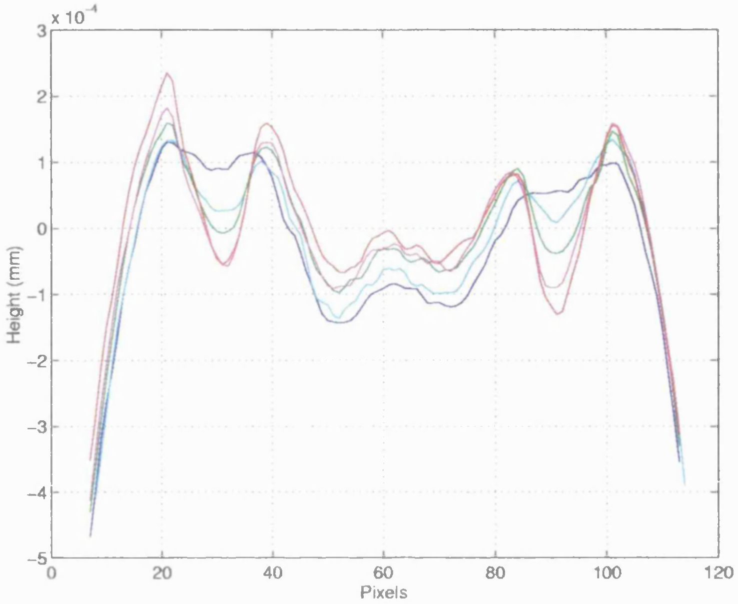

Figure 3.10: Typical consecutive series of cross-sections of polished surfaces

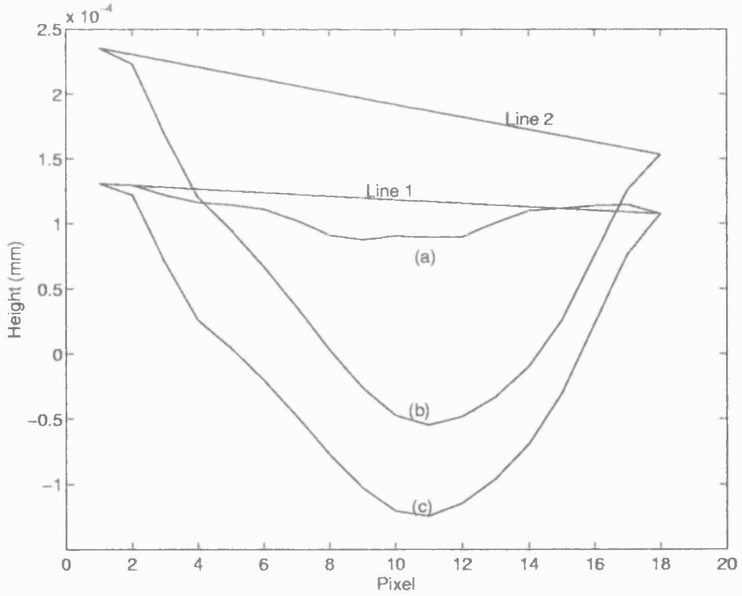

Figure 3.11: Residual tilt and off-set compensation

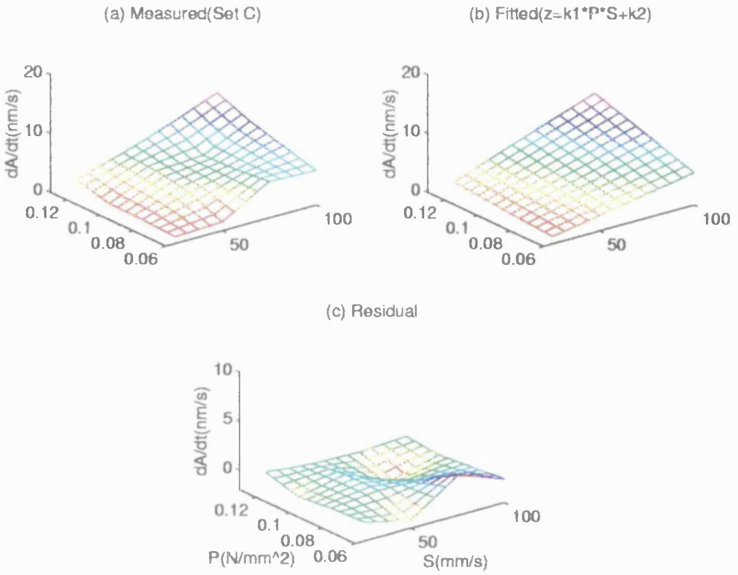

Figure 3.12: Measurement and fitting ($z = kPS$) of material removal rate of the set C

3.7 Results and discussion

Two simple models of polishing were investigated. For each pressure and speed combination, the material removal rate $\Delta A/\Delta t$ was measured as given in Appendix A for the complete material removal rate data and the error analysis. Figure 3.12 (a) for the set C shows an example of the measured material removal rate. The average was taken among the four points on the workpiece for the set A, and increased to eight for the set B and C.

Firstly, the classical Preston's equation, $z = kPS$, was used to fit the measured data. The fitting example of set C is shown in Figure 3.12 (b). Least mean square method was used for the fitting, and the coefficients found are tabulated in Table 3.2. In a previous experiment on a Zerodur glass ceramic sample, the reported material removal coefficient was 5.54×10^{-7} mm^2/N[57], which is in the same order as the k in this experiment, perhaps due to the similar characteristics of the two materials. The residual of the measurement and fitting is plotted in Figure 3.12 (c). The goodness of fitting χ as defined as follows between the measurement and fitting were also tabulated in Table 3.2, which can be a measure of how good the fitting is. For the case of $z = kPS$, the goodness of fitting values in Table 3.2 show that the

	k $10^{-6}\text{mm}^2/\text{N}$	χ nm/s
Set A	0.4559	0.3028
Set B	1.1871	0.5038
Set C	0.9123	0.2887

Table 3.2: Result of fittings to Preston's equation

set C gives the closest fitting.

$$\chi = \sqrt{\frac{1}{N}\sum(\frac{\Delta A}{\Delta t} - z)^2}, \tag{3.5}$$

where $\frac{\Delta A}{\Delta t}$ is the measured material removal rate, z is the fitted value of the material removal rate, and N is the total number of measurement in a set.

Table 3.2 shows that the material removal coefficient k varies from 0.4559×10^{-6}-1.1871×10^{-6} mm^2/N, which has the factor of 2.6 between the maximum and minimum. Provided the material removal coefficient k varies within the maximum and minimum values in this experiment, or within the close range, it implies that the actual polishing can be executed without overshooting a predicted material removal. For example, if the polishing parameters - tool pressure, speed, and polishing time - are planned to remove a certain depth, based on the maximum k in Table 3.2, at least 1/2.6=38% of the target can be achieved, without overshooting the target. Therefore, the minimum material removal prediction accuracy per one polishing run, defined as $\Delta A_{observed}/\Delta A_{predicted}$, is 38%.

However, this material removal prediction accuracy is for the material removal for a point, and there is a clear difference between the form improvement factor introduced in the previous work with the OSL active lap[57], which is the form improvement factor over the whole workpiece surface, and the two can not be directly compared. The form improvement factor per one polishing run was 10% in the previous work.

Secondly, a modified form of the Preston's equation, $z = kP^aS^b$, was used for another fitting. Modelling of the chemical-mechanical polishing (CMP) of semiconductor wafers, which is similar to the glass polishing, had been reported[99] to be empirically successful with an equation $W = kP^{2/3}S$. The idea is to extend this attempt to have another degree of freedom for the other parameter S. By taking the logarithms

	k 10^{-6}mm^2/N	a	b	χ nm/s
Set A	0.7227	0.744	0.7621	0.2836
Set B	3.5709	1.3014	0.9135	0.4399
Set C	0.5717	1.0577	1.1432	0.3834

Table 3.3: Result of fittings to an equation $z = kP^aS^b$

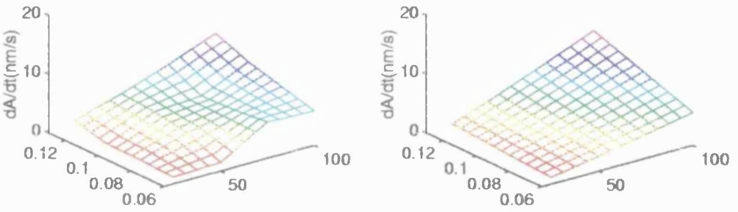
(a) Measured(Set C)

(b) Fitted(z=k*P^a*S^b)

(c) Residual

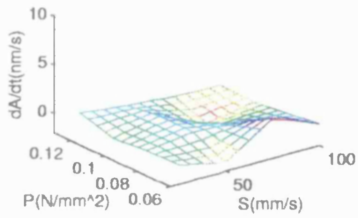

Figure 3.13: Measurement and fitting ($z = kP^aS^b$) of material removal rate of the set C

of both hand sides, coefficient k and powers a and b could be found with the least mean square method as in the previous fitting. An example of the fitting (set C) is shown in Figure 3.13 (b). The coefficients and goodness of fitting for the three sets are shown in Table 3.3, in which each set tends to excel the goodness of fitting with $z = kps$ by up to 10%. However, Table 3.3 can not be used to calculate the prediction accuracy as with Table 3.2, since a and b are different in each set.

The limits of the work in this chapter and suggestions for future work is discussed as follows. The material removal prediction rate observed in this chapter is limited to a point rather than over an area. It needs to be expanded over an *area* to properly control a surface form. The typical material removal rates observed in this chapter were between 0.06-1.2 μm/min (see Appendix A in which the unit is in nm/sec), which is lower than a reported material removal rate of 2.8 μm/min by the magnetorheological technique.[34]

However, the practical material removal rate with the pitch tool polishing in this work is not likely to be as high as 1.2 μm/min, which was resulted by the maximum tool pressure and speed used in this work. The surface roughness was not measured in this experiment, due to the lack of the surface measurement apparatus in OSL. With the interferometer used in this experiment, only the surface form was measured. It could be visible from the naked eye inspection of the interferograms that the surface roughness worsens as the polishing tool pressure increases. Therefore, there is a limit in the polishing pressure to increase the material removal rate while maintaining the surface roughness. For the future work, surface roughness measurement is required.

The material removal rate observed in this chapter is limited for a specific workpiece material. To apply the similar prediction method to other materials, the empirical database for wider range of glass, glass ceramic materials are needed.

Based on the work in this chapter, a novel approach of a polishing tool is demonstrated in the following chapters.

Chapter 4

Characteristics of the spinning compliant tool for polishing aspheric optics

4.1 Introduction

In chapter 3, a sub-diameter pitch tool was used to investigate the material removal for polishing aspheric optics. Traditionally, natural pitch has been the choice of polishing tools for precision optical polishing and figuring.[50] Due to the visco-elastic nature of pitch, the polishing tool made of pitch put on a workpiece slowly flows and conforms to the workpiece and maintains intimate contact with it. However, the speed of conformation is in the order of several hours in room temperature. To produce an aspheric surface which has varying radius of curvature along the surface, a small sub-diameter pitch tool has been used to avoid the radius of curvature mismatch problem between the surface and tool as shown in Figure 4.1.

Figure 4.1 illustrates the mismatch problem of the full-sized pitch tool and an aspheric surface. A full-sized pitch tool is polishing a primary paraboloid mirror. Since the radius of curvature is not uniform throughout the workpiece surface, mismatch occurs when the full size tool is moved across the workpiece surface. The paraboloid surface would be polished into an unwanted figure.

The smaller the size of the polishing tool, the smaller the contact area becomes,

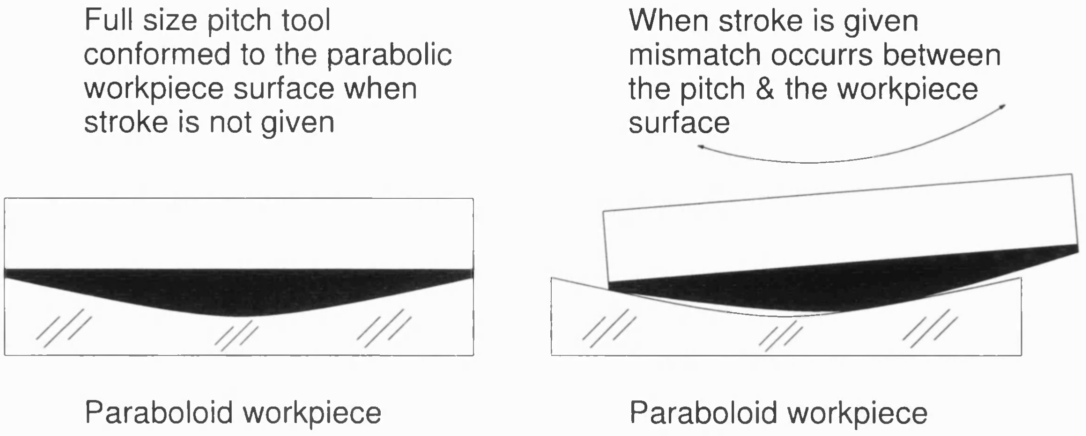

Figure 4.1: Mismatch of conventional pitch tool for aspheric surface

thus the amount of material being removed is smaller and the aspheric surface polishing/figuring process becomes slower.

In this chapter and the following three chapters, development and experiments of a sub-diameter compliant polishing tool hereafter named 'spinning compliant tool' (SCT) are described, demonstrating the feasibility of using such tool for aspheric surface polishing/figuring in terms of surface texture and surface form. The increase in removal rate results from high tool spinning RPM, counteracting the reduced contact area.

Recent research on more compliant material, or fluid, as a polishing tool, such as the magnetorheological polishing[33, 45], and the fluid jet polishing[36, 25] suggest that relatively softer materials than pitch can be attractive alternatives as polishing tools for aspheric optics.

A spinning compliant tool is comprised of a polishing cloth attached to an air/liquid-filled rubber membrane for compliant characteristic, which can be spun rapidly for high material removal rate. In cooperation with OGL, prototype versions of a patented pneumatic tool[117], were built and experimented.

Potential advantages of a spinning compliant tool are the nominally distributed pressure underneath the tool, quicker conformality of the tool, and high removal rate. The distributed pressure can produce grooves with less sharp edges than a pitch tool does. It was suggested in [118] that a tool with Gaussian-like pressure distribution can be useful for optical polishing, giving less high spatial-frequency grooves on the surface. The concept had been derived from an active lap for polishing large astronomical telescope mirrors developed in OSL [54] which can be programmed to give desired pressure distribution underneath the tool.

Without using various pitch tools with different radius of curvature in aspheric optics polishing, one *conforming* tool can be used throughout the polishing process, since the tool shape conforms rapidly to the workpiece shape regardless of the curvature of radius of the workpiece. The rapid conformality also enables rapid rotation of the tool, without scratching the workpiece surface or cracking the tool, hence enables faster removal rate.

From the experiments of the active servo mode pitch tool polishing in the last chapter, the performance requirements for the new polishing tool could be obtained as follows.

Firstly, the new tool should be able to produce higher material removal rate than pitch tool polishing. The results from the last chapter shows that, in order to increase the material removal rate, either the tool pressure or relative speed need to be increased. However, it was also observed qualitatively that increasing the tool pressure ruins the surface texture of the workpiece, than increasing the relative tool speed. Therefore, the tool speed is chosen as the variable to increase the material removal rate, and the tool needs to be spun rapidly.

Secondly, it should be sufficiently compliant to conform to an aspheric workpiece surface, but not too soft so that the tool can give enough pressure for polishing. The varying radius of curvature on an aspheric design requires a compliant material as the tool, which conforms to the local radius of curvature in *ad hoc* nature. The compliance of the tool is also necessary to spin the tool rapidly without producing scratches on the workpiece.

Thirdly, it should give repeatedly, the surface roughness qualities comparable to that of pitch tool polishing. Finally, it should be sufficiently rugged to last the polishing strokes and rapid rotation.

In this chapter, the characteristics of spinning compliant tools proposed in this thesis are analyzed and described through experiments with several compliant tools. Before constructing a spinning compliant tool, the pressure characteristic underneath a non-spinning compliant tool is studied as a theoretical background. The pressure underneath a pitch tool could be assumed to be uniform since pitch is stiffer than the compliant material used in this chapter. However, it is necessary to understand how the pressure is distributed underneath the compliant material to predict the material removal in chapter 7.

A prototype non-spinning compliant tool, which was intended to measure the pressure distribution, was built and tested. The methods for measuring the pressure distribution of various complaint materials were devised and tried. Then a spinning compliant tool and the motor driving electronics were built in cooperation with OGL. For the selection of the polishing cloth, several polishing cloths were experimented with the spinning compliant tool, and the selected cloth was tailored to conform to the spherical surface of the tool. A simulation of the speed map of a tilted spinning compliant tool is also presented, which is later integrated to a polishing simulation software developed for form prediction in chapter 7. Then a prototype of hydraulic spinning compliant tool (HSCT) from OGL, which is used in chapter 6 for surface texture experiments is briefly introduced. With trial polishing experiments with a hydraulic spinning compliant tool, the abrasive slurry particles, polishing cloth used for polishing, and glass debris were investigated with scanning electron microscopes (SEM) and an optical microscope. The changes in abrasive particles and polishing cloth before and after polishing, and the size and shape of glass debris are anticipated to take role in surface texture.

Two spinning compliant tools are used for different experiments in the following chapters. The hydraulics spinning compliant tool and the fixed-pressure (squash ball) spinning compliant tool are used in Chapter 6 for surface texture experiments. The fixed-pressure (squash ball) tool is used in Chapter 7 for surface form figuring experiments.

4.2 Pressure characteristics of compliant tool

Before designing a compliant tool, the pressure characteristics of compliant tools were looked at first. To be able to predict the material removal using compliant tool, it is necessary to understand the pressure distribution of the tool when it is pressed on the workpiece. Although it would be ideal to deal with the dynamic case, taking rotation and strokes of the tool into account in real time, only the static case of the compliant tool pressed on a flat surface is considered here in order to make the problem tractable. Firstly, a mathematical model to estimate the pressure distribution is reviewed and then actual measurements of pressure distribution are discussed in later sections. Finite element analysis of pressure distribution was also proposed but discarded due to time and budget limits. Two models of the compliant tool were used to understand the pressure underneath the tool.

4.2.1 Solid sphere model

Firstly, a model based on a stressed solid cylinder [4] was considered and the pressure model underneath a pressed sphere could be analytically derived from the cylinder's case.

$$p(\rho) = \frac{3F}{2\pi a^3}\sqrt{a^2 - \rho^2}, \tag{4.1}$$

where $p(\rho)$ is the load per unit area, ρ is the radial distance from the centre of the contact area, F is the total load applied on the sphere, and a is the radius of the contact area as illustrated in Figure 4.2. Integration over the contact area gives the total force F. As the Equation 4.1 suggests, the pressure distribution shows an elliptical distribution with maximum pressure at the centre of the footprint.

4.2.2 Spherical shell model

When the tool is a spherical shell with inner pressure, and it is pressed on a flat surface, a model from a shear-stress analysis proposed by Updike [109] can be used. Originally used to calculate the contact pressure distribution for ophthalmic instruments, the same solution can be used for the case of air/liquid-filled rubber ball tools. The vertical load per unit area, or contact pressure p according to [109] is as follows.

$$p = CI_0(k\phi)/R, \tag{4.2}$$

where q is the shell internal pressure, C, k are constants, I_0 is the zeroth order modified Bessel function, ϕ is shell polar coordinate such that $R\sin(\phi) = \rho$, and R

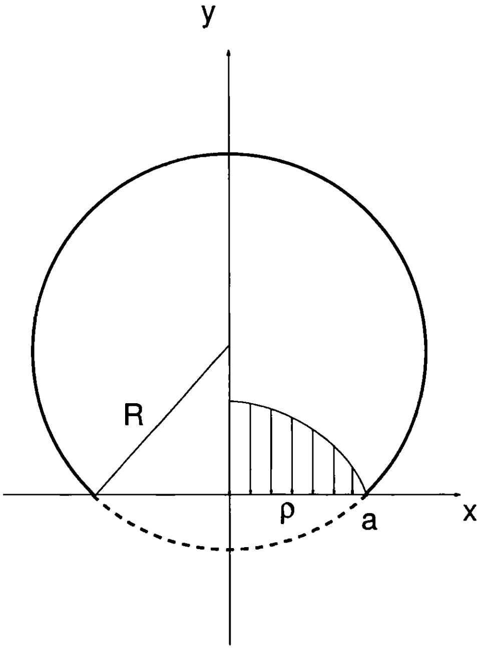

Figure 4.2: Pressure distribution for a solid ball pressed against a flat surface

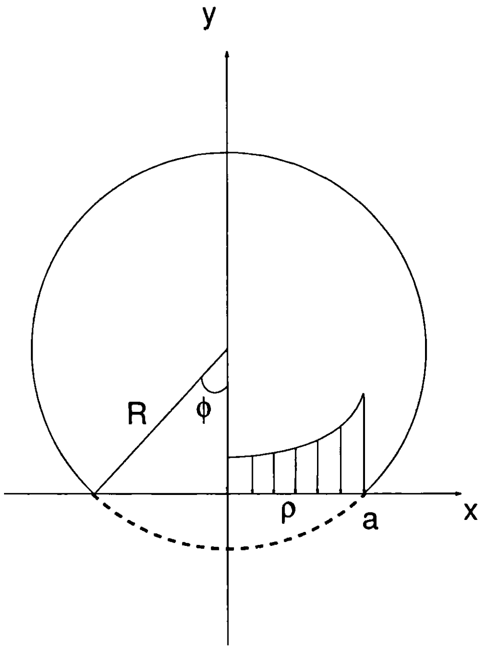

Figure 4.3: Pressure distribution (the zeroth order modified Bessel function) for a shell pressed against a flat surface

is the shell spherical radius as shown in Figure 4.3.

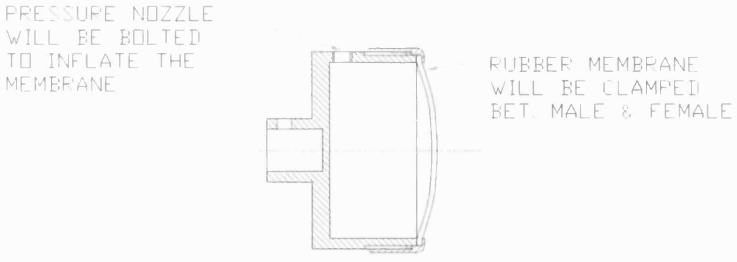

Figure 4.4: Early model of a non-rotating compliant pneumatic tool

Contrary to the previous case of the solid sphere, Equation 4.2 tells that the central region in the contact area has minimum pressure, and the maximum at the edge with a shell type of tool. Although both cases are not taking the movements of the tool nor the effects of polishing cloths on top of the compliant material into account, they can give initial understanding to the pressure map underneath compliant tools. The effects of polishing cloth attached to the compliant tool is investigated later.

4.3 Pressure distribution underneath compliant tools

4.3.1 Inflated membrane compliant tool

In order to actually measure the pressure applied by a compliant tool when it is pressed against a surface, a prototype compliant tool was designed and constructed. The first pneumatic design had an inflatable rubber membrane with an air-tight chamber.

As illustrated in Figure 4.4, the first pneumatic compliant tool consists of an air-tight aluminium alloy chamber and a neoprene membrane to which the polishing cloth is attached. The membrane is inflated by an air pump through a self-locking bicycle tube valve on the wall of the chamber.

After building the tool it was found the volume of the air chamber was too small so that the air escaped the chamber before the valve locked the air. The problem was solved by attaching a bicycle inner tube as a reservoir to the top of the tool body linked by a tubing coil. Thus the total air volume became larger and the air did not

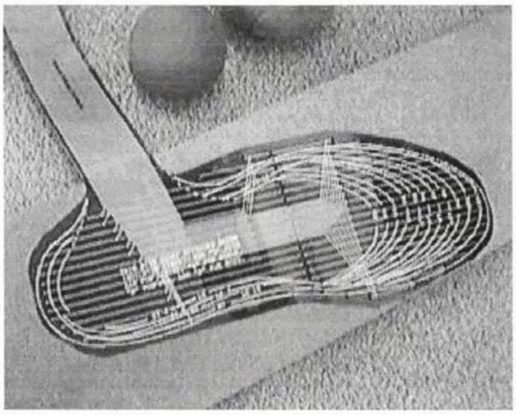

Figure 4.5: 2D foot sensor which can measure the pressure distribution underneath a compliant tool

leak significantly. It was measured that the joint between the membrane and the chamber could endure up to 1 psi of internal air pressure.

4.3.2 Measurement of pressure distribution

After building the first compliant tool with an inflatable membrane, the tool pressure distributions were directly measured. By courtesy of the Department of Podiatry at University of Brighton [6], a foot pressure sensor system [104] was used to measure the pressure distribution of the first compliant tool and some other rubber balls as reference. The picture of the foot sensor which measures pressure in 2D is shown in Figure 4.5. The sensor has a matrix of force sensors with the spatial resolution of 5 mm and has the pressure resolution of 1 kPa (=0.15 psi=$1 \times 10^{-3} N/mm^2$) with measurement error of ±5%.

The first compliant tool (membrane diameter=50 mm, membrane thickness=0.4 mm, internal air-pressure=1 psi=0.007 N/mm^2) and an air-filled rubber ball (diameter=62 mm, rubber thickness estimated less than 1 mm) were pressed against the sensor with different forces. However, the first compliant tool was too soft because the internal air pressure was not high enough to transfer the force to the sensor and no pressure was detectable. Only the balls (sponge balls, air-filled rubber balls) gave readings for the measurement. However, similar to the pressure distribution modeled by Updike, the measurement showed that pressure distribution with an air-

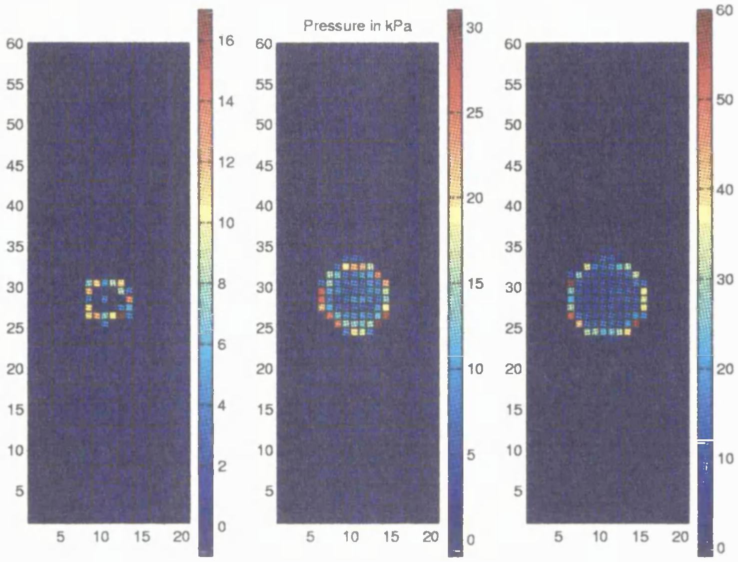

Figure 4.6: Pressure distributions underneath a spherical shell

filled rubber ball (shell) gave distributions with maximum pressure near the edge of the footprint. Figure 4.6 shows a footprint pressure map taken from the sensor with a shell type compliant material. Three pressures (low(173 kPa=0.17 N/mm^2), middle(794 kPa=0.79 N/mm^2), and high(1409 kPa=1.4 N/mm^2)) were used for pressing against the sensor.

The measurement for shell type tool is analysed in Figure 4.7. The pressure values measured in Figure 4.6 underneath the tool are averaged along the radius and plotted. It is clearly shown that the pressure profile is such that the maxima are near the edge of the footprint which agrees with Equation 4.2. It has similar pressure distribution as ring type pitch tools which gives pressure only around the edge of the tool. Ring type pitch tools are usually full size laps, and they are used when only edge region of a workpiece needs to be polished. It would be undesirable to have sharp maximum pressure at the edge of the tool for small tools like compliant polishing tool. It is later shown, with polishing cloths on, the sharp maximum in the edge effect is reduced.

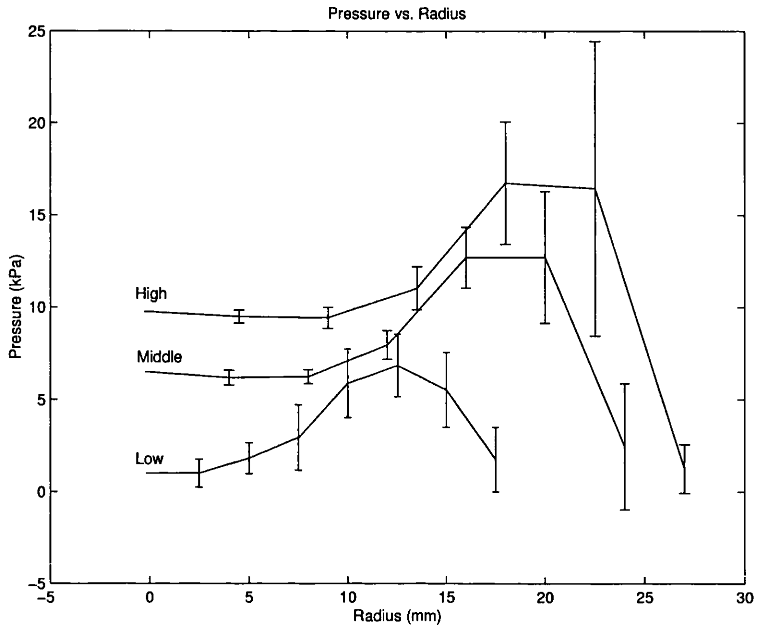

Figure 4.7: Pressure distributions underneath a spherical shell, radially averaged

4.3.3 Spinning compliant tool with one contact pressure

From the measurement of contact pressure by 2D array of pressure sensors, it was reassured that the contact pressure has maximum near the edge of the contact area when a shell type of tool is used. It was also observed that ball type tools can also convey applied load more efficiently, i.e. higher integrated contact pressure(=total load apllied/contact area). Therefore, a spinning compliant tool based on an air-filled rubber ball was made.

Four different compliant materials (air-filled rubber, or sponge balls) were tested to measure the integrated contact pressures, by pressing the balls against a transparent flat glass and measuring the pressing forces and the contact areas. The characteristics of the balls are tabulated in Table 4.1. Three of them are air filled rubber balls with different inner air pressures, and the fourth ball is a solid sponge ball. The compliant balls have been reported[115] that under certain pressure regime, they maintain constant integrated contact pressures. Due to their elastic nature, the contact area increases according to the applied pressure on a compliant ball. Among the four balls with different integrated contact pressures, the squash ball was selected for the surface form figuring experiment in Chapter 7, anticipating high removal rate. In order to rapidly spin the tool, a spinning mechanism was

Tool	Diameter (mm)	Cont. press. (psi)	Composition
Tool 1	39.5	10	Rubber shell
Tool 2	51.5	6.6	Rubber shell
Tool 3	62	4.7	Rubber shell
Tool 4	70	1.5	Sponge

Table 4.1: Characteristics of the balls used as the compliant material

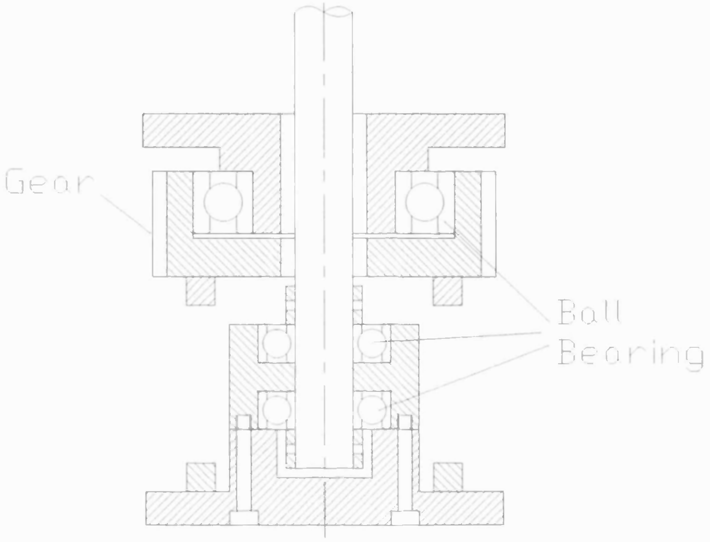

Figure 4.8: Mechanical drawing of the Oldham coupling to minimise the spinning vibration from the polishing rod (designed by E. Herrmann, OSL)

incorporated. A spinning mechanism with Oldham coupling and flat motor was attached to the CCPM polishing head. By transferring the rotating motion indirectly to the compliant tool, the coupling was designed to minimise the influence of rotation vibration to the shaft, which would disturb the CCPM load cells recording polishing pressure. The mechanical concept of the coupling is shown in Figure 4.8.

The controlling electronics for the flat motor was constructed to give maximum rotation speed up to 1000 RPM. Figure 4.9 shows the circuit diagram for the electronics. The rotating tool was calibrated with an optical rotation sensor before each polishing run.

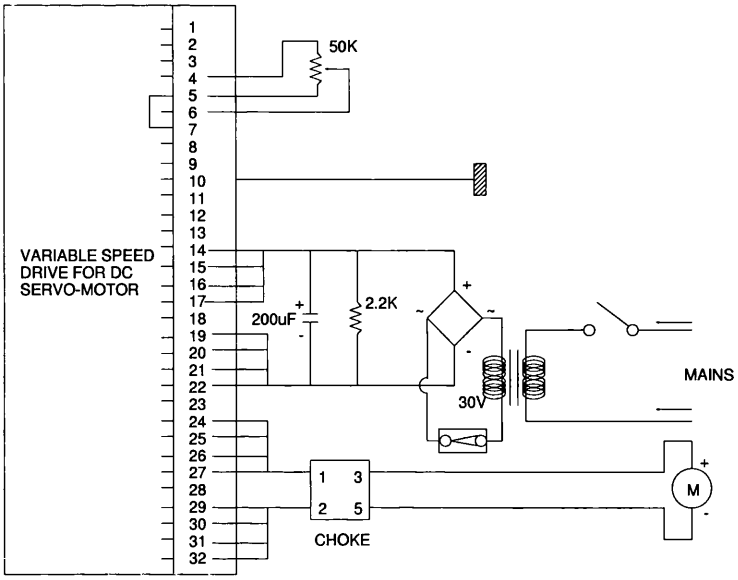

Figure 4.9: Motor drive electronics diagram (designed by D. D. Walker, OSL)

4.3.4 Tilted spinning and the spinning vector calculation

Due to the fast spinning, it was feared that the tangential speed underneath a rotating tool with orthogonal spinning axis would result in radial speed gradients inside the footprint with a central zero. A solution to this problem was to tilt the tool as much as practical to reduce the gradient effect of the speed. With the SaTReC CCPM, the head could be tilted 20 degrees without obstructing the safe polishing with rapid rotation.

Figure 4.10 shows a diagram of a sphere rotating when pressed against the workpiece. The spinning axis (y') is tilted by 20 degrees with respect to the workpiece normal. The ball was regarded as a sphere with a section cut, when it is pressed. Assuming the spinning RPM is more dominant than the stroke speed, so the effect of stroke is negligible to the shape of the ball and the contact area keeps a symmetrical shape, the effective rotation radius ρ could be obtained. An example of comparison between rotation with orthogonal rotation axis and tilted axis is shown in Figure 4.11, when the ball tool has diameter of 40 mm, footprint diameter of 14.5 mm, and 400 RPM rotation with 20 degrees tilt. The detailed mathematics for derivation of the tilted rotation speed map is in Appendix B.

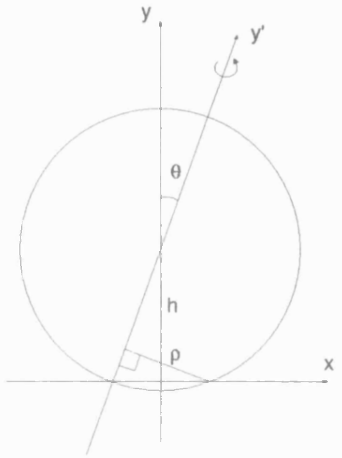

Figure 4.10: A diagram of tool pressed against the workpiece with tilted rotation axis

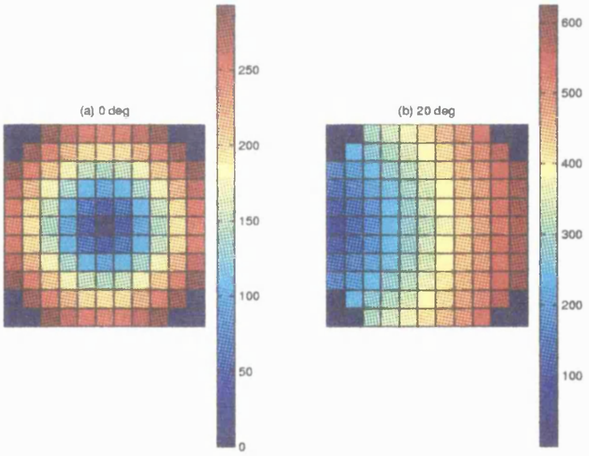

Figure 4.11: Comparison of calculated speed map between up-right and tilted rotation (speed in mm/s)

	Abrasives	R_a after polishing
C1	Silicon Carbide (30 μm)	36
C2	Silicon Carbide (15 μm)	17
C3	Aluminium Oxide (30 μm)	14
C4	Aluminium Oxide (12 μm)	14
C5	Aluminium Oxide (1 μm)	10
C6	Aluminium Oxide (0.3 μm)	21
C7	Chromium Oxide (0.5 μm)	7
C8	Cerium Oxide (2 μm)	10

Table 4.2: Surface roughness results by various polishing abrasive cloth/films with a spinning compliant tool

4.3.5 Polishing cloth selection and tailoring

In order to select the polishing cloth suitable for the spinning compliant tool, a surface roughness test was carried out 8 different kinds of polishing cloth, or bound abrasive films. The requirements for a suitable polishing cloth were, firstly, to produce best surface roughness which is comparable to pitch tool polishing, and secondly, to be sufficiently conformal, so the cloth can cover the spherical shape of the compliant tool.

10 mm patch of each kind of polishing cloth was cut out and attached to the tip of a compliant tool (internal pressure=10 psi), and the tool was rotated on a glass ceramic sample (Astrositall) for 3 minutes with the spinning axis orthogonal to the workpiece surface. Measured by a stylus profilometer[103], Table 4.2 shows the surface roughness values in R_a (see chapter 6 for the details), after the polishing. The average surface roughness of the initial surface was 18.9 μm. The polishing cloth/film coded as C1-C7 are bound abrasive film, and C8 is a velvet-like cloth (Multitex) with externally supplied slurry.

Although the Chromium Oxide (0.5 μm) abrasive film gave the best surface roughness result, it is not suitable for the polishing cloth to be used with the spherically shaped spinning compliant tool. The plastic film was not suitable to cover the sphere smoothly, instead, the second best polishing cloth, the Multitex with Cerium Oxide

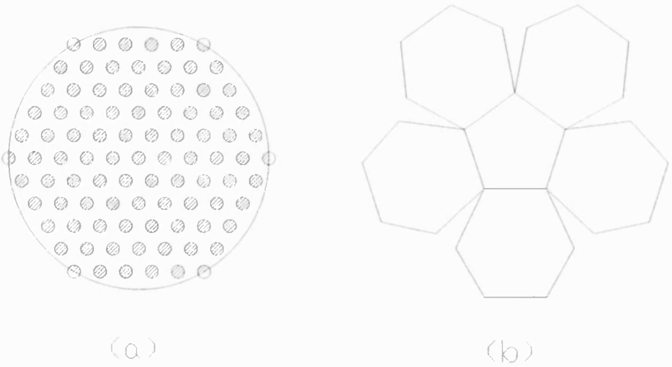

Figure 4.12: Designs of polishing cloth to cover a spherical surface (shaded circles in (a) indicate holes on the polishing cloth)

slurry was selected as the suitable polishing cloth for the SCT polishing.

The selected polishing cloth was cut and attached according to the size of the ball. Multitex is a velvet-like polishing cloth for optical polishing with 1.5 mm thickness and adhesive back paper. Since the tool is a spherical ball and it is used with tilted rotation axis, the cloth was required to cover the 3D spherical surface rather than a small area. However, the thickness of the polishing cloth made it difficult to wrap the sphere and the cloth had to be cut to a certain geometry to cover spheres.

Firstly, a mesh geometry as shown in Figure 4.12 (a), was designed and tried, by punching out various sizes and densities of small holes out from a circular cloth. However, none of the trials cover the sphere without any wrinkle and due to the loss of area on the cloth by punching out, it meant the actual contact area between the cloth and the workpiece was reduced. Conversely, it had been reported [55] that the small patches of the cloth punched out in the punching job had been glued on the spherical surface, without success because the adhesive power of each small patch was not strong enough for rapid rotation strokes and the patches were detached while polishing.

The problem was solved by using a football-like design as shown in Figure 4.12 (b), to give the smoother coverage as well as the larger contact area. A complete tool with polishing cloth attached is shown in Figure 4.13.

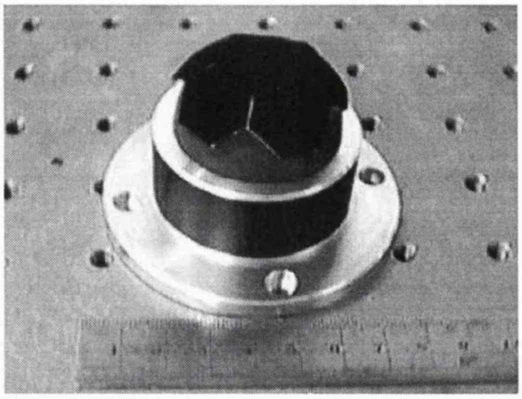

Figure 4.13: A compliant polishing tool with a tailored polishing cloth attached

4.3.6 Pressure distribution with the polishing cloth

In the previous sections, all the pressure distributions were calculated or measured assuming circularly symmetric distributions inside the contact area, and without any polishing cloths attached to the compliant tool. However, in actual polishing - with tool rotation and strokes, the pressure distribution would not be exactly as described previously due to the directional shearing effects on the contacting area of the tool.

In order to understand the pressure distribution closer to the reality, it was measured with the polishing cloth on, and the axis tilted. Although the pressure distribution while the tool was spinning was not possible, the static case was considered to be the closest to the reality.

Since the 2D foot pressure sensor used in the previous section was not available this time, a single load cell pressure sensor rig was constructed used instead. The load cell was calibrated with a known force first, and then was used to measure the 1D profile of the ball-based compliant tool. A metal plate and a housing for the load cell was designed and manufactured so that the force is applied to the sensing part only. Figure 4.14 shows the cross section of the button load cell embedded flush in a test plate with the housing.

The compliant tool was attached to the CCPM and the tool was lowered to press on the sensor with a constant lowering length each time before the tool position was horizontally shifted by 1 mm. Hence the pressure distribution was measured point by point. The voltage reading from the load cell was converted to force, and the

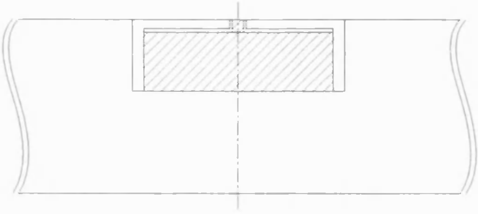

Figure 4.14: Load cell (hatched) with a housing embedded flush in a test plate (the amplifier electronics constructed by H. Jamshidi, OSL)

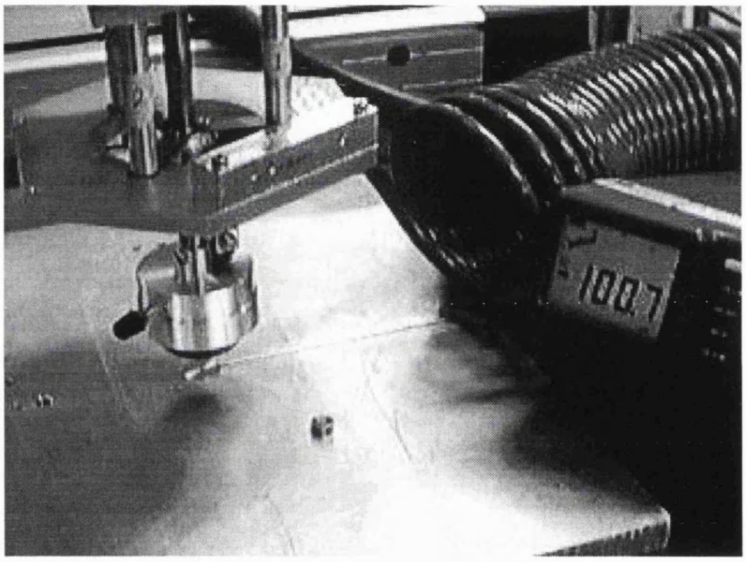

Figure 4.15: Overview of an example of the 1D pressure measurement for a compliant tool (the load cell can be seen below the tool, embedded in the aluminium plate)

force values were divided by the area of the load cell sensing part. The overview of an example of the 1D pressure measurement is shown in Figure 4.15.

A result profile of pressure is plotted in Figure 4.16. It shows less sharp maximum in the edge of the footprint rather than a sharp maximum at the edge proposed and measured in the previous sections without polishing cloths, which was most likely caused by the effect of polishing cloth. With polishing cloths, it is important to notice that the compliant tool has a pressure distribution with more Gaussian-like distributions so the compliant tool can have less furrow effect than pitch polishing tools. This pressure distribution is used in chapter 7 to calculate the material

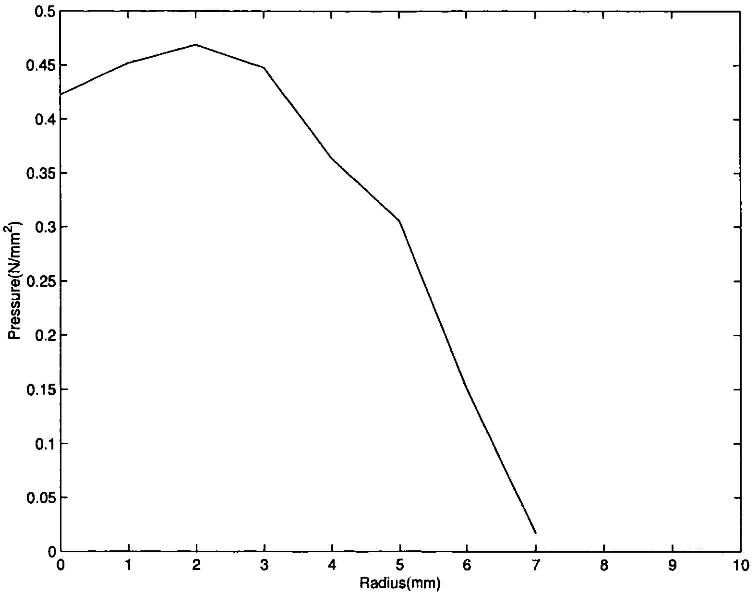

Figure 4.16: Radial profile of pressure distribution of the squash ball-based compliant tool with a polishing cloth attached

removal.

4.3.7 Polishing cloth before and after polishing

The polishing cloth [101] used throughout this thesis was investigated before and after polishing using an optical microscope. Figure 4.17 shows the polishing cloth before polishing. The magnified cloth shows a porous cell feature. Typical size of the cell is between 25-50 μm.

The microscope picture after polishing is shown in Figure 4.18 after several hours of trial polishing with the same polishing cloth (aluminium oxide slurry). It shows that the cell walls are worn and torn out thus the cell size effectively became bigger up to 75-100 μm.

4.4 SEM analysis of abrasive particles with HSCT polishing

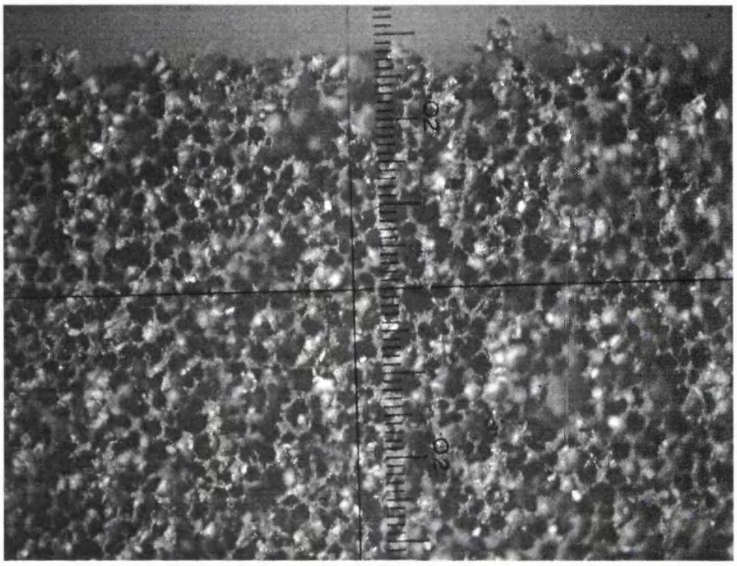

Figure 4.17: A fresh polishing cloth before polishing (1 div.=0.001 inch)

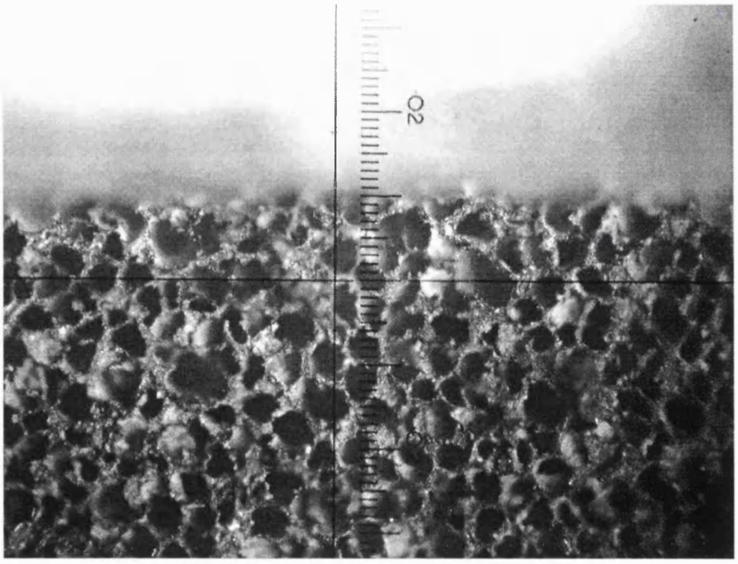

Figure 4.18: A fresh polishing cloth after polishing (1 div.=0.001 inch)

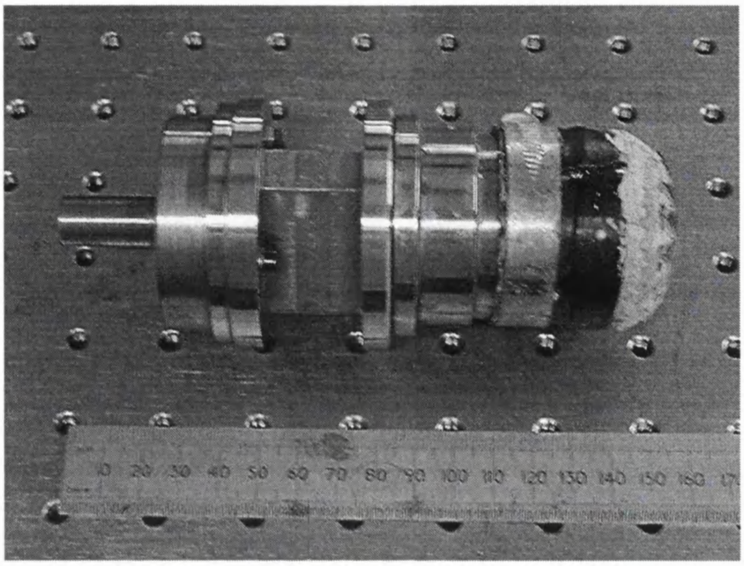

Figure 4.19: View of the hydraulic spinning compliant tool (by courtesy of OGL)

4.4.1 Hydraulic spinning compliant tool

The squash ball tool was designed to give one integrated contact pressure. Another spinning compliant tool as shown in Figure 4.19 was used in this thesis, which was evolved from the fixed-pressure tool, by courtesy of OGL.

Rather than using air as the compliant material inside the rubber membrane, liquid - e.g. silicone oil - was used as the compliant material. Air was replaced by liquid as it is less compressible, and can convey the load more efficiently. With a spring mechanism of applying load to the liquid, the hydraulic tool was designed to provide more than one integrated contact pressure. The schematic illustration of the hydraulic spinning compliant tool is shown in Figure 4.20. By adjusting the adjusting bolt, the spring can apply different load to the piston, thus can apply different polishing pressure instead of one. This tool is used in chapter 6, in order to investigate the surface texture.

In this section, the influence of the hydraulic spinning compliant tool on the abrasive particles was investigated. Scanning Electron Microscopes (SEM) were used to observe the polishing abrasive particles in detail by taking the SEM measurement of the particles before and after polishing. X-Ray analysis with SEM was carried out in order to analyze the composition of the debris after polishing.

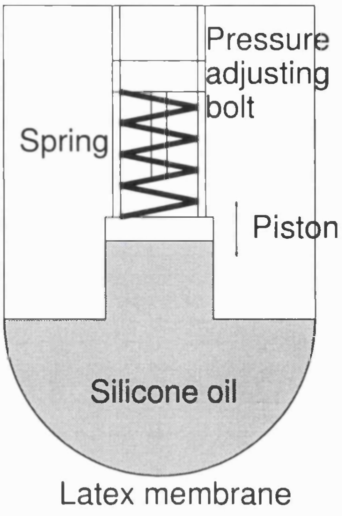

Figure 4.20: Schematic view of the hydraulic spinning compliant tool

4.4.2 Abrasive particles before polishing

Fresh polishing abrasive solution (Regipol 990) was dried and was viewed with Hitachi SEM [38] at different magnifications. According to the datasheet [87], the average particle size is 0.35-0.45 μm. The abrasive particles were put on a special adhesive tape and then it was covered with gold for scanning.

Figure 4.21 shows the SEM images of fresh abrasive particles before polishing. In can be seen that the particles do not have sharp shapes as in diamond abrasives. The highest magnification achieved was ×12000 beyond which the image quality was deteriorated.

4.4.3 Abrasive particles after polishing

The same polishing solution was used to polish a BK7 glass with a tool using a polishing cloth (Multitex). 1 kg force was used for the polishing pressure and the tool spinning of 500 RPM was used. The total dwell time was 30 minutes. The slurry was dried on the workpiece surface after polishing and viewed under SEM. Figure 4.22 shows the images from the abrasive particles after polishing.

It shows that after polishing, the particles seem more coagulated although it does not necessarily mean it is also so during the polishing. However, it was not possible

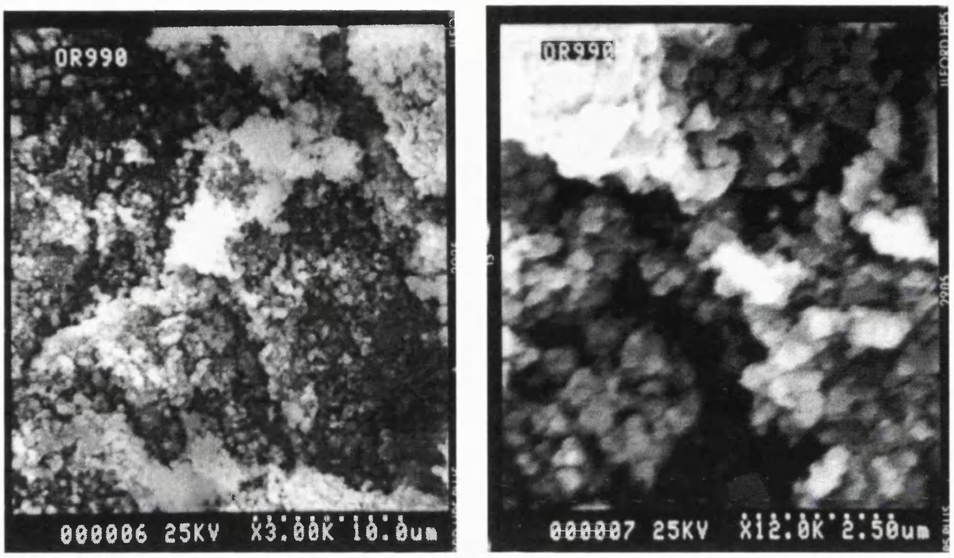

(a) (b)

Figure 4.21: SEM images of polishing abrasive particles *before* polishing: (a) at ×3000, (b) at ×12000

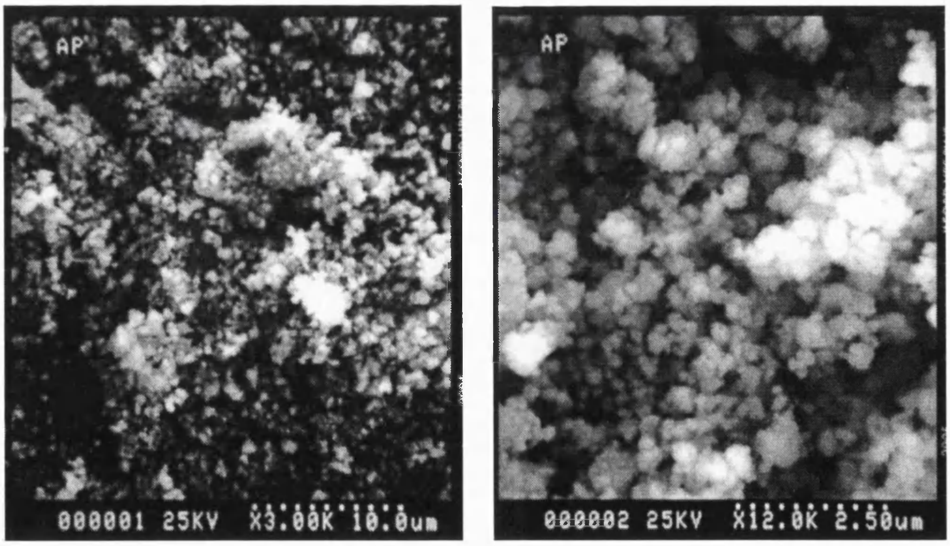

(a) (b)

Figure 4.22: SEM images of polishing abrasive particles *after* polishing: (a) at ×3000, (b) at ×12000

to determine whether there existed any glass debris. In order to distinguish the particles, an X-Ray spectrograph component analysis method was used as described in the next section.

4.4.4 SEM with X-Ray analysis on after polishing abrasive particles

By combining the SEM and X-Ray spectrograph analysis, an SEM image can be identified by the atomic weight of the material under the probe. Jeol SEM [46] was used to carry out the scanning on an SEM image. As the abrasive slurry used contains 55-65% of cerium oxide and BK7 glass contains silicon oxide [87], it was decided to search for cerium and silicon atoms.

The sample was made in two methods. Firstly, small amount of used abrasive particles were put in a resin. The resin was hardened to fix the abrasive particles and polished on the surface to be viewed by the SEM. The idea was to make the sample with scarce population of abrasive particles (and possibly glass debris). However, the image quality was not good with the resin method, and this method was discarded. The second method was similar to the method used in the previous section, except this time carbon was coated for the X-Ray analysis.

Figure 4.23 shows an SEM image at × 3000 with a scale bar of 10.9 μm indicating the scanning length of the X-Ray probe. Figure 4.24 shows the result of the X-Ray analysis in the scanned length. It is showing the mass percentage of cerium and silicon atoms among many other elements. It can be seen that cerium is the majority where total percentage of cerium is 33% and that of silicon is 3%. There are only two noticeable peaks of silicon in the scanned line. The vertical line at one of the peaks in Figure 4.24 corresponds to a short vertical marker in the SEM image of Figure 4.23. In conclusion, the amount of glass removed by polishing is substantially small, which could be scarcely detected with the SEM used.

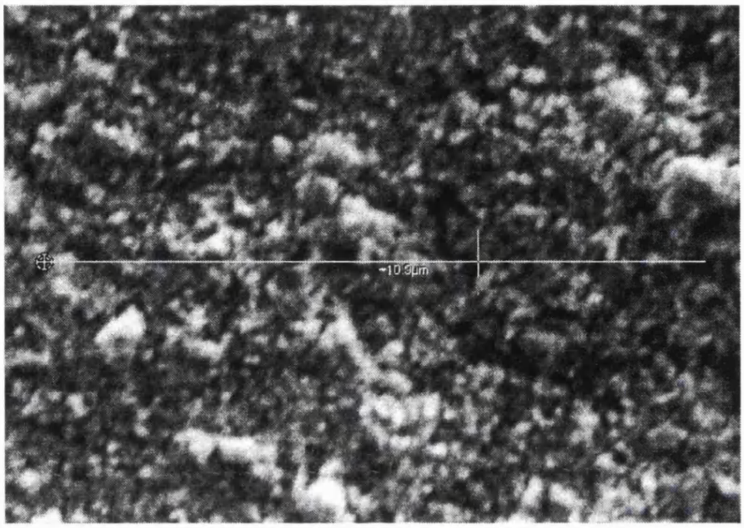

Figure 4.23: SEM image of abrasive particles after polishing at ×3000 and the scanned length

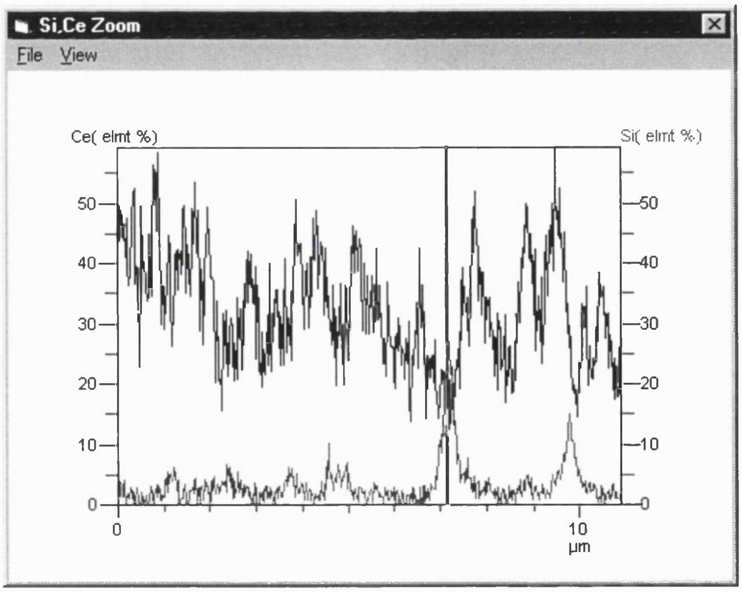

Figure 4.24: X-Ray component analysis of abrasive particles after polishing

Chapter 5

Surface texture simulation for spinning compliant tool polishing

5.1 Introduction

As mentioned earlier in the thesis, there are two major concerns in optics manufacturing, namely the surface *texture* and surface *form* to meet the optics design and tolerances. The former is concerned with microscopic structure of a surface, i.e., the high spatial frequency components of the profile of an optic. The rougher a surface is, the more incident light is scattered and the light energy is diffused in an optical system. It is crucial to have sufficiently smooth surfaces for both refractive and reflective optical elements. With conventional pitch tool polishing, approximately down to 1 nm in R_a can be expected, depending on the detailed polishing regime.

The typical process that controls surface texture area is not fully understood even for pitch tool polishing. However, for a spinning compliant tool - the emphasis of the author's contribution - surface texture was a completely unexplored field.

In the following two chapters, theoretical and empirical aspects in the formation of surface texture are described. In this chapter, the theoretical work is presented.

A microscopic polishing mechanism based on a micro-indentation model is reviewed. Starting from this model, a method to calculate the surface texture (R_a) is proposed, by using an actual abrasive particle size distribution function, which is calculated by fitting the data provided by the abrasive slurry manufacturer.

Then, according to the statistical model, a particle size and thus a groove depth generator is produced, which generates random groove depths following the particle size distribution function. Based on the groove depth generator, a computer simulation software of surface texture is created. By simulating the formation of grooves, the effects of polishing strokes of multi-directions on surface texture are investigated.

5.2 Surface texture by indentation theory

The complexity of the physics of the polishing process makes it difficult to understand the formation of surface texture. As noted earlier, unlike the grinding process, which is mainly a mechanical fracturing process [35, 65], polishing is generally accepted as a mixture of mechanical, thermal, and chemical processes.[60, 105] The mechanical parameters such as the hardness of the glass, abrasive and tool, the shape and the distribution function of abrasive particle size[16, 19, 123], tool pressure and speed [99], and temperature [15], as well as the chemical parameters such as the concentration and the pH of slurry and the zeta (ζ) potential between the glass and the slurry liquid [21] while polishing are thought to play roles in the process. However, there has not been any grand unified theory which combines all the parameters and explains the phenomenon completely, and each account seems to be used when some parameters are more crucial than others.

As unifying all the possible theories of polishing is such an enormous task and beyond the scope of this thesis, a polishing regime when mechanical parameters are more dominant than others is focused. Under such condition, micro-indentation methods [16, 19, 123] have been proposed to explain the tribology of polishing. In particular, based on Bulsara *et al*'s work [16], which proposed a method to relate the total load and abrasive particle size distribution function, a method to predict the surface texture is proposed in this chapter.

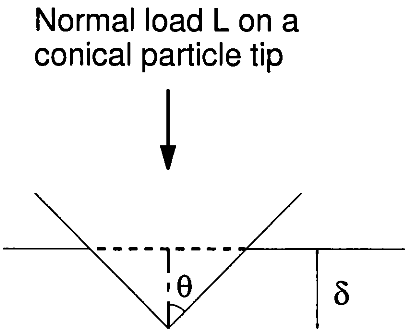

Figure 5.1: Diagram of one conical abrasive particle indenting on the workpiece

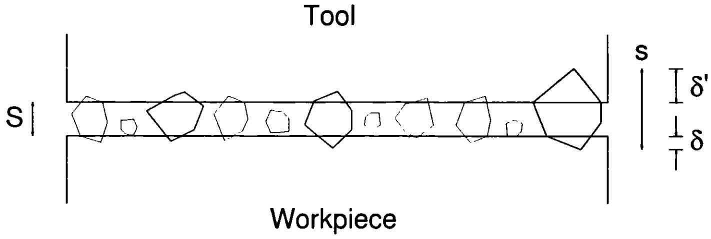

Figure 5.2: Many abrasive particles between the workpiece and tool

5.2.1 Total polishing load and abrasive particle size distribution

From a purely mechanical point of view, optical polishing can be thought of as a two-body and/or three-body [14] abrasive wear process. Starting from the single-particle case, then extending it to N particles, the relationship between the surface texture and other mechanical parameter such as total pressure on the polishing tool can be calculated. Figure 5.1 shows a rigid non-deformable conical indenter, or a particle tip indenting on the workpiece, and Figure 5.2 illustrates many particles between the workpiece and tool.

For one particle, the load L being applied on the workpiece surface and the tool surface can be written as

$$L = \Psi H(\delta \tan\theta)^2 = \Psi H'(\delta' \tan\theta)^2, \tag{5.1}$$

where Ψ is the shape factor (e.g. π for a conical indenter) of the particle tips, H, H' are hardnesses of the workpiece and tool surface respectively, 2θ is the particle tip angle, and δ, δ' are the penetrating depths of the workpiece surface and tool surface respectively. It is assumed that the shapes of the tip indenting both workpiece and tool surface are identical.

From Figure 5.2, the indentation depths have the following relationship:

$$\delta + \delta' + S = s, \tag{5.2}$$

where S is the gap between the workpiece and the tool, and the s is the nominal size of a particle. By combining Equations 5.1 and 5.2, the load L on a particle s_i can be put as

$$L(s_i) = \frac{\Psi H \tan^2 \theta}{(1 + \sqrt{\frac{H}{H'}})^2}(s_i - S)^2. \tag{5.3}$$

When there are N particles between the workpiece and tool, and the largest particle size of the N particle sample is s_L, it can be thought that only the particles with sizes such that $S < s < s_L$ can be "active" in indenting on the workpiece surface, and all other particles smaller than S are not participating in polishing. Therefore, the total load will be distributed and applied on only these active particles so that

$$L_{total} = \sum_{s_i > S} L(s_i). \tag{5.4}$$

Considering a continuous particle size distribution function $\phi(s)$ as the probability density function, the total load transferred to the active particles can be written as

$$L_{total} = \frac{N \Psi H \tan^2 \theta}{(1 + \sqrt{\frac{H}{H'}})^2} \int_S^{s_L} (s - S)^2 \phi(s) ds. \tag{5.5}$$

The total number N of the particles between the workpiece and the tool can be approximated by calculating the volume between the gap volume of As_L, where A is the area of the tool contact, and s_L is the largest among N particles. The volume can be approximated as

$$Ax_L = V_a(1 + \frac{\rho_a}{m\rho_l}) = \frac{N\pi\overline{s^3}}{6}(1 + \frac{\rho_a}{m\rho_l}), \tag{5.6}$$

where V_a is the volume of abrasive particles under the tool, ρ_a and ρ_l are the densities of the abrasive particle and the liquid in the slurry respectively, m is the mass ratio of the abrasive particle over the liquid of the slurry, and $\overline{s^3}$ is the mean cubic particle size, which can be approximated as $\overline{s^3} = \int_{s_{min}}^{s_{max}} s^3 \phi(s) ds$ when N is sufficiently large as discussed by Bulsara *et al.*[16]

Therefore, the total number N of the particles under the tool can be calculated as

$$N = \frac{6As_L}{\pi \overline{s}^3} / (1 + \frac{\rho_a}{m\rho_l}). \tag{5.7}$$

When the probability function is known and there is a total load applied to a polishing tool, the gap S between the workpiece and tool can, in principle, be numerically calculated by solving Equation 5.5, where s_L can be replaced by s_{max} when the sample size N is sufficiently large.

The number of active particles n can be calculated as

$$n = N \int_{s_{min}}^{s_{max}} \phi(s) ds. \tag{5.8}$$

It has been reported [16] that the number of active particles n involved in polishing is typically less than 0.5% of the total number of particles N. It suggests that only a very small portion of particles which are larger than a certain size are actively involved in polishing. The SEM pictures of abrasive particles before and after shown in Figure 4.21 and 4.22 seem to support the theory that not much difference could be observed. It also implies that by providing abrasive slurry which has a more uniform particle size distribution, more active particles can be involved in polishing. With more active particles, the same total load can be distributed to larger number of active particles, and this leads to smaller indentation depths, thus smoother surface texture.

The particle size distribution function, or $\phi(s)$ in Equation 5.5 can be calculated by fitting the cumulative particle size distribution data provided by the manufacturer, to a cumulative particle size distribution function $\Phi(s)$. Figure 5.3 (a) shows an example of cumulative particle size distribution data (circles) for polishing slurry (e.g. Regipol 990 [87]), acquired sedimentologically.

The cumulative particle size distribution data are fitted to a cumulative probability density function $\Phi(s)$ as shown in Figure 5.3 (a) (solid), which is defined as

$$\Phi(s) = \int_{s_{min}}^{s} \phi(s) ds, \tag{5.9}$$

where $\phi(s)$ is the particle size distribution function. The cumulative particle size data of Regipol 990 from the manufacturer shows that the maximum size s_{max} of the particle is 6 μm, but the minimum size s_{min} was not available from the manufacturer

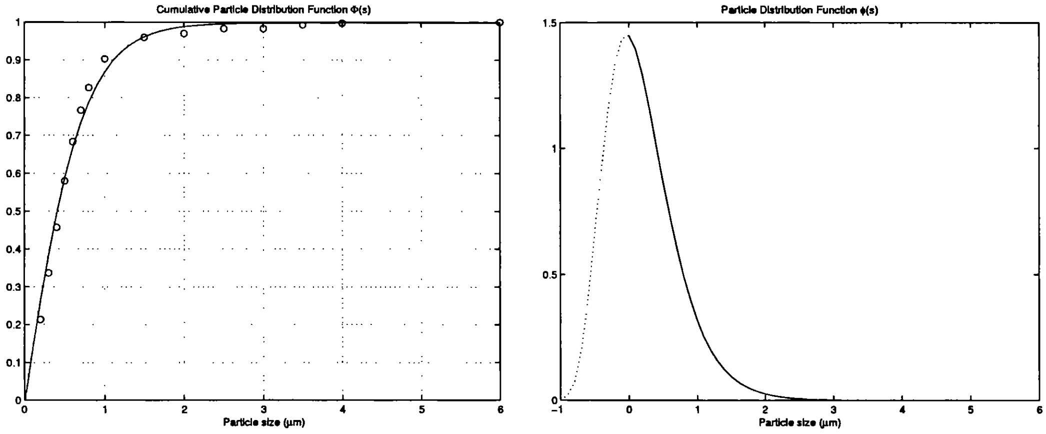

(a) (b)

Figure 5.3: (a) Cumulative particle size distribution data (circles) fitted to $\Phi(s)$ (solid), (b) Particle size distribution function $\phi(s)$

due to the limit of the particle size measurement equipment used. [79] The minimum size s_{min} is assumed to be 0.01 μm, which is close to zero as the trend of the data shows.

A log-normal probability density function is used for $\phi(s)$ as it is known to represent many granulated powders produced by milling fine-grained materials. [93] The bounded log-normal probability function has the form of

$$\phi(s) = \frac{1}{(s-b_1)\sqrt{2\pi}b_3b_4} e^{-\frac{1}{2}\left(\frac{\ln(s-b_1)-b_2}{b_3}\right)^2}, (s > b_1) \tag{5.10}$$

and it also satisfies $\int_{s_{min}}^{s_{max}} \phi(s)ds = 1$ as the particle size is bounded between the s_{min} and s_{max}. As $\Phi(s)$ is a non-linear function, Nelder-Mead simplex algorithm [73] is used to fit the provided cumulative particle distribution data to $\Phi(s)$, and thus the coefficients b_1, b_2, b_3 and b_4 of $\phi(s)$ are calculated. Figure 5.3 (a) (solid) shows the well fitted function such that 95% (in weight) of the particles are smaller than 1.2-1.7 μm, which agrees with the data sheet.

Figure 5.3 (b) shows the resulting $\phi(s)$ of Regipol 990 abrasive slurry, and the average particle size is in 0.35-0.45 μm range as it is confirmed by the manufacturer's data sheet. Notice that the probability density function for abrasive particle size is not symmetrical over its peak, hence the mean is not at the peak. (The negative particle size part is shown in dotted line to show the asymmetry.)

5.2.2 Calculation of surface texture

Equations 5.1 and 5.2 also lead to the equation of $\delta(s)$ for one particle as

$$\delta(s) = \frac{s - S}{1 + \sqrt{\frac{H}{H'}}}, (s > S) \tag{5.11}$$

and this can be used to calculate the surface texture polished with particle size distribution $\phi(s)$. The average absolute surface texture R_a of the polished surface can be defined as

$$\begin{aligned} R_a &= \frac{1}{N_x N_y} \sum_x \sum_y |\overline{z} - z(x, y)| \\ &= \frac{1}{N_x N_y} \sum_x \sum_y |\{\overline{z_o} - \overline{\delta}\} - \{z_o(x, y) - \delta(x, y)\}| \\ &= \frac{1}{N_x N_y} \sum_x \sum_y |\{\overline{z_o} - z_o(x, y)\} - \{\overline{\delta} - \delta(x, y)\}|, \end{aligned} \tag{5.12}$$

where N_x, N_y are numbers of particles in x, y directions giving $N_x N_y = N$. $z(x, y)$ is the height on the workpiece on the contact area, and $\overline{z}$ is the mean, *after* polishing. Similarly, $z_o(x, y)$ and $\overline{z_o}$ are the original height and the mean on the contact area, *before* polishing.

When the absolute average of the original surface height before polishing, and the absolute average of the indentation depth δ are defined respectively as

$$(R_a)_o = \frac{1}{N_x N_y} \sum_x \sum_y |\overline{z_o} - z_o(x, y)|, \tag{5.13}$$

$$(R_a)_\delta = \frac{1}{N_x N_y} \sum_x \sum_y |\overline{\delta} - \delta(x, y)|, \tag{5.14}$$

from Equations 5.12, 5.13, 5.14, the lower limit of R_a is decided such that

$$R_a \geq |(R_a)_o - (R_a)_\delta|. \tag{5.15}$$

(Note that $|\sum |A| - \sum |B|| \leq \sum\{|A| - |B|\} \leq \sum |A - B|$.)

However, as more polishing is applied, the $(R_a)_o$ is gradually reduced by $(R_a)_\delta$, until the final R_a reaches the ideal limit, which is $(R_a)_\delta$, when $(R_a)_o \to 0$. Therefore, the final surface texture can be considered converging to the absolute average of the indentation depths, so that

$$R_a \to (R_a)_\delta, \tag{5.16}$$

provided the workpiece surface is sufficiently polished with known abrasive particle distribution.

$(R_a)_\delta$ from 5.15 was defined over the points (x, y) on the contact area. However, as only the *active* particles participate on indenting on the workpiece, $(R_a)_\delta$ can be re-written as the function of particle size distribution as follows.

$$(R_a)_\delta = \frac{1}{N}\sum_{s_i > S} |\overline{\delta} - \delta(s_i)| \rightarrow \int_S^{s_L} |\overline{\delta} - \delta(s)|\phi(s)ds, \tag{5.17}$$

where $\overline{\delta}$ is the mean value of $\delta(s)$ over N particles. $\overline{\delta}$ can be calculated as $\int_S^{s_L} \delta(s)\phi(s)ds$.

In Equation 5.17, $(R_a)_\delta$ is described as a function of the indenting $\delta(s)$ on the workpiece surface, the largest particles size s_L under the tool, and the gap S between the workpiece and the tool. Also, due to the gap S, which can be numerically found in Equation 5.5, $(R_a)_\delta$ is a function of the total load L_{total}, the hardness values of the workpiece and tool (H and H'), particle shape (Ψ and θ), and the total number N and size distribution $\phi(s)$ of active particles.

Therefore, the final surface texture R_a is a function of the initial surface texture, the tool load, workpiece and tool hardnesses, and the number of abrasive particles on the contact area as well as the particle geometry and size distribution.

The assumptions made in the above derivation are:

1. The abrasive particles have identical shapes and indentation angles (Ψ and θ), and no coagulation of the particles occurs while polishing.
2. The abrasive particle size follows the calculated particle size distribution function $\phi(s)$, but the particles are spatially well dispersed on any point (x, y) under the contact area.
3. The total number, N, of abrasive particles underneath the contact area is sufficiently large.
4. No polishing strokes are given, and thus sliding indentation or rolling of the abrasive particles are not taken into account for the calculation of the surface texture.
5. The workpiece, abrasive particles, and tool are not elastic, and the formation of δ is a plastic deformation.

The numerical calculation of S and $(R_a)_\delta$ are left for the future work. An average particle shape (θ) can possibly be obtained by measuring the θ from the SEM photographs of the particles. For brittle materials, the hardness is measured by the length of the impression when an indentation tip is pressed on the material (e.g. Knoop hardness [95]). However, the hardness information usually given by the manufacturer of the polishing cloths is measured in different method, as the material used in polishing cloths such as polyurethane is elastic. The hardness of elastic material is usually measured by the rebound length of a projectile bounced off the material (e.g. Shore scleroscope hardness [9]).

The hardness values (H, H') required for the calculation of $(R_a)_\delta$ need to be compatible. The measurement of the hardness for a polishing cloth, which can be measured in a nano-indentation testing equipment, is beyond the scope of this thesis, and it is left as the future work.

Also, for the further development of the surface texture theory for a spinning compliant tool using polishing cloths, the elasticity of the polishing cloth needs to be considered. Figure 5.4 shows the cross section of an unused polishing cloth (Multitex [101]). It shows the porous feature. However, as the pore part is made of polyurethane, pressed pores would transfer the polishing load in an elastic way. Figure 5.5 illustrates a porous type polishing cloth with a load and a stroke applied.

5.3 Simulation of surface texture

5.3.1 Particle size generator function

With the particle size distribution function $\phi(s)$, and thus the cumulative particle size distribution function $\Phi(s)$ calculated from the previous section, it is possible to build a particle size generator function, which generates particle sizes according to the particle size distribution function. This generator function can be used to generate the indentation depth $\delta(s)$, and this leads to a simulation of sliding indentation producing grooves. Therefore, the surface texture when a stroke is given can be simulated.

Given the cumulative particle size distribution function, $y = \Phi(s)$ has the range of

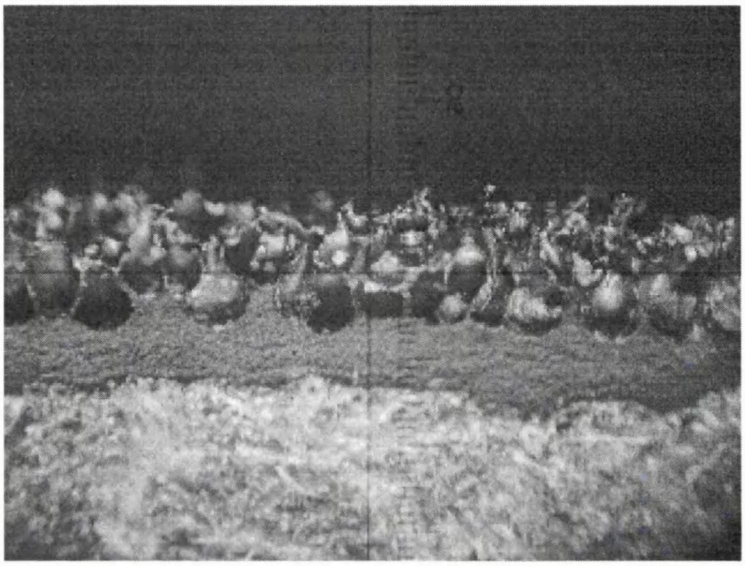

Figure 5.4: A cross section of the porous polyurethane polishing cloth (1 div.=25.4 μm)

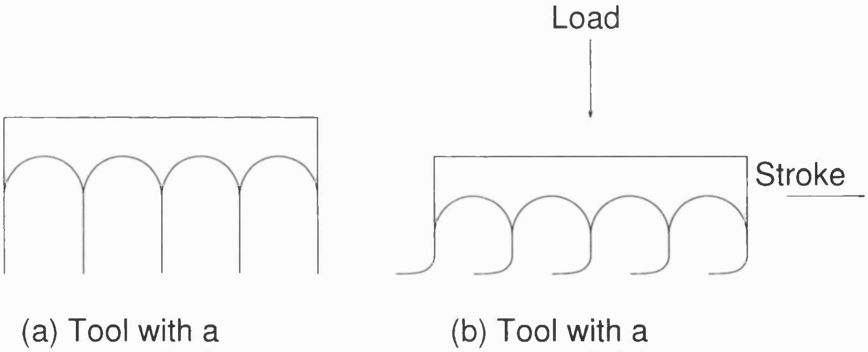

(a) Tool with a porous polishing cloth not loaded, not given a stroke

(b) Tool with a porous polishing cloth loaded and given a stroke

Figure 5.5: Exaggerated illustrations of porous and elastic polishing cloth when given a load and a stroke

$0 \leq y \leq 1$. If the inverse function, $s = \Phi^{-1}(y)$ can be calculated, and a uniformly random number of y in the range of $0 \leq y \leq 1$ is fed as an input to the inverse function, the particle size can be generated according to the particle size distribution function $\phi(s)$.

From the definition of $\Phi(s)$ (Equation 5.9), it can be rewritten as

$$y = \Phi(s) = \frac{1}{2b_4}[\mathrm{erf}\{\frac{\ln(s - b_1) - b_2}{\sqrt{2}b_3}\} - \mathrm{erf}\{\frac{\ln(s_{min} - b_1) - b_2}{\sqrt{2}b_3}\}], \tag{5.18}$$

where erf(s) is the error function defined as $\mathrm{erf}(s) = \frac{2}{\sqrt{\pi}} \int_0^s e^{-t^2} dt$, which is commonly calculated in mathematical software packages. The second term in Equation 5.18 can be put as a constant C, and the inverse function can be calculated as

$$s = \Phi^{-1}(y) = b_1 + e^{b_2 + \sqrt{2}b_3 \mathrm{erf}^{-1}(2b_4 y + C)}, \tag{5.19}$$

where $\mathrm{erf}^{-1}(y)$ is the inverse error function from $y = \mathrm{erf}(x)$. Therefore, when a random y_i for an ith particle, which can be picked from a uniform distribution of y within [0,1], the particle size s_i can be generated according to the particle distribution function $\phi(s)$. Consequently, the indentation depth $\delta_i(s)$ is generated, and when this particle is swept, this leads to the depth of the groove.

5.3.2 $N_x \times N_y$ particles matrix model

With the particle size generator function, the depth of indentation $\delta(s)$ from Equation 5.11 can be obtained with the calculation of S from 5.5 and the information of hardness (H, H'). As only the active particles participate in indentation, s generated by Equation 5.19 only contributes to $\delta(s)$ when $s > S$. However, as H/H' is not available at the moment, $\delta(s)$ is thought as a small fraction of s. For example, when the indentation is 1% of the particle size, $\delta_i = \frac{s_i}{100}$ can be used instead of Equation 5.11.

Assuming the particles are not coagulated, and are spatially uniformly dispersed underneath the contact area, a tool which has a matrix of particles whose sizes follow $\phi(s)$ is simulated.

Consider an $N_x \times N_y$ matrix as shown in Figure 5.6, which gives an indentation depth for each particle according to $\phi(s)$. Only the particles larger than the gap S

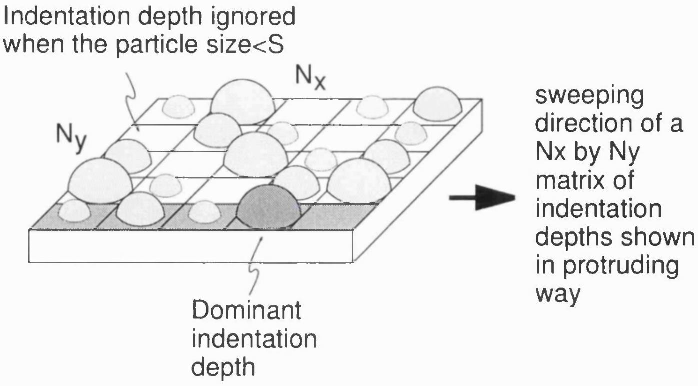

Figure 5.6: An example of $N_x \times N_y$ matrix of abrasive particles whose sizes follow $\phi(s)$

between the workpiece and the tool are active in producing the indentation depth.

If the matrix is swept in one direction along the rows, sliding indentation by each particle produces a groove. Considering a row of particles swept in a longitudinal way, it is assumed that the final depth of the groove is decided by the maximum indentation depth. For instance, when the particles of the front row of Figure 5.6 is swept longitudinally, the largest indentation depth is the dominant indentation depth δ_i of the row. The differences in indentation width, thus groove width, according to groove depth is not considered.

A 100×100 matrix of indentation depths is produced to simulate the grooves by one stroke. Each δ_i is generated using the particle size generator, Equation 5.19. Although S from Equation 5.5 can not be obtained explicitly in this work due to the incompatibility problem with hardness values, S is calculated from Equation 5.8 assuming the number of the active particles is 0.5% of the total number of the particles, which is 2.3 μm with the given $\phi(s)$ of Regipol 990. Thus, the indentation depth δ_i of particle size s smaller than S can be ignored in the matrix.

For each row, the dominant particle is found, and this particle decides the removal profile, thus the profile of grooves is produced. An example of simulated grooves is shown in Figure 5.7. It can be seen that some point on the removal profile are zeros where none of the particles in the row are larger than S.

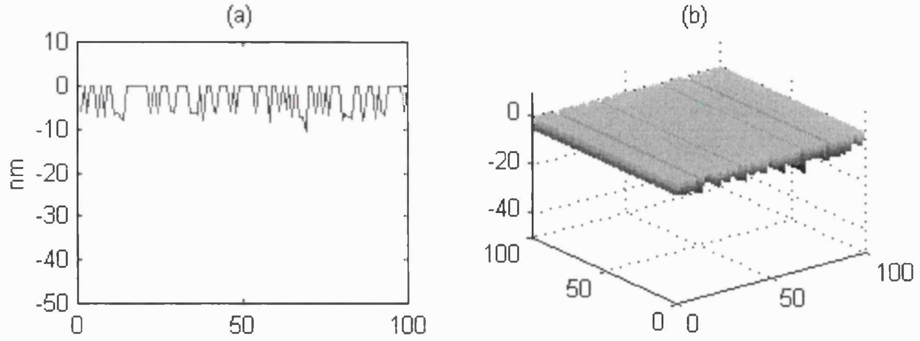

Figure 5.7: Grooves simulated by one-stroke polishing of $N_x \times N_y$ abrasive particle matrix on a perfect flat: (a)removal profile, (b)grooves in 3D

5.3.3 Multi-directional polishing

When strokes are given in real polishing, they are usually given in a multi-directional way to ensure smoother surfaces. However, it is not clear how the surface texture reaches a limit, and what effects the different directions of polishing have on the surface texture is not intuitive. If several groove simulations in the last section can be imposed on one another with different polishing directions, the effect of multi-directional polishing can be simulated. The change of direction $\Delta\theta$ of the next polishing run on an existing groove can be assigned with different values and the effects on the susrface texture can be simulated. This information is of particular interest for the spinning compliant tool, whose spinning axis can be tilted and then precessed in an effort to achieve better surface quality.

In the last section, a simulated removal profile caused by sliding indentation of the abrasive particles was applied on a perfectly flat surface. However, when the workpiece surface is not perfectly flat (e.g. when a second stroke is applied on the surface polished with the previous stroke), the peaks of the surface is more likely to be polished than the valleys, depending on how deeply the abrasive particles are touching down into the valleys. This hypothesis can be implemented by matching the zero level of the removal profile with the peak of the surface. If the valley is deeper than the removal depth, the surface is untouched, thus only the peaks are removed. In Figure 5.8, a removal profile (solid) and the surface (dotted) are illustrated, where the centre part of the surface is not being polished.

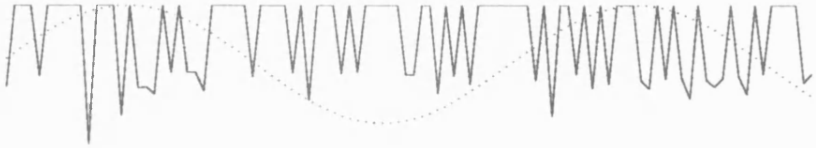

Figure 5.8: A removal profile (solid) applied on workpiece profile (dotted), and the middle part is not removed

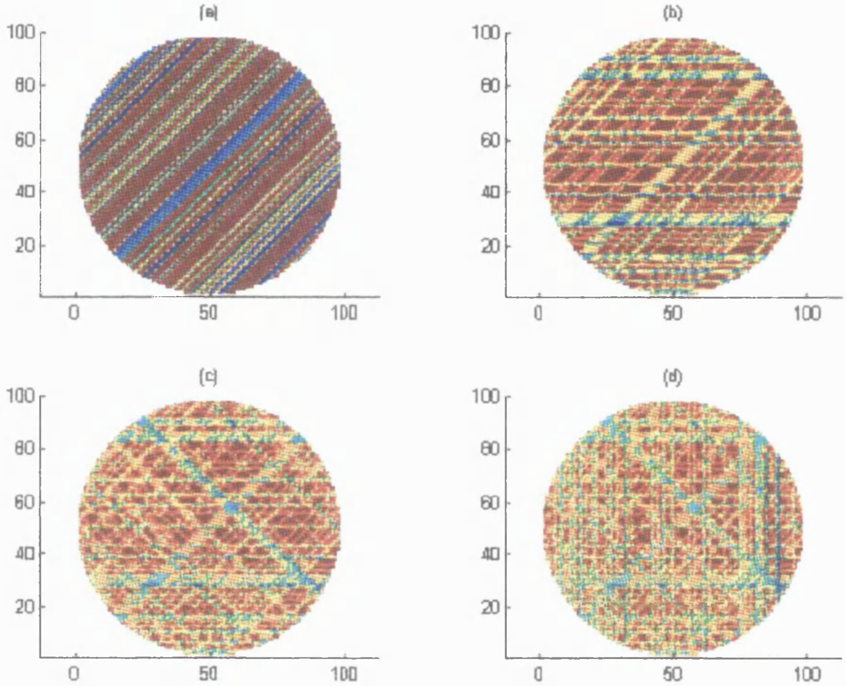

Figure 5.9: Grooves simulated by multi-directional polishing of $N_x \times N_y$ abrasive particle matrix with 45° differences in directions (in alphabetical order)

In order to simulate multi-directional polishing, the $N_x \times N_y$ removal profile matrix needs to be rotated, and only the inscribing circular part of the matrix is considered. Figure 5.9 shows the simulation of 4 consecutive polishings applied with different directions by 45° ($\Delta\theta = 45°$).

In Figure 5.10, one-directional polishing and multi-directional polishing are compared, by setting $\Delta\theta = 0°$ and 45° respectively. Also, the numbers of polishing runs are increased, and the surface texture R_a values can be seen to reach lower limits as mentioned in formula 5.16.

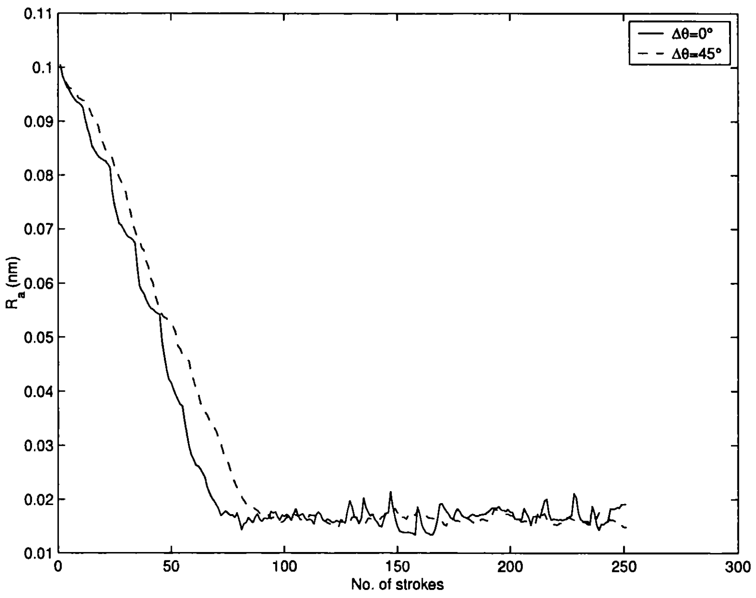

Figure 5.10: Surface texture R_a against number of polishing strokes with $\Delta\theta = 45°$

Figure 5.10 shows that when there are only one-directional polishing sweeps with random removing profile for each sweep calculated from $\delta(s)$, the surface texture reaches the lower limit faster than the case when there are multi-directional sweeps. This is because the simulation is based on an assumption that the second stroke on an existing groove removes the peaks only as shown in Figure 5.8. When the direction of the second stroke is identical to the first one, it can remove the whole lines of peaks more effectively than a different direction.

Figure 5.10 also suggests that the average lower limits of the two polishing schemes are virtually same as the lower limit is the same, decided by the groove depth $\delta(s)$ distribution. However, it can be seen that the one-directional polishing gives more variant lower limit.

By using different $\Delta\theta$ values, the effect of multi-directional polishing on surface texture is investigated. Figure 5.11 shows the surface texture in R_a. It can be seen that the surface texture produced with different $\Delta\theta$ $(=22.5, 45, 90°)$reach the same lower limit of R_a and the converging speeds do not differ significantly. It can be interpreted that as long as the polishing direction is changed ($\Delta\theta \neq 0°$), the rates of R_a decreasing towards the limit are not decided by $\Delta\theta$ and are virtually the same.

This can be applied when a spinning compliant tool axis is tilted and precessing discretely on the workpiece. Figure 5.11 suggests that in the case of discrete prescession

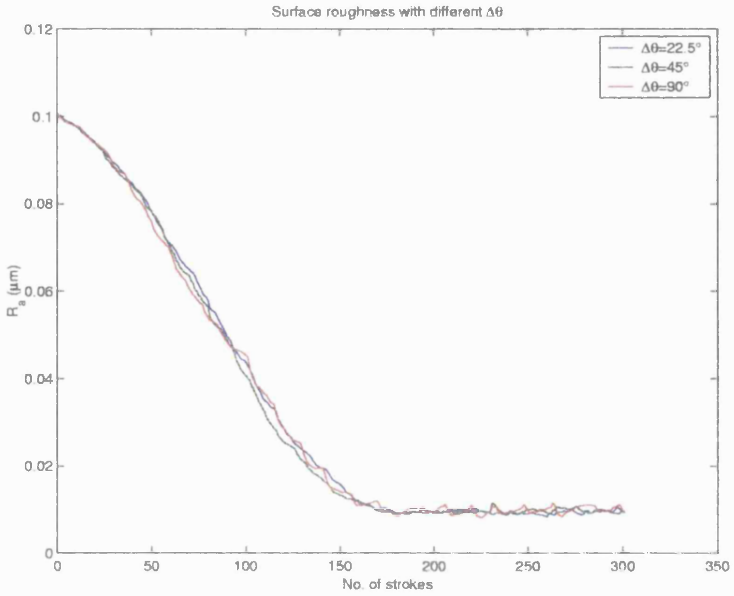

Figure 5.11: Surface texture R_a plotted for multi-directional polishing with different $\Delta\theta$

of the spinning compliant tool, the precession angle $\Delta\theta$ of the spinning axis may not be significant to the surface texture in terms of the rate of decrease towards the limit, and the value of limit.

Chapter 6

Surface texture experiment with spinning compliant tools

6.1 Introduction

In the last chapter, theoretical studies and simulations were presented. In this chapter, actual polishing experiments were carried out to investigate the relationship between the surface texture and several parameters associated with spinning compliant tools, and the experiment results suggest how to reduce surface texture more efficiently with spinning compliant tools.

Two sets of experiments are reported. One is polishing with a spinning compliant tool on a tool on an experimental rig based on a pillar drill, which does not give any lateral strokes, and the other is polishing with the prototype CCPM used in Chapter 3 to give lateral strokes with a spinning compliant tool.

In the former, or the no-stroke experiments, the effects of one-directional and discrete precession polishing were investigated, referring back to the surface texture simulation from the last chapter. Then, the effects of two different polishing pressures with discrete precession polishing were investigated.

For the latter experiment, using the CCPM, multi-directional polishing experiments were carried out by giving strokes instead of precessing the tool. Various spinning RPM were investigated for surface texture values. For both sets of experiments,

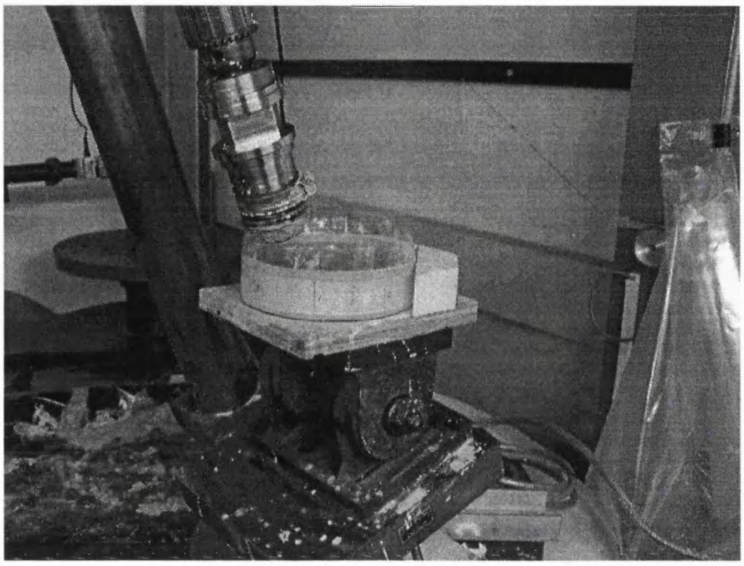

Figure 6.1: Pillar drill set up for spinning compliant hydraulic tool polishing experiment

surface texture was measured using the WYKO RST500 phase-shifting interferometer(PSI) surface texture measuring instrument.[114]

6.2 Surface texture experiment with SCT on drill machine

6.2.1 Polishing experiment set-up

A drilling machine was used to spin the OGL's compliant hydraulic tool, as shown in Figure 6.1. The tool was applied with 40.8 kPa (High) and 21.4 kPa (Low) as the polishing pressure. An ordinary pillar drill was tilted 20 degrees and the table for the workpiece was kept horizontal using a spirit level. The tool was lowered on the centre of the workpiece to have approximately 1.2 mm of footprint diameter and polished without any stroke but only with spinning of the tool. The tilted spinning tool also gave more nearly linear groove patterns than a spinning tool with an up-right spinning axis as shown in Figure 6.2.

In a past experiment using a rotating tool with the polishing head in up-right position, it was reported that the tool mark on the workpiece had concentric rings

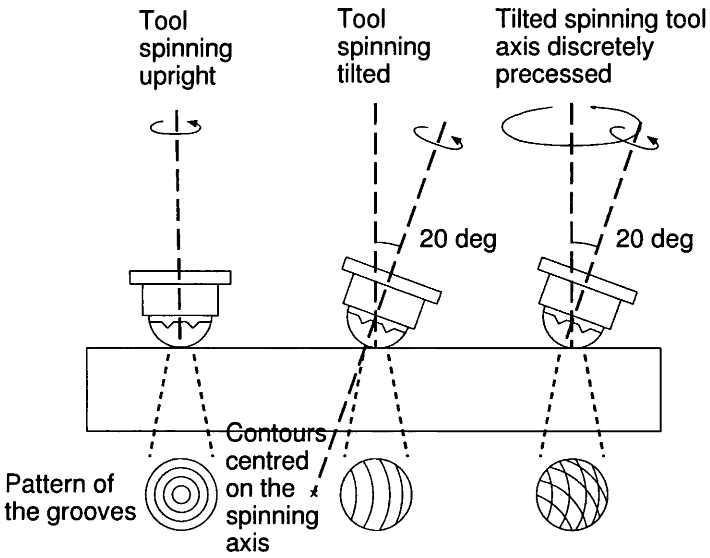

Figure 6.2: Effects of tilting and precessing a spinning compliant tool

under the tool.[52] Figure 6.2 illustrates the difference in the pattern of the way material is removed underneath the spinning tool. The upright spinning tool gives more variant (zero at the centre and maximum at the edge of the footprint) spinning speed on the contact area than the tilted spinning tool, hence the tilted spinning tool gives less variant material removal rate and more uniform material removal pattern underneath the tool.

The workpiece was kept horizontal in order to enable a pool of slurry to be contained to maintain constant slurry concentration. The slurry kept in the pool on the surface was continuously agitated to prevent precipitation by the tool spinning at 500 RPM, which conveniently prevented precipitation.

6.2.2 Tool and abrasive slurry

The hydraulic spinning compliant tool described in Chapter 4 was used for this experiment. The hydraulic spinning compliant tool was designed to give polishing pressures ranging from 21.4-40.8 kPa (3.1-5.9 psi) , by adjusting the spring inside the tool to pressurise the silicone oil. In order to see the two extreme cases, the two end pressures (highest and lowest) were used.

As for the abrasive slurry, Regipol 990 [87] was used. The concentration of the

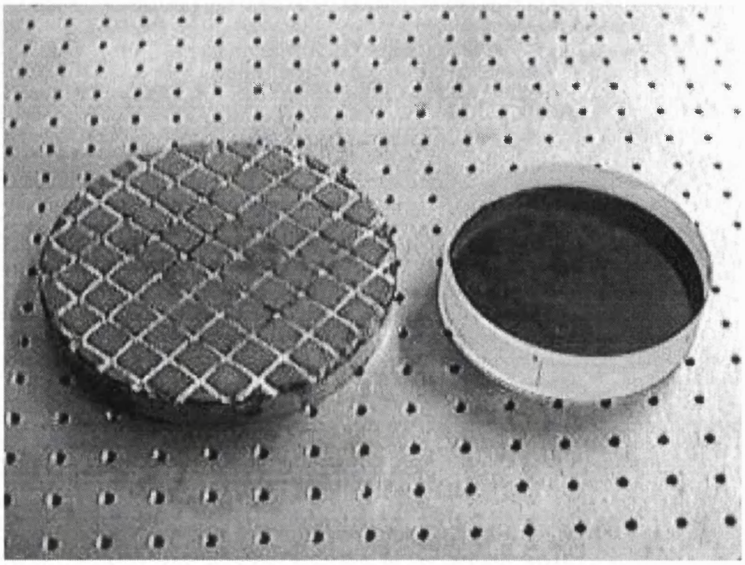

Figure 6.3: The oversized flat pitch tool used for planarisation, and the ∅140 mm workpiece

slurry [87] is 100 g/l. Regipol 990 is a peach coloured abrasive slurry, which has the average particle size in the region of 0.35-.0.45 μm according to the manufacturer.

6.2.3 Workpiece

A ∅140 mm BK7 sample was used as the workpiece. BK7 [98] is one of the most widely used material for optical components. The initial surfaces were prepared by the author, from a roughly ground sample. Both sides of the workpiece were hand-ground with a glass tool using 220, 400, 800, and 1000 grade carborundum, and finally hand-polished with a cerium oxide slurry (Regipol 788 and Regipol 990). An oversized pitch tool, as shown in Figure 6.3, was used for the polishing.

In order to measure the initial surface texture of the workpiece before the spinning compliant tool polishing runs, the R_a of 10 different locations are measured on the first planarised surface with a phase-shifting interferometer [114] as shown in Figure 6.4. The average of measured R_a values is 1.6 nm with the standard deviation of 0.17 nm.

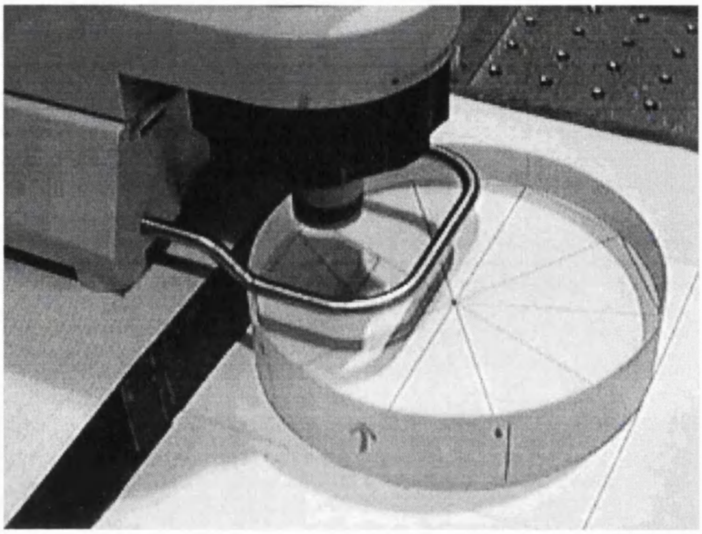

Figure 6.4: The surface texture measurement interferometer[114] and the workpiece

6.2.4 Surface texture measurement equipment

An interferometric surface texture testing apparatus, as shown in Figure 6.4 is used to measure the surface texture. For each measurement, cylindrical and tilt terms are removed to measure the higher frequency components only. Phase-Shifting Interferometry (PSI) mode is used which has resolution less than 1 Å.[114] For each polishing run, the surface texture is measured three times and averaged.

A 10× objectives is used with the interferometer, which gives 1.2 mm×0.9 mm inspection area, and 3.4 μm lateral resolution on the sample surface.

6.2.5 Effects of one-directional polishing on surface texture

Before investigating the effects of multi-directional polishing on surface texture, one-directional polishing runs were done on the flat workpiece, which were corresponding to the case of $\Delta\theta = 0°$ from the surface texture simulation in Figure 5.10.

The hydraulic spinning compliant tool was used to polish the workpiece without any lateral strokes or rotation of the workpiece, but only the spinning. Since there was no lateral strokes or precession of the tool, an arbitrary point on the contact area can be thought to experience effectively one-directional polishing. The tool was lowered so that the contact area had a diameter of 12 mm, which gave 40.8 kPa

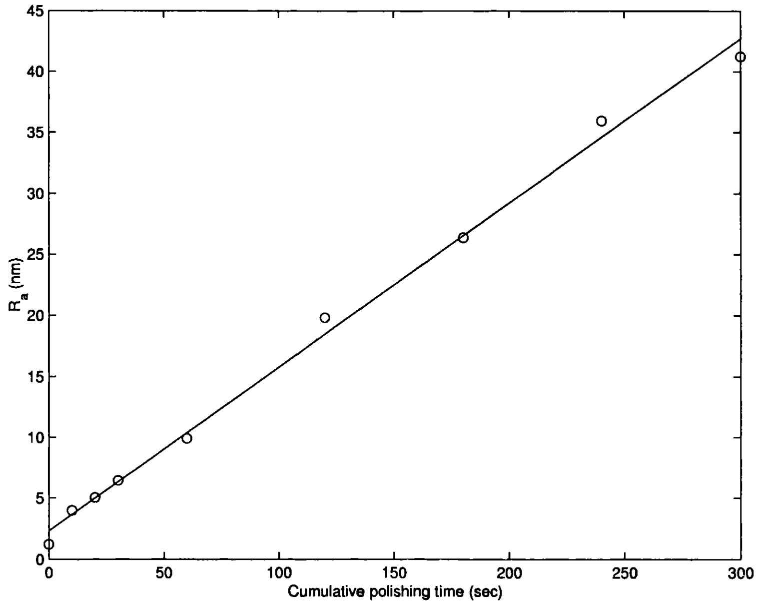

Figure 6.5: Surface texture measured against cumulative polishing time for one-directional polishing

(5.9 psi) of polishing pressure.

Figure 6.5 shows the surface texture R_a measured against the cumulative polishing time. It shows the surface texture became worse proportional to the polishing time. It instantly suggests that, unlike the hypothesis used in the last chapter as depicted in Figure 5.8, the removal profile polishing after the previous removal profile is more or less identical, and the valleys on the surface become deeper and the peaks are removed less to keep increase the R_a.

It can be interpreted that the elasticity of the polyurethane polishing cloth presses the abrasive particles deeper in the valleys of the workpiece surface when polished in the same direction. Therefore, it hints that the surface texture simulation, as a future work, should be extended to adopt the elastic nature of the spinning compliant tool surface, at least in order to be used when a spinning compliant tool is polishing in one-direction. Figure 6.8 shows the surface texture measurement result pictures, and the grooves are clearly visible. However, by looking at the size of the grooves, they can be recognised as the macroscopic grooves produced by the pores of the polishing cloth when the tool simply spins with no lateral strokes.

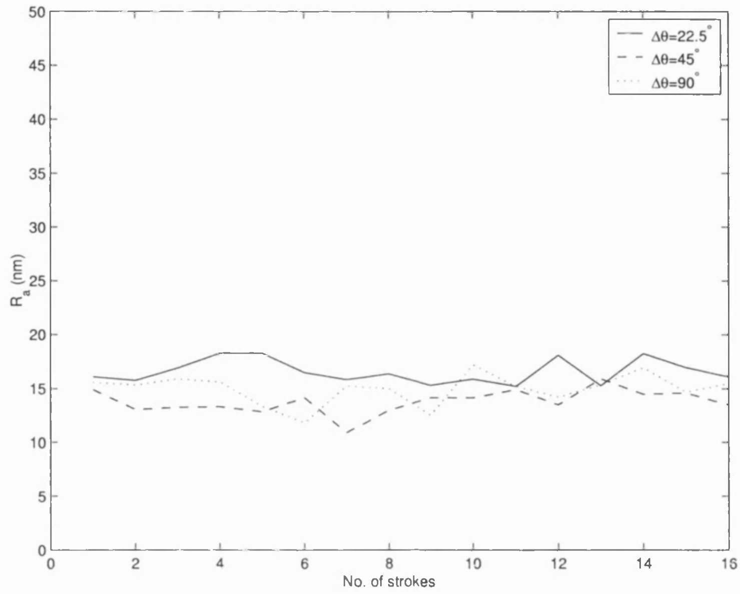

Figure 6.6: Surface texture result from discrete precession polishing experiment

6.2.6 Effects of discrete precession on surface texture

In order to see the effects of discrete precession of the spinning compliant tool, the workpiece was rotated after each 3-second session of polishing. Three angles ($\Delta\theta = 22.5, 45, 90°$) were used, as from the simulations of last chapter. The internal pressure of the hydraulic spinning compliant tool was reduced, so that it gave 21.4 kPa (3.1 psi) polishing pressure in order to reduce the macroscopic grooves caused by the polishing cloth structure.

The measured surface texture values are plotted in Figure 6.6. It shows the surface texture values do not increase as in the one-directional case but remain more uniform within ±2 nm. It shows the regime where the surface textures reach the lower limit as simulated in Figure 5.11. It also shows that the angle difference $\Delta\theta$ does not play a significant role on surface texture in discrete precession polishing, which also seems to agree with the simulation in Figure 5.11. It hints that when a tool surface is elastic, the peaks-first removal scheme used in the surface texture simulation can be used for multi-directional polishing, unlike the case of one-directional polishing.

Note however that these results were obtained with the no lateral tool motion on the surface, and hence the averaging mechanism of real polishing was absent. This explains the moderately high absolute values of R_a.

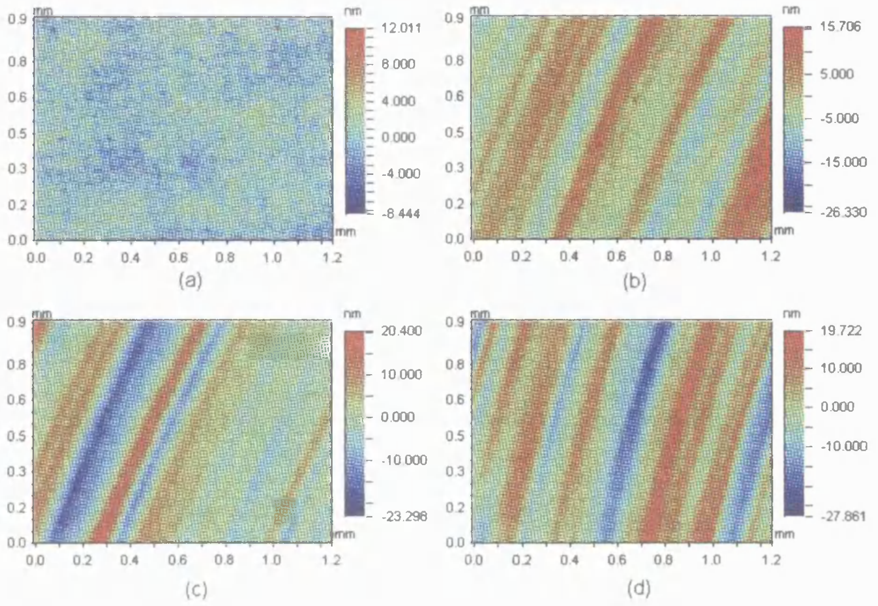

Figure 6.8: Surface texture measurements of one-directional polishing

compliant tool was polishing. Due to the limit of the drill polishing set-up, which did not have a turn-table for the workpiece, the workpiece was rotated nearly continuously by hands with approximately 4 RPM. The polishing session lasted 30 seconds. It produced R_a of 12.7 nm, which was smaller than most of surface textures produced by discrete precession polishing. The measurement resulted from the surface texture interferometer are shown in Figure 6.8, 6.9, and 6.10.

Figure 6.8 shows the surface texture measurements of one-directional polishing from the initial surface to next polished surfaces differ by 10 seconds of polishing time. The groove patterns produced by the pores of the polishing cloth are clearly shown.

Figure 6.9 shows the surface texture measurement of discrete precession polishing when the polishing pressure was high (40.8 kPa) and the discrete precession angle $\Delta\theta = 22.5°$. The clockwise rotation of the pattern can be seen. Although each polishing session lasted only for 3 seconds, each picture of Figure 6.9 shows that the grooves from the previous session are virtually over-written with the current ones. It explains why the surface texture was almost the same for different discrete precession angle $\Delta\theta$, and why it is more efficient to precess the tool continuously.

Figure 6.10 is the surface texture measurement picture when the workpiece was manually rotated nearly continuously. It shows less directional pattern with smaller

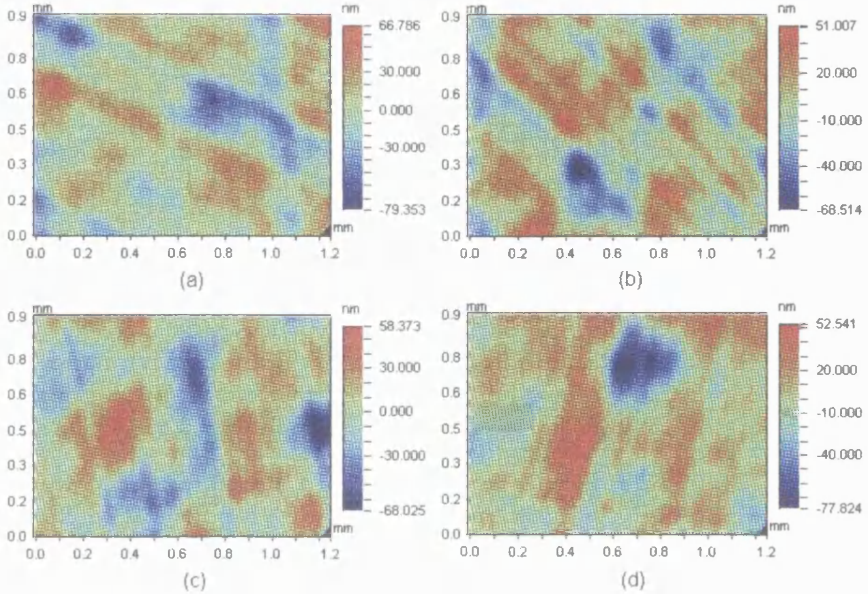

(a) (b)

(c) (d)

Figure 6.9: Surface texture measurements of discrete precession polishing

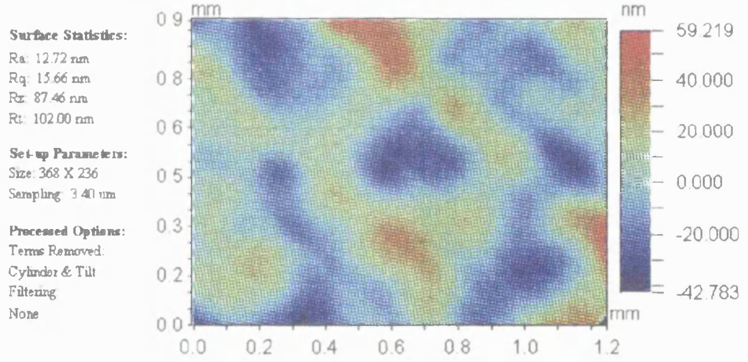

Surface Statistics:
Ra: 12.72 nm
Rq: 15.66 nm
Rz: 87.46 nm
Rt: 102.00 nm

Set-up Parameters:
Size: 368 X 236
Sampling: 3.40 um

Processed Options:
Terms Removed:
Cylinder & Tilt
Filtering
None

Figure 6.10: Surface texture measurements of continuous precession polishing

surface texture. The tool pressure used was low (21.4 kPa) and the rate of rotation of the workpiece was approximately 4 RPM. When the tool is continuously precessed, the dwell-time of one-direction can be smaller than the case of discrete precessesion.

6.3 Surface texture by SCT on CCPM

Multi-directional polishing can be implemented in another way: giving lateral strokes when polishing. In this section, multi-directional polishing is described with a spinning compliant tool on the CCPM used in Chapter 3, by giving lateral strokes,

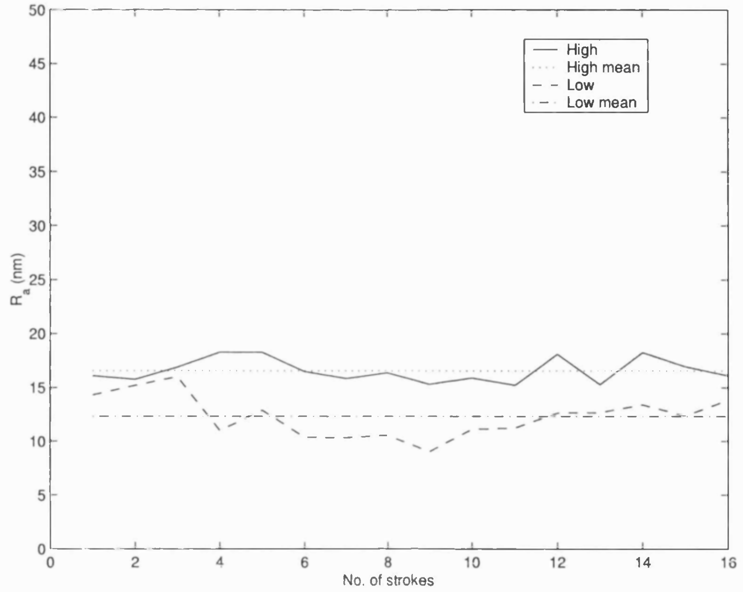

Figure 6.7: Effects of tool pressure on surface texture

6.2.7 Effects of SCT pressure on surface texture

From Equation 5.5, it was also speculated that the total load of the polishing tool, or the polishing pressure on a contact area, contributed to the gap between the workpiece and the tool. The smaller the pressure, the larger the gap becomes, and from Equation 5.11, the groove depths become smaller, thus surface texture becomes better.

Surface textures produced by using two different internal pressures of the hydraulic spinning tool are compared, in order to see the effect of different polishing pressures on surface texture. The high pressure was 40.8 kPa, and the low was 21.4 kPa.

Figure 6.7 shows the surface texture values of discrete precession polishing of two different polishing pressures. The discrete precession angle $\Delta\theta$ was 22.5° for both pressures. It shows that by reducing the polishing pressure down to half, the average surface texture was decreased by 25%.

6.2.8 Surface texture comparison

After the discrete precession polishing experiment was carried out, continuous precession polishing was experimented by rotating the workpiece while the spinning

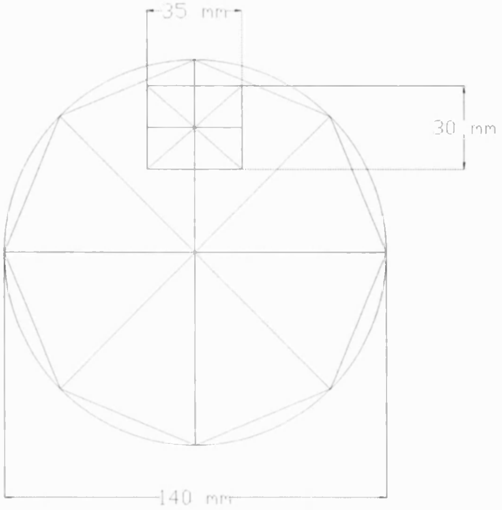

Figure 6.11: ∅140 mm BK7 workpiece with one of eight 30 × 35 mm^2 polishing areas shown

instead of precessing of the tool. In conventional polishing, W-shaped strokes are given to apply multi-directional polishing to reduce surface texture. By using the programmable stroke capability of the CCPM, W-shaped strokes were given with a spinning compliant tool. With the W-shaped strokes on, the effects of tool spinning RPM on the surface texture is investigated. The tool RPM was chosen since it is related to the relative speed between the tool and workpiece, which was used as a parameter in the pitch tool polishing experiment in Chapter 3.

6.3.1 Workpiece

Another ∅140 mm BK7 workpiece was used again for this experiment. The initial surfaces were prepared by hand polishing as before. In order to use the workpiece surface efficiently, sectored zones were allocated as shown in Figure 6.11, and each octant sector was polished with different tool RPM. Each sector was polished for 30 seconds with the assigned tool RPM, with the strokes confined in the 30 × 35 mm^2 rectangle so the tool was always inside a fixed area of the sector. The surface texture was measured three times around the centre of the rectangle and averaged. Six polishing runs with different tool RPMs were made on each side of the workpiece, leaving two for contingency.

In measuring the surface texture itself before and after the spinning compliant tool polishing, the initial surface form does not have to be of high quality. However, in order to measure the surface form before and after polishing, thus the material removal rate, it is beneficial to have a relatively optically flat form, which will be discussed in the next chapter. Due to the limits of the surface form measurement equipment, the flatter the initial surface is, the less error in measuring the amount of the removed material.

Each initial surface is hand polished with a pitch tool to have $1/4 \pm 1/10\ \lambda$ peak-to-valley flatness in the polishing region.

6.3.2 Abrasive slurry

Cerox 1670 was used as abrasive slurry for the experiment with concentration of 100 g/l. It is creamy white coloured, and has 1-2μ of the average particle size.[94] When used with a pitch tool, it is known to have slower removal rate but finer surface texture than Regipol 788[12], which was used in the pitch tool polishing experiment in Chapter 3.

For this section, the slurry pool could not be used due to the size of the polishing head, giving lateral strokes. Instead, the abrasive slurry was supplied with a squeezy bottle to the workpiece to make the polishing area continuously wet throughout the run. At faster tool rotation beyond 400 RPM, the slurry is rapidly spattered and it has to be supplied 3-4 times to make the polishing area wet.

6.3.3 Tools and RPM

Driver electronics for the spinning compliant tool were built as shown in Figure 4.9, and used to control the RPM of the spinning tool reported in this chapter.

Since the hydraulic spinning compliant tool used with the pillar drill set-up did not have mechanical interface to be used with the CCPM in this experiment, a single pressure spinning compliant tool from Chapter 4 was used. The squash ball tool had the polishing pressure of 68.9 kPa (10 psi).

Six different spinning RPMs were chosen: 100, 200, 400, 600, 800, and 1000 RPM.

These were chosen based on a similar experiment which had been carried out at OGL in the past.[56] It had been reported that a tool RPM around 100 RPM had given the best R_a of 8 nm under a certain set of experimental conditions.

Compared to the pressure and speed values used in the pitch polishing experiment (60-120 kPa, 25-100 mm/sec), relatively lower pressure (68.9 kPa) and higher speed (the maximum tangential speed when the contact area had 10 cm diameter was approximately 1340 mm/sec when the tilted tool was spinning at 1000 RPM) were used in the surface texture experiment with spinning compliant tools. (See Appendix B for the velocity component calculation.)

6.3.4 CCPM

The CCPM head was tilted 20 degrees as shown in Figure 6.13 as with the drill machine experiment, in order to reduce undesirable gradient effects concentric grooves of a rapidly spinning tool as shown in Figure 6.2.

In a past experiment using a rotating tool with the polishing head in the up-right position, it was reported that the tool mark on the workpiece had concentric rings under the tool.[52] Figure 6.2 illustrates the difference in the pattern of the way material is removed underneath the spinning tool. The upright spinning tool has more speed variation (zero speed at the centre and maximum at the edge of the footprint) across the footprint than the tilted spinning tool. Hence the tilted spinning tool gives less variation in material removal rate and more even material removal pattern underneath the tool.

Litton Itek [49] had attempted a tool *orbiting* around an axis without any spinning of the tool itself to avoid the concentric material removal problem. The difference between a tool orbiting and spinning (with the axis upright) is illustrated in Figure 6.12.

However, due to the complexity of the orbiting mechanism (up to 400 RPM) and the characteristics of the pitch tool used in the Litton Itek's CCOS, the OSL's spinning compliant tool approach (up to 1000 RPM) can offer higher spinning RPM, thus a higher material removal rate.

The prototype CCPM was used under the "height equation mode" in which the

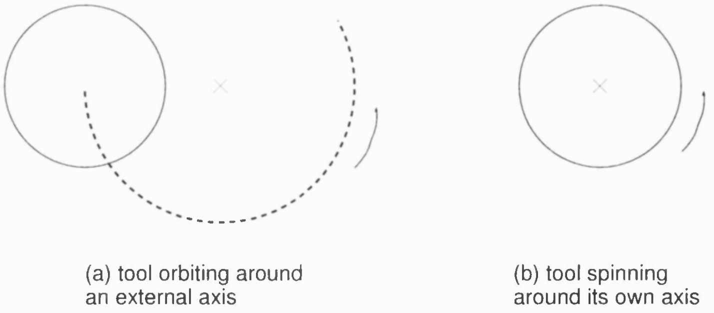
(a) tool orbiting around an external axis

(b) tool spinning around its own axis

Figure 6.12: Comparison of motions of (a)oribiting tool and (b)spinning tool viewed from top

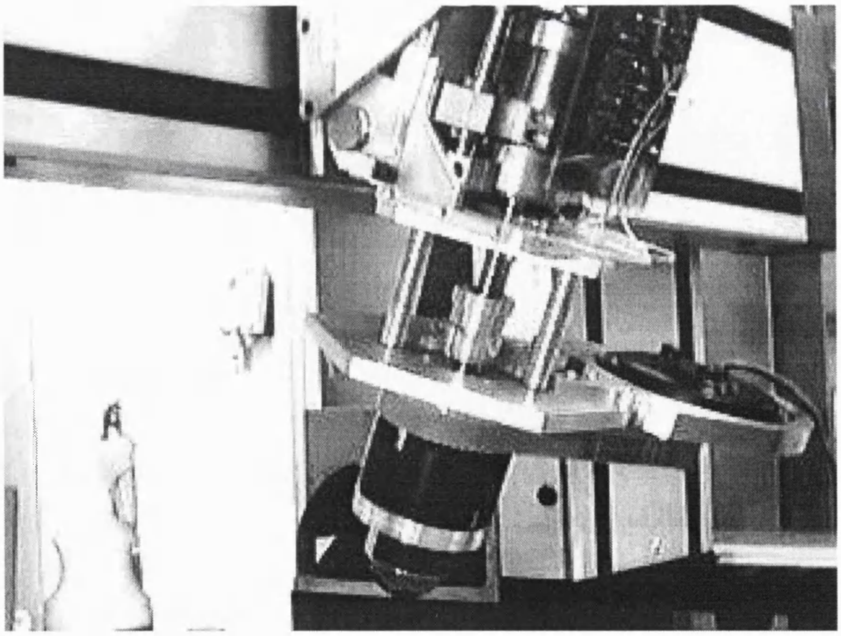

Figure 6.13: CCPM head with the spinning compliant tool attached

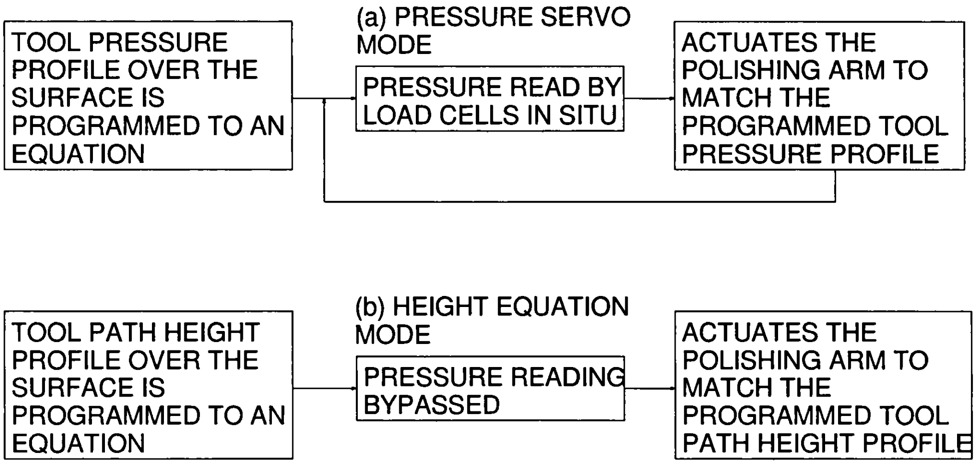

Figure 6.14: Comparison of pressure servo mode (a) and height equation mode (b) of the CCPM

height of the tool (Z arm height) can be pre-set by a polynomial equation, regardless of the forces recorded by load cells of the polishing head. A constant height ($Z = c_0$) was used for the equation as the experiment was carried out on a flat surface.

The active pressure servo mode, which was used for the pitch tool experiment in Chapter 3 could not be used with the compliant tools due to the following reasons. (The difference between the pressure servo mode and the height equation mode of the CCPM is briefed in Figure 6.14.)

The prototype CCPM used was originally designed for hand tools such as pitch. Its frequency response in pressure-servo mode, combined with the resonant frequencies of the compliant tool and machine, led to a dynamically unstable system which oscillated. It was also due to the load cell housing mechanism of the CCPM which was designed for vertical operation, so that pressure could not be measured accurately when the polishing head was tilted as in this experiment.

The strokes were set so that each tool contact area was polishing in a fixed rectangular area as shown in Figure 6.11. The turntable was not rotated while polishing stroke direction and was rotated 45° after one polishing run for the next sector.

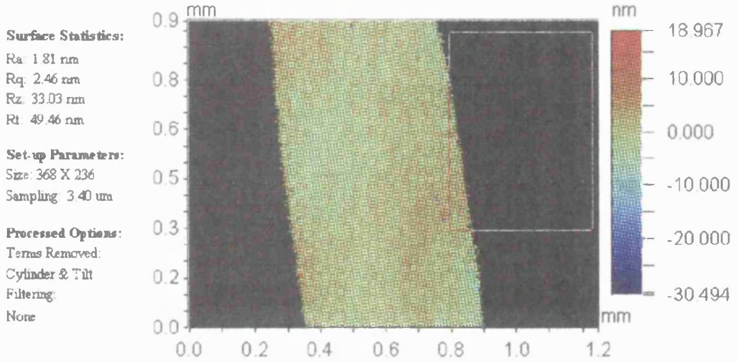

Surface Statistics:
Ra: 1.81 nm
Rq: 2.46 nm
Rz: 33.03 nm
Rt: 49.46 nm

Set-up Parameters:
Size: 368 X 236
Sampling: 3.40 um

Processed Options:
Terms Removed:
Cylinder & Tilt
Filtering:
None

Figure 6.15: Interferometric surface texture measurement of a sample glass *without* tip-tilt stage (white rectangle in the upper right corner to be magnified in Figure 6.18)

6.3.5 Discussion on surface measurement

The same surface texture measurement interferometer was used to measure the surfaces in this section. Figure 6.15 shows a surface texture measurement result for the experiment in this section. However, it shows that the whole inspection area could not be measured. Usually, a sample is put on the tip-tilt micrometer stage of the interferometer, in order to capture the interferometric fringes over the whole inspection area. Since the workpiece was too thick to be placed between the objectives and the tip-tilt stage of the interferometer, the workpiece was placed on the optical table, and the fringes could not be focused over the whole inspection area. Approximately 1/3 of the whole inspection area could be focused and measured as shown in Figure 6.15. Black area is where it was not within the depth of focus of the instrument.

To see the effect of the reduced inspection area, a different glass sample, which is thin enough to be used with the tip-tilt stage, was separately measured. To simulate the situation without the tip-tilt stage, several sub-regions with approximately 1/3 of the whole area were selected and measured. The 1/3-area sub-region measurements showed a tendency of smaller R_a values, with less than 10% difference at maximum from that of the whole area. Therefore, it was concluded that the measurements with one third of the inspection area, (without tip-tilt stage) can be accepted as the valid surface texture measurements to 10%. A comparison is illustrated in Figures 6.16 and 6.17, in which Figure 6.17 is a subset from Figure 6.16 as indicated by a

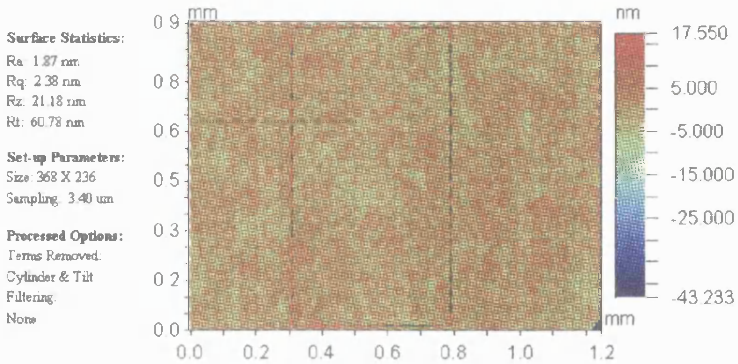

Surface Statistics:
Ra: 1.87 nm
Rq: 2.38 nm
Rz: 21.18 nm
Rt: 60.78 nm

Set-up Parameters:
Size: 368 X 236
Sampling: 3.40 um

Processed Options:
Terms Removed:
Cylinder & Tilt
Filtering:
None

Figure 6.16: R_a measured over the whole inspection area of a test sample glass *with* the tip-tilt stage (A sub-region is shown in a vertical rectangle in the middle.)

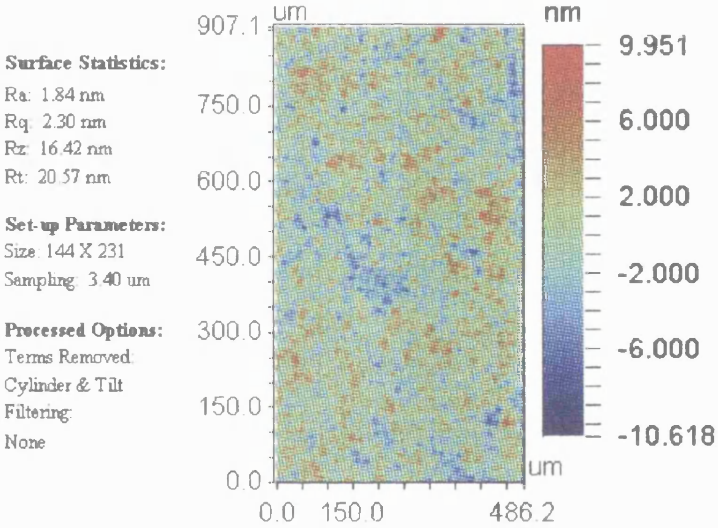

Surface Statistics:
Ra: 1.84 nm
Rq: 2.30 nm
Rz: 16.42 nm
Rt: 20.57 nm

Set-up Parameters:
Size: 144 X 231
Sampling: 3.40 um

Processed Options:
Terms Removed:
Cylinder & Tilt
Filtering:
None

Figure 6.17: R_a measured over the sub-region surface of the test sample glass in Figure 6.16

rectangle in Figure 6.16. The whole inspection area gives R_a=1.87 nm while the sub-region gives R_a=1.85 nm, which is about 1 % difference in R_a values.

It was also checked that the blank regions (see Figure 6.15) did not contribute to the calculation of R_a. In the Figure 6.15, a sub-region is chosen as a rectangle containing small area of the measurement area, but the blank area as the majority. In the sub-region, if the blank region were counted as zeros for the calculation of R_a, then the R_a for the sub-region would be substantially smaller than the R_a from the Figure 6.15, as the majority of the sub-region are zeros. However, it is confirmed that a blank region is not counted as zero but ignored, as the R_a shown in Figure

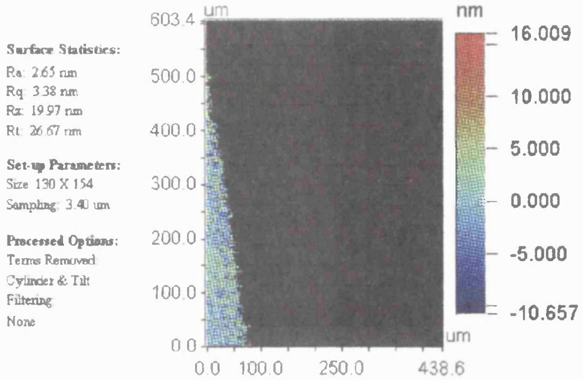

Figure 6.18: R_a measured in the sub-region of the sample glass surface measurement containing blanks (magnified from Figure 6.18)

6.18 of the sub-region, which gives R_a=2.70 nm, even higher than the R_a from the mother region in Figure 6.15. This also ensures that the surface texture of a reduced inspection area (i.e. without the tip-tilt stage) can be trusted.

The same test sample was also measured with different magnification objectives - providing different inspection area dimensions but the same number (368×236 pixels) of spatial sampling, thus different spatial sampling rates 2.5×, 10×, and 40× objectives are tested. They respectively gave the spatial sampling resolution, or the distances between the centres of two adjacent pixels on the test surface, of 13.60 μm, 3.40 μm, and 850.00 nm.

The R_a measurements gave 1.69 nm, 1.87 nm, and 2.79 nm respectively, thus larger R_a for higher magnification objectives.

Usually little attention is paid to the importance of the sampling resolution and inspection area or length (in the case of line-scanning stylus profilometers) when measuring surface texture. However, R_a needs to be given with measurement details such as the inspection area and sampling resolution, as R_a can have different values with different sampling resolution and inspection area on the same surface. Furthermore, any filtering of the measurement should be given as well as this can change the surface texture result.

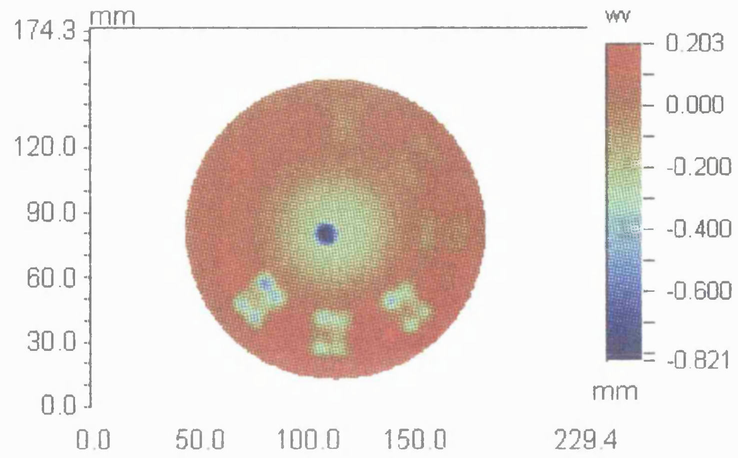

Figure 6.19: Stroke patterns measured with surface form interferometer[112] for tilted spinning compliant tool polishing(68.9 kPa, 100, 200, 400, 600, 800, 1000 RPM, Cerox 1670)

6.3.6 Effects of spinning tool RPM on surface texture

Figure 6.19 shows the pattern of removal, which was measured after 6 polishing sessions. WYKO 6000 optical surface form interferometer was used, whose accuracy (peak-to-valley) of the instrument is known to be better than 6 nm with a repeatability surpassing 0.6 nm.[112]

Different tool spinning RPM was used for each octant. Due to the nature of the W-stroke, the speed of stroke becomes zero momentarily to reverse the stroke at the edge of the pre-defined polishing rectangle. Most noticeably, 4 corners have deepest removal where both x and y directional stroke speeds become zero momentarily, while the compliant tool is spinning. (The central dip was produced when no-stroke polishing was done to measure the size of the contact area.)

For each octant, R_a at the centre of the pre-defined polishing rectangle was measured. The measured R_a values against the tool RPM are plotted in Figure 6.20. After doing one set (6 RPMs) of experiments, two more identical sets were carried out for repeatability test. Three measurements are averaged for each tool pressure-RPM combination and the error bar shows the range of three measurements for each point. The averaged surface texture values were in between 2.0 and 2.6 nm.

The results show that there is an insignificant relationship between R_a values and

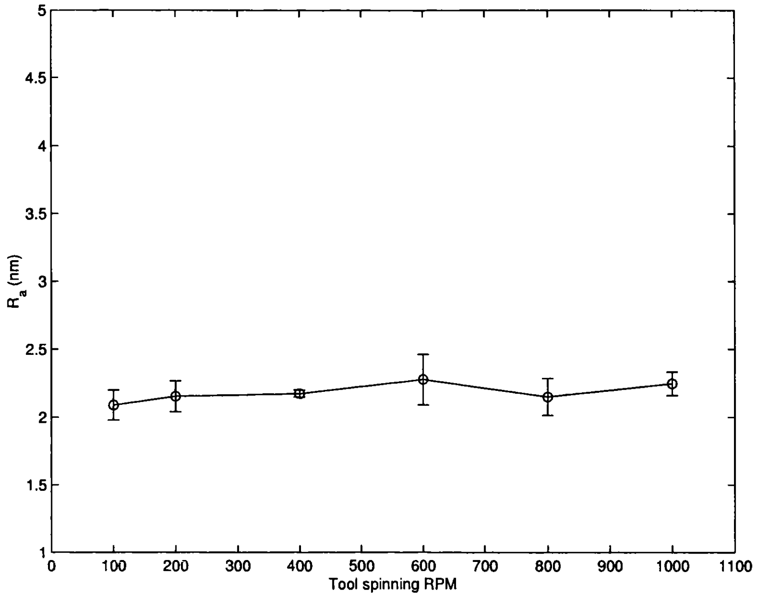

Figure 6.20: Surface texture against RPM for spinning compliant tool polishing(68.9 kPa, 100, 200, 400, 600, 800, 1000 RPM, Cerox 1670)

the tool RPM nor with the pressure, within the ranges of RPM used and the specific experimental set-up. Although the trends show that R_a slightly increases as RPM increases, the slopes of change are negligible in practical polishing a few Åof differences in R_a. The total average of the surface textures is R_a=2.2 nm which is significantly better than the surface texture achieved by any of the previous results by a spinning compliant tool at a single location on the sample, discretely or continuously precessing. This is consistent with the lateral stroke averaging the surface texture generated by the tool surface.

The result also shows that near pitch tool polishing surface quality ($R_a = 1$ nm) can be achieved by giving W-shaped strokes with no precessing of the tool. Intuitively, the combination of lateral stroke and precession would be expected to give the best surface texture. However, the experimental equipment required to confirm this was unavailable to the author.

Furthermore, different tool spinning RPM can in principle be used as required for a figuring process - higher removal rate for higher RPM - without the loss of surface quality with the given polishing pressure. However, it should be noted that changing the tool spinning rate still disturb the tool influence function, which would need to be considered when developing the form control algorithm.

6.4 Conclusion and future work

Various situations with the spinning compliant tool were experimented in this chapter, and the surface texture values were measured against different factors. The limit-reaching feature described by the surface texture model from the last chapter as shown in Figure 5.10 was supported by the observations. The effects of discrete polishing on surface texture was also observed as simulated in Figure 5.11. It also confirmed that the final limits of surface texture are not affected by the precession angle $\Delta\theta$ for discrete precession polishing.

It was observed how continuous precession produces better surface texture than discrete precession of the tool, and it was also observed that lateral strokes produce near pitch tool polishing quality. The future work on combining the continuous precession and lateral stroke remains to be investigated with anticipation of the lowest achievable surface texture by this type of polishing tool.

Also the role of polishing pressure on surface texture was observed, which suggests controlling of the internal pressure of the hydraulic polishing tool in real time so that the polishing pressure can be reduced over time, can be useful to improve the surface texture. This would require independent control of the pressure within the tool, as well as the force with which it is applied to the workpiece.

However, the porous structure of the polishing cloth also degrades the surface texture by producing macroscopic grooves, whilst this is both by stroke and precession, there is clearly scope for further investigation on different kinds of polishing cloths. Particularly, development of a “compliant bound-abrasive”, which can conform to the compliant material of the SCT, would be beneficial to the SCT polishing for aspheric optics.

Having demonstrated that the surface texture with the SCT polishing can achieve near surface texture of pitch tool polishing, the material removal characteristic in terms of form is investigated in the next chapter.

Chapter 7

Surface form figuring with spinning compliant tool polishing

7.1 Introduction

Surface texture, the microscopic aspect of polishing aspheric optics with spinning compliant tool, was discussed in the previous two chapters. The other aspect of material removal on an aspheric surface is to achieve a target design in terms of the macroscopic surface *form*, within a tolerance. It is the aspheric *form* that makes it difficult to polish/figure with conventional pitch tools, due to the changing radius of curvature on the surface, and even more difficult to test in optical quality. In order to solve the former of the problems, a method which can be used to polish/figure an aspheric surface is developed in this chapter by using a spinning compliant tool.

In chapter 3, the material removal rate in pitch tool polishing was investigated at a location on the workpiece. However, in order to produce an optical "surface," it needs to be extended over an area. In this chapter, a preliminary investigation of a process to polish/figure over an axially symmetric aspheric surface, using the spinning compliant tool is reported. A trial surface form figuring experiment based on this method demonstrates feasibility of the approach.

Firstly, using the fixed-pressure spinning compliant tool from the previous chapter, the influence function, which is defined as the material removal rate of the spinning compliant tool, is measured. This characteristic function of a spinning compliant tool is dependent on spinning RPM and pressure. This function was measured with the surface form interferometer [112].

Secondly, polishing simulation software SimPol is developed, which incorporates the tilted spinning velocity calculation and the distributed polishing pressure investigated in chapter 4. It is used to predict the material removal with the spinning compliant tool polishing, and this work leads to an algorithm for dwell time calculation.

Finally, an algorithm to calculate the dwell time of a spinning compliant tool, to polish axially symmetric aspheres is developed, and used to predict the material removal. Then, the dwell time calculation is applied to a preliminary surface form experiment to polish an arbitrary axially-symmetric aspheric form.

7.2 Influence function for spinning compliant tool

Unlike a pitch tool, a spinning compliant tool can remove material when there is no lateral strokes, due to the rapid spinning. When the polishing pressure and the spinning RPM are defined at a fixed location with a specific glass and with a specified abrasive slurry, the volumetric material removal rate of the spinning compliant tool can be obtained by measuring the volume of removed material and the polishing time. Since this removal rate is characteristic function of the spinning compliant tool, it is henceforth called the *influence function* of the spinning compliant tool.

Polishing of a surface using a spinning compliant tool is essentially a convolution of this influence function on the workpiece surface over a total polishing time, and it is important to know the shape of influence function of a spinning compliant tool under certain parameters in order to predict the surface form.

Again, the squash ball tool, which has the characteristic polishing pressure of 68.9 kPa, was chosen for this chapter. Figure 7.1 shows a view of the spinning compliant tool mounted on the CCPM, with 20° of tilt from the vertical, ready to polish on a workpiece with abrasive slurry.

For the measurement of the influence function, the spinning compliant tool was pressed on the centre of the same ⌀140 mm BK7 workpiece used in the CCPM

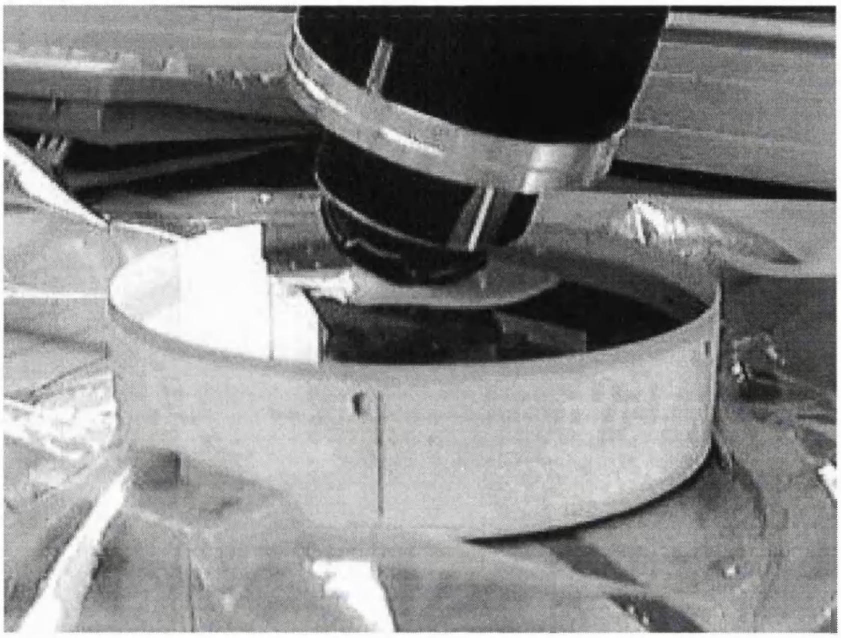

Figure 7.1: Tilted spinning compliant tool (68.9 kPa) in contact with the abrasive slurry (Regipol 788) on the workpiece

polishing experiment from the last chapter, spinning with 100 RPM. Giving no side-way strokes, it was pressed for 30 seconds, and Figure 6.19 shows the removed pattern as a hole in the centre of the picture. A magnified contact area is shown in Figure 7.2. It hints at the slightly arc-shaped groove pattern, which is caused by the tilted spinning of the tool. Figure 7.3 shows the 3D view of the influence function, which is slightly tilted to one side as it is caused by a tilted spinning tool. It can be seen that the deepest point is approximately 0.4 μm below the surface, thus giving 0.8 μm/min in terms of depth removal rate. As a comparison, the typical values of the depth removal rate from the pitch tool polishing (see Chapter 3) were less than 0.2 μm/min.

7.3 Simulation of surface form polishing

Microscopic surface texture under certain conditions is simulated in Chapter 5, which was based on a statistical model. Macroscopic surface form can be simulated by using Preston's equation. In order to predict the surface form of the polished surface, a polishing simulator named SimPol was written in MATLAB and described in this

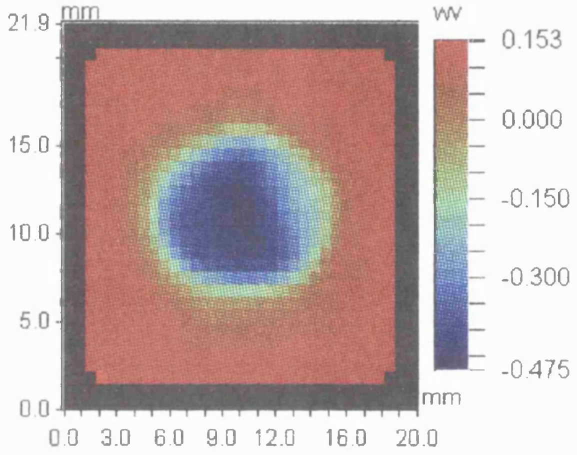

Figure 7.2: Contact area of the influence function polished by the tilted spinning compliant tool (68.9 kPa, 100 RPM) for 30 sec

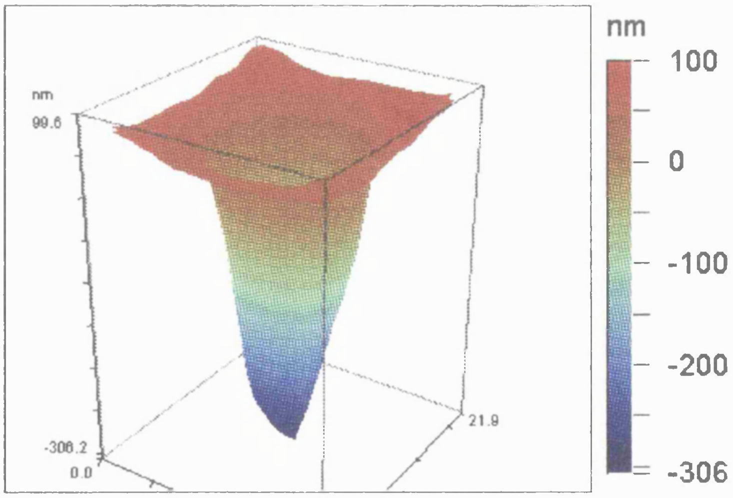

Figure 7.3: 3D view of the influence functions of the tilted spinning compliant tool

chapter. The prototype CCPM uses a software called DIPOS (Dedicated Intelligent Polishing Operating Software), which predicts the material removal by combining the polishing parameters in real time. Since the version used (ver. 5.0) of DIPOS was originally developed for the pitch tool polishing, it supports neither the arc-shaped speed map (e.g. Figure 4.11 (b)) with a tilted spinning tool, nor the distributed pressure (e.g. Figure 4.16) underneath a compliant tool.

SimPol was developed to incorporate the tool speed profile across a tilted spinning tool, as well as the distributed polishing pressure underneath the compliant tool. Unlike DIPOS 5.0, SimPol runs completely as a stand-alone simulation - without any data transfer from the running CCPM. It means a prediction can be made without actually running the CCPM.

Figure 7.4 shows screen shots of SimPol for a polishing example, chronologically in alphabetic order. The same polishing parameters for the polishing experiment from the last chapter with the 68.9 kPa squash ball were used - tool size, RPM, tilt angle, and side-way stroke lengths and frenquencies. Although the material removal coefficient is arbitrarily put as 1, the material removal pattern agrees well with that of the measurement shown in Figure 6.19.

The speed map of the tilted spinning compliant tool as in Figure 4.11 (b) and the pressure distribution showed in Figure 4.16 are used. The tool was rotated with 400 RPM, the rotation axis was tilted 20 degrees from the vertical axis. Without any turntable rotation, the 30 mm$\times$35 mm strokes are given with 0.31 Hz and 0.13 Hz stroke frequencies for x and y strokes respectively. The diameter of the tool contact area is 14 mm while the workpiece diameter is 140 mm.

Within the pre-defined rectangular polishing area, the stroke in each direction accelerates in the first half stroke and decelerates in the latter half stroke, so the speed of the stroke is maximum in the middle of the stroke, and zero at both ends of the stroke. Consequently, it shows that the corners of the polishing area have higher material removal than that in the middle. Due to the rapidly spinning tool, it removes more materials when the dwell time is longer, and the effect is maximised when x and y strokes coincide with zero speeds at the four corners of the polishing area. The distinctive four peaks can be seen in the figure, which is the material removal result after 30 seconds of polishing from the start.

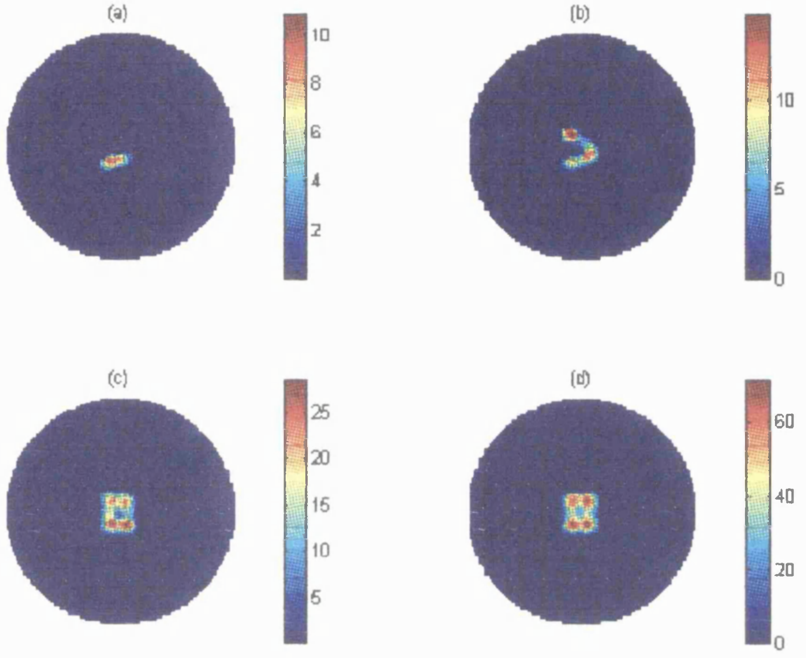

Figure 7.4: Screen shots of the SimPol simulating the polishing pattern of Figure 6.19

7.4 Unit material removal using SimPol

The form figuring work for a spinning compliant tool in this chapter starts with no precession, and no lateral random strokes. Taking advantage of an axially symmetric surface as the target surface as the starting point, no lateral random strokes were given but only the tool spinning and the turntable rotation were used in this chapter.

An annular groove is polished on the surface at a distance between the tool and the centre of the workpiece, as shown with a pitch tool in Chapter 4. The idea was to increase the radial distance by 1 mm and give different dwell time at each position according to a dwell time calculation. With a constant turntable RPM and a tool spinning RPM, the spinning compliant tool dwell time was the only variable to control the form. The schematic view of the spinning compliant tool polishing is shown in Figure 7.5, and an example of predicted material removal as an annular groove by a spinning compliant tool is shown in Figure 7.6. In the latter figure, the workpiece surface is a reference, and it is shown as if the workpiece were stationary

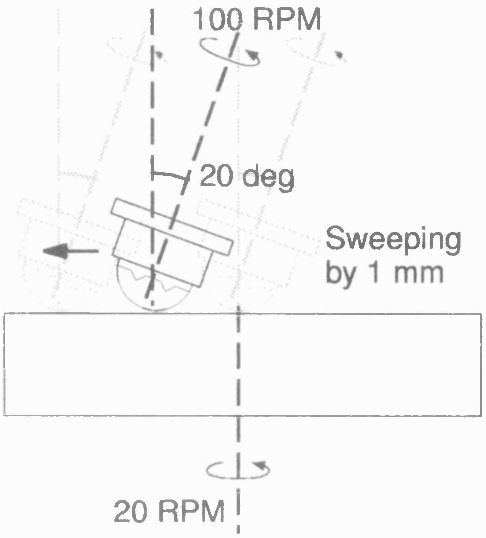

Figure 7.5: Discrete radial sweep of the spinning compliant tool: from the centre to the edge of the workpiece

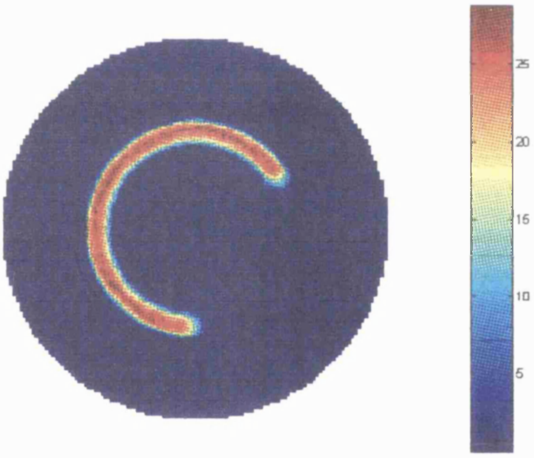

Figure 7.6: Screen shot of SimPol showing the real-time formation of an annular groove: spinning compliant tool polishing clockwise

and the tool is rotating.

The 140 mm BK7 workpiece used in the last chapter was hand-polished with a pitch tool with Regipol 788 to have an arbitrary but rotationally symmetric convex form. The central circular area with 50 mm diameter was chosen as the initial surface. The radial profile of the initial surface, was measured by the WYKO 6000 surface form

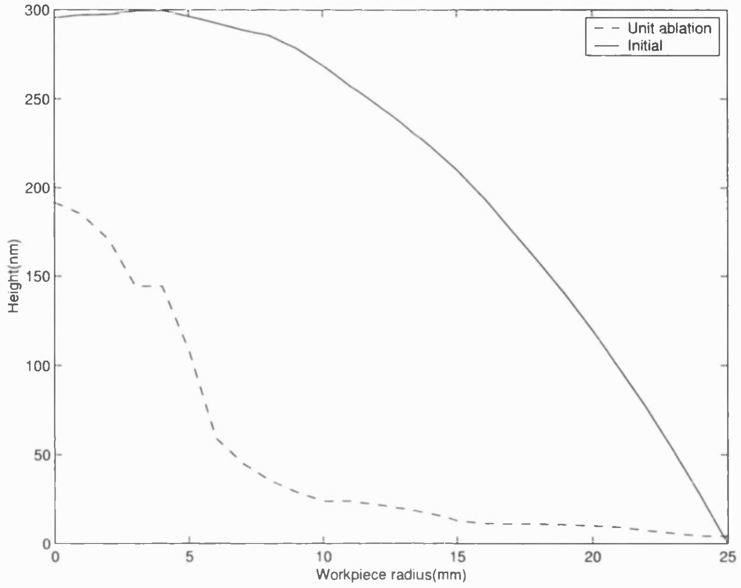

Figure 7.7: Initial error (solid) profile and the unit material removal (dashed) calculated by SimPol

measurement instrument, and is shown as the solid profile in Figure 7.7. The target was to polish the initial surface to a flat surface, thus the solid profile in Figure 7.7 was also the initial error to be polished. The initial peak-to-valley error was 0.3 μm (=0.48λ, λ=632.8 nm).

Since the workpiece was symmetric, the polishing was planned to be carried out by sweeping the spinning compliant tool along the radius of the workpiece, from the workpiece centre outwards by 25 mm .

The unit material removal is defined as the convolution of the annular grooves, by radially increasing the tool position from the workpiece centre to the 25 mm edge by 1 mm. Each annular groove is polished for one period of the turntable rotation. For example, when the turntable RPM is 20, the turntable period is 3 seconds, then each annular groove is produced for 3 seconds at each radial position.

The material removal function measured in Figure 7.3 was used to find out the material removal coefficient in Preston's equation. By matching the height of the influence function in SimPol with that of the profile of the measured influence function, the material removal coefficient for SimPol was determined as 0.26×10^{-6} mm^2/N.

For the SimPol calculation, 100 RPM was used for the spinning tool, and 20 RPM was used for the turntable, giving three seconds for the rotation period. By running SimPol with the tool position being stepped radially outward in 1 mm steps on the workpiece every 3 seconds, the predicted unit material removal was calculated, shown as the dashed profile in Figure 7.7.

It was initially thought that by dividing the initial error profile by the unit material removal profile, then multiplying by the period of the turntable, would give the required integrated dwell time at each tool position.

However, the shortcomings of the scheme was realised soon after the unit material removal profile was compared to the initial error profile. Figure 7.7 shows the peak of the unit material removal profile near the centre of the workpiece caused by starting the scanning such that the centre of the tool is starting from the centre of the workpiece. This implies polishing near the centre of the workpiece can easily be over-polished. It should therefore be polished carefully, especially inside the workpiece radius equal to the radius of the contact area.

More seriously, the convolution effect of the contact area is considered only for the calculation of the unit material removal. However, it is not sufficient to convolve to the initial error profile, which is not intuitively seen.

For example, consider two adjacent tool positions A and B on the radius of the workpiece. The unit material removal values are calculated by SimPol. Since the polishing by the tool at position A overlaps the surface at position B due to the area of the tool area. The polishing at the two positions are not independent. Simply obtaining the multiples of the unit material removal at each position independently, does not accurately represent the initial error profile.

7.5 Deconvolution method for form control

7.5.1 Calculation of required integrated dwell time

In order to circumvent the problems of the polishing scheme using the unit material removal profile, a different approach based on deconvolution was developed to reduce the form error. It has been reported that MRF[34, 61] technique used such method, whose details are not revealed. When only the *radial* profile of the form error is

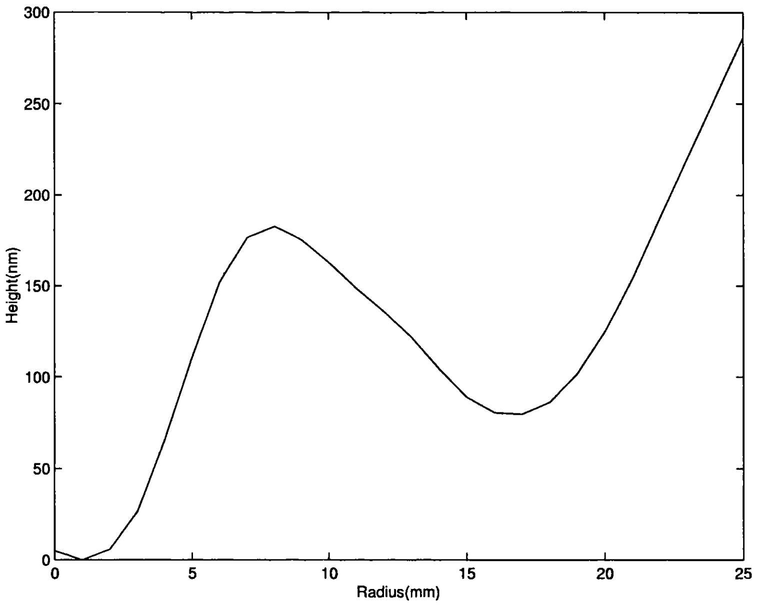

Figure 7.8: Initial surface radial profile of a rotationally symmetric glass sample for the deconvolution method

considered, the profile can be thought of as the convolution of the profile of the material removal rate, or the influence function profile of the spinning compliant tool, and the integrated dwell time at each position of the tool on the radius.

Conversely, by deconvolving the influence function profile out of the initial form error, the integrated dwell time at each position of the tool on the workpiece can be calculated. The beauty of this method is that the result of deconvolution directly gives the integrated dwell time at each point, which already has taken the convolution effects into account.

Figure 7.8 shows the radial profile of an arbitrary (aspheric) surface. It was deliberately polished arbitrarily, but axially symmetrically, to be used as an initial surface. It was used as the initial surface error for the deconvolution method as the objective was to make a sample flat. The initial surface had 286 nm (=0.45λ) of peak-to-valley error.

It was noticed from the previous section that special consideration should be taken near the centre of the workpiece. The initial error profile of Figure 7.8 suggests that near the centre of the workpiece is the minimum point and it should not even touched around the centre. Also, as shown in Figure 7.3, the influence function of the tilted spinning compliant tool is itself inclined. This suggests that tool sweeping

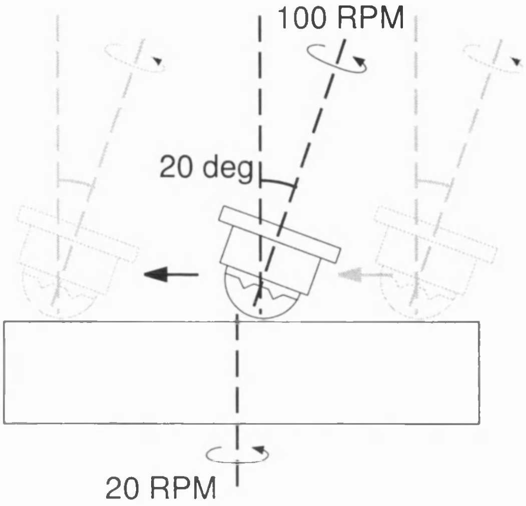

Figure 7.9: Illustration of full diameter sweep by an SCT: from one edge to the centre, then to the opposite edge

back and forth on the workpiece radius would be better than a single pass in order to average the tool marks. Since the workpiece is rotating, sweeping once across the diameter is equivalent to sweeping back and forth on the radius. Therefore, it was decided to sweep the tool across the diameter of the workpiece according to the integrated dwell time calculated at each point.

Note that in the case of a precessing tool (see Chapter 6), only a single radial motion is required. This is because the precession provides the averaging function, and in multiple (or all) directions as well.

The diametric tool-path had another advantage in reducing the effect of possible inclination of the turntable, or the mounting of the workpiece, with respect to the tool traverse. This was of particular concern as the prototype CCPM was not adequately stiff. Therefore, the deconvolution was carried out from the workpiece edge to the centre, then from the workpiece centre to the opposite edge.

The deconvolution was calculated by solving for the $1 \times n$ array of integrated dwell time (IDT) in the following matrix equation:

$$IDT * A = \begin{pmatrix} t_1 & t_2 & \cdots & t_n \end{pmatrix} \begin{pmatrix} F & 0 & \cdots & 0 \\ 0 & F & \cdots & 0 \\ & & \ddots & \\ 0 & 0 & \cdots & F \end{pmatrix} = E \qquad (7.1)$$

Each element represents the integrated dwell time for each position of the tool, and A is the matrix whose rows represent the profiles of the influence function vectors being shifted by 1 mm over one radius of the workpiece. F is the $1 \times m$ array of influence function, which is the profile of 3D influence function in Figure 7.3. E is the initial error profile which is also the targeted amount to be removed expressed as a $1 \times m$ array. By solving the equation by least square method, IDT can be calculated, where n is the length of the error vector E subtracted by that of F.

Mathematically, IDT can have negative elements, and with the negative elements, the convolution of IDT and F generates near perfect profile of E except at both ends of the scanning. However, since neither time nor material removal can be negative, the lowest negative element was shifted up as zero. This renormalisation process results in imperfect profile of E and this is also why more than one radial sweep is required.

Surely, if negative elements effectively 'add' material, then renormalising is the same as making the sample thinner overall, which gives no effect on form control.

Figure 7.10 shows the non-negative (all the negative values shifted up to zeros) integrated dwell time for each tool position on the workpiece. Figure 7.10 (a) is for the sweep of the first radius of the workpiece, and Figure 7.10 (b) is for the second half. For the second half of the workpiece, the tool was swept until the last inner edge of the tool touches the workpiece radius of 25 mm in order to reduce the peak at the edge, as it can be seen in Figure 7.10 (b) where it shows more tool positions.

7.5.2 Total polishing time and material removal prediction

The required integrated dwell time was calculated along the radius of the workpiece. However, as the workpiece is rotated to polish the whole area on the surface, the effect of rotation has to considered. Since the tool size is much (10 times) smaller

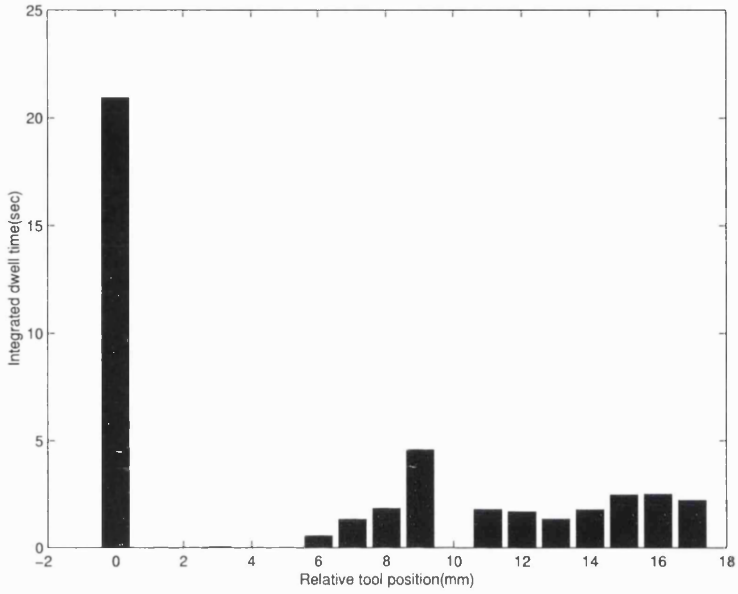

(a)

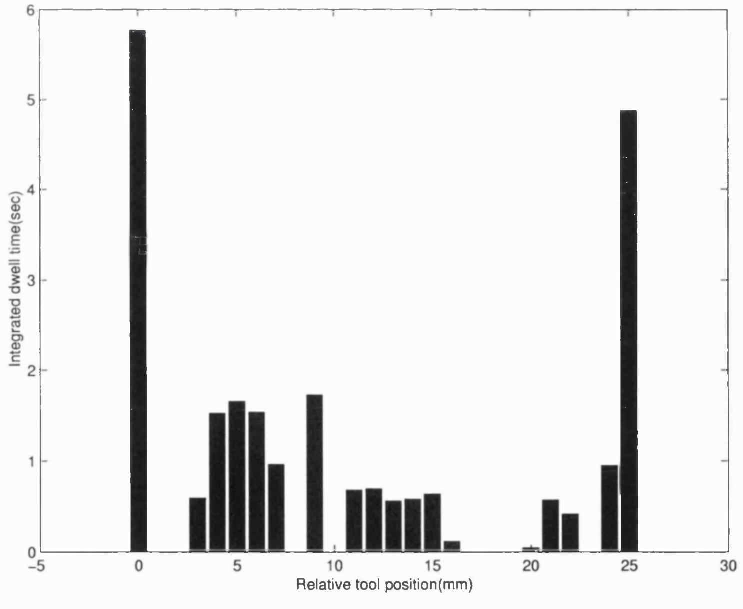

(b)

Figure 7.10: Non-negative *IDT* required for: (a)first radius of the workpiece (from the workpiece edge to centre), (b)second radius of the workpiece (centre to the other edge

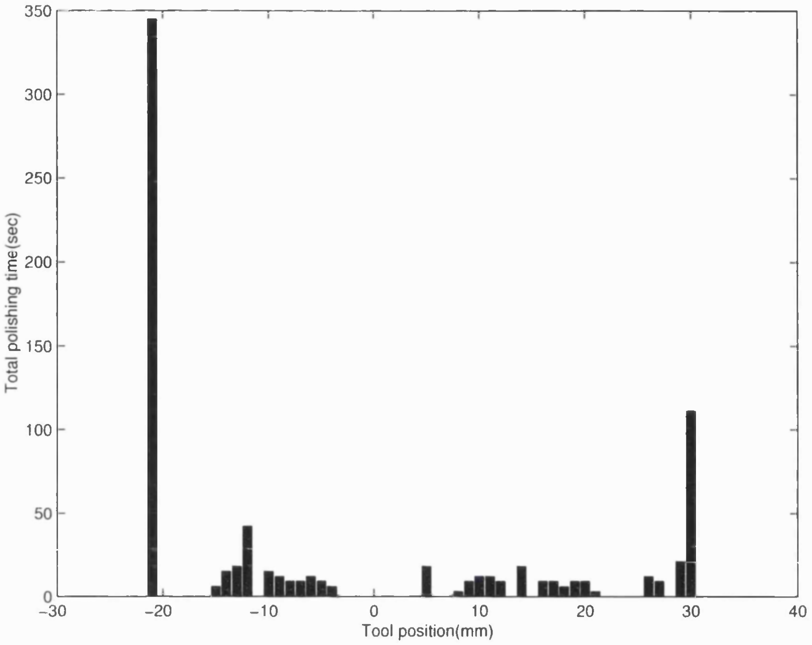

Figure 7.11: Total polishing time across the workpiece: scanning from one edge through the centre to the opposite edge

than the workpiece size, when there is one rotation of the workpiece and the tool at $\rho(x, y)$ position on the workpiece produces an annular groove, a point on $\rho(x, y)$ experiences integrated dwell time which is a fraction of the rotation period.

At any radial position on the workpiece, the integrated dwell time per one turntable rotation, or unit integrated dwell time, can be calculated once the tool size and turntable RPM are known. The details of the geometry for the calculation is in Appendix C. With the required integrated dwell time and the integrated dwell time per one rotation, the total polishing time at a radial tool position can be calculated as follows.

$$TPT_i = T \times \frac{IDT_{required}}{IDT_{unit}}, \tag{7.2}$$

where TPT_i=total polishing time at each radial polishing position, T=turntable rotation period, $IDT_{required}$=required integrated polishing time calculated by the deconvolution method, and IDT_{unit}=unit integrated polishing time calculated as in Appendix C.

The total polishing time across the workpiece diameter s plotted against the tool position on the workpiece is shown in Figure 7.11.

With the total polishing time based on the renormalised integrated dwell time, the amount of material removal can be predicted by convolving it with the profile of influence function, which is calculating $IDT * A$ in equation 7.1. Figure 7.12 (a) shows the first half of the workpiece, from left to right, swept from the edge towards the centre of the workpiece. It shows the profile of influence function, the initial surface profile, the predicted amount of material removal, and the residual error. The residual error is flipped horizontally and then fed as the new initial surface into sweeping of second half of the workpiece as shown in Figure 7.12 (b). This also shows the predicted material removal and residual error of less than 40 nm (peak-to-valley).

7.5.3 Result of the form control experiment with the SCT and conclusion

Finally, the spinning compliant tool polishing/figurring experiment is carried out on the initial surface of Figure 7.8, using the calculated total polishing time at each radial tool position.

The final polished surface is shown in Figure 7.13, compared with the initial surface. The radial sweeping with the CCPM could not be done continuously, but discretely by 1 mm. The tool had to be polished on one location, then is was lifted, radially moved 1 mm, then pressed down again on the workpiece. Repetition of this task through the workpiece diameter took 1 hour of total work. However, it should be noticed that the sum of the pure polishing time ($\sum_i TPT_i$) was less than 13 minutes. Within 13 minutes the 50 mm diameter workpiece with the initial error of 286 nm (0.45 λ) was reduced to 177 nm (0.28 λ).

The achieved form improvement factor is 38% per one polishing run, in less than the total polishing time of 13 minutes. (The previous work[57] on the OSL active lap does not reveal the total polishing time.) However, it should be noticed that compared to the 10% of improvement factor of the OSL active lap per one polishing run, it is a considerable improvement in the convergence rate to the target surface. It has been also reported that the Steward Observatory Mirror Lab's stressed-lap has achieved 11-13%[57], and the Litton Itek's CCOS has achieved average 17%[48]

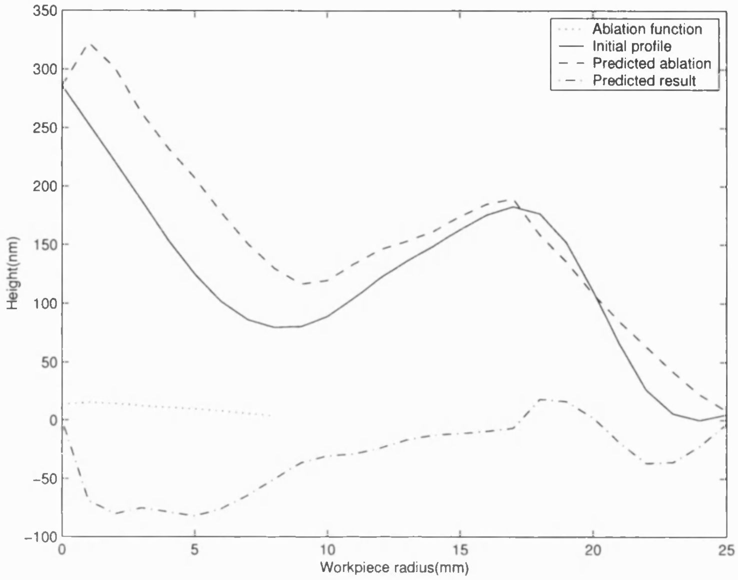

(a)

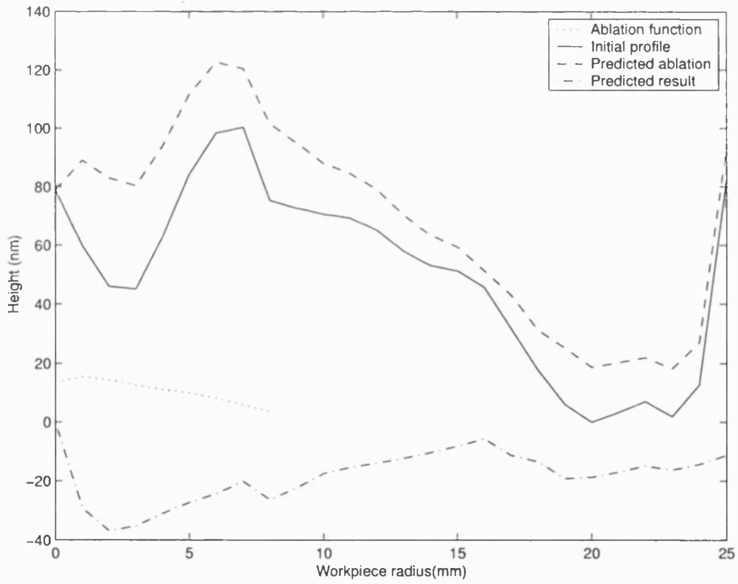

(b)

Figure 7.12: Material removal prediction by deconvolution method: (a)first radius of the workpiece(from edge to centre), (b)second radius of the workpiece (from centre to the other edge)

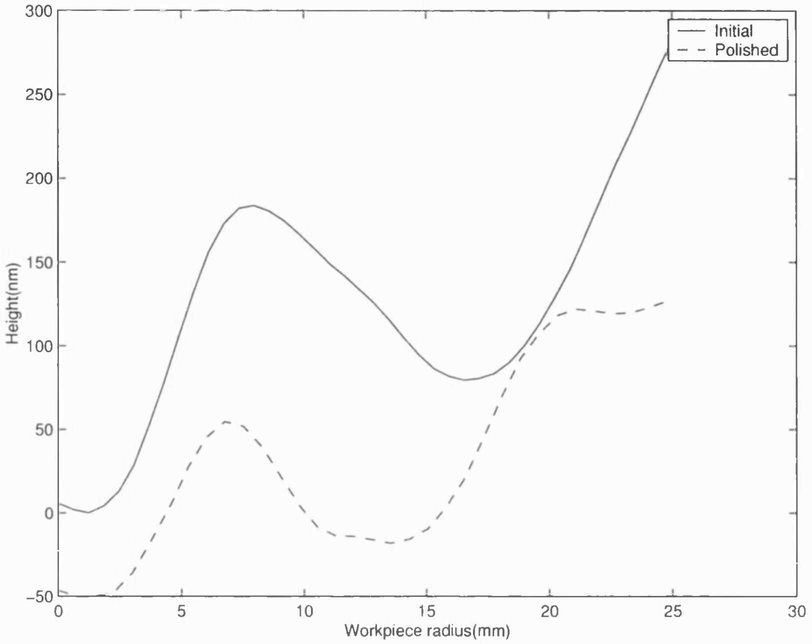

Figure 7.13: Initial and final surface profiles

of form improvement factors.

More importantly, for the OSL active lap polishing, the polishing strokes and dwell time were decided by an experienced optician. For the case of the SCT polishing, with a relatively simpler polishing strategy, the SCT dwell time is calculated by an algorithm, and thus the polishing process can be automated.

The result of this polishing experiment with the spinning compliant tool shows the feasibility of the technique: an attractive alternative to the conventional pitch tool polishing for aspheric production. Due to the limits of time and availability of indstry owned equipment, extensive repeatability experiments were not carried out for this thesis. Possible future improvements are described in the following section.

7.6 Discussion and future work

During the calculation of the required dwell time and total polishing time, it was found that the total polishing time is very sensitive to the dimension of the tool footprint. Even 1 or 2 mm of difference in the size of the footprint in the calculation, resulted in several minutes of difference in the total polishing time. It implies that the position accuracy in the spinning compliant tool polishing is also an important factor in estimating the total polishing time, and thus the material removal. Since the polishing head of the CCPM was tilted, it was difficult to position the tool contact on the centre of the workpiece with the accuracy better than ±1 mm. This must have affected the polishing result as well. It is known that the prototype CCPM has tool positioning errors in the mm regime.

In this experiment, the material from an arbitrary aspheric surface was removed, targeting a flat surface. It implies that vice versa, manufacturing an aspheric surface starting from a flat or an arbitrary surface is also achievable. For the future research, the following areas of work are proposed to achieve better results in producing aspheric surfaces with the spinning compliant tool.

Firstly, the improved accuracy in positioning of the spinning compliant tool is essential. If a spinning compliant tool whose spinning axis is horizontal, as shown in Figure 7.14 were developed, it could polish shallow aspheric surfaces without tilting the polishing head and this can give higher centering accuracy. The tilt of the polishing head can be added for polishing steep aspheric surfaces, provided the positioning problem is solved.

However, with the tilted spinning compliant tool used for this chapter, the workpiece is experiencing opposite spinning direction when the tool is swept across the diameter of the workpiece as shown in Figure 7.15 (a). This results in undesirable lower material removal for the second radius of sweeping. If a horizontal spinning tool as proposed here can be used, the problem can be solved as shown in Figure 7.15.

Secondly, the experimental work in this thesis was undertaken with the CCPM machine having the cantilever polishing arm, with the addition of a prototype spinning compliant tool added to the CCPM. This resulted in a vibrational problem with the higher tool RPM. Although this has since been superseded by a re-build with a bridge-type structure which is stiffer, a redesign of the spinning mechanism interface is required for even stiffer structure to experiment in the higher removal rate. This has led to a radical re-design of the industrial machine, which is currently in progress.

Thirdly, an automated process for the continuous sweeping can make the whole polishing process more rapid. In the experiment for this chapter, the intermittent

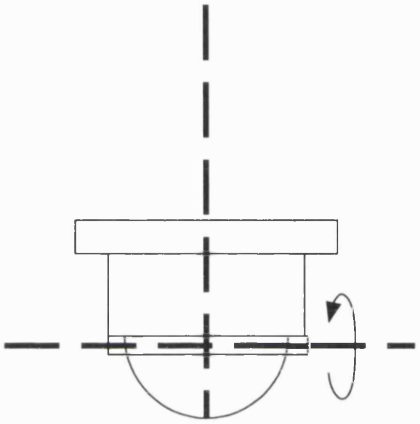

Figure 7.14: A rotating compliant tool with a horizontal spinning axis

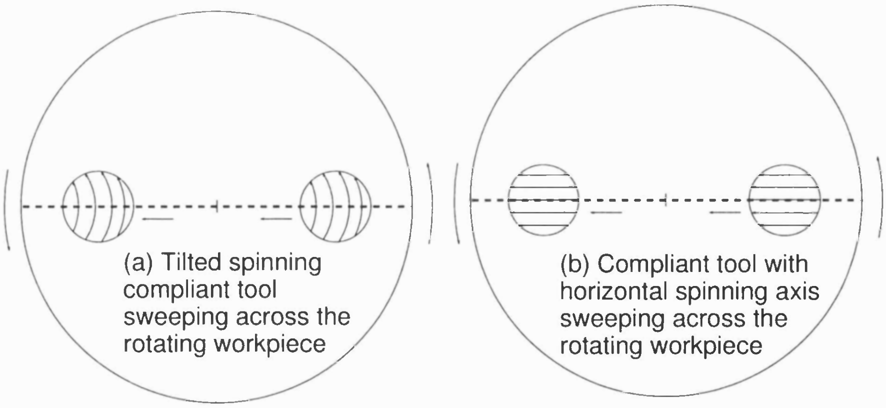

(a) Tilted spinning compliant tool sweeping across the rotating workpiece

(b) Compliant tool with horizontal spinning axis sweeping across the rotating workpiece

Figure 7.15: Comparison of tilted spinning tool polishing and horizontal spinning tool

sweeping process consisted of iterations of lowering the tool on the workpiece, polishing, lifting the polishing head, shifting the head, then lowering the tool again for polishing at the next tool position manually. If the sweeping can be done continuously without lifting the tool dwelling at each position as calculated, the whole polishing time can be substantially reduced. For example, for the SCT form control experiment described in this chapter, 1 hour can be reduced to near 13 minutes. Extra control software is required to feed the pre-calculated total polishing time at each tool position, while sweeping the tool.

Fourthly, the bound-abrasive polishing cloths as proposed in [31] can also make the polishing process simpler for spinning compliant tool polishing. In the experiment with a spinning compliant tool in this thesis, a polishing cloth was used with the occasional supplies of the abrasive. If the abrasive can be embedded in the polishing cloth, then an external supply of abrasive can be minimised or is not required, and the drainage system for the polishing machine can be simpler and cleaner. However, epoxy was used as the base for the abrasive in [31], which is not compliant when it hardens. Softer embedded abrasive polishing cloths need to be developed to be attached to the air-filled compliant material.

The deconvolution method in this thesis is used assuming the surface is rotationally symmetric. Hence, the extension to the deconvolution method from 1D (finding the integrated dwell time (IDT) on the workpiece radius) to 2D (finding the IDT on any location on the surface area) will enable the spinning compliant tool polishing method to polish non-symmetric aspheric surfaces, or remedy non-axially symmetric errors in axially symmetric surfaces. The extension of the radial deconvolution to the deconvolution over the whole workpiece area is a possibility to calculate the dwell time for a non-axially symmetric workpiece. Litton Itek [49] has used its dwell time control technique to polish an off-axis paraboloid. It has not published the details of its proprietary process in terms of material removal rate.

Lastly, as discussed for the case of the pitch tool polishing in chapter 3, the active pressure servo mode for the SCT polishing might lead to even faster form convergence. The redesign of the pressure sensing part of the CCPM is required to run the active servo mode with the SCT.

Chapter 8

Index of manufacturability for aspheric surfaces produced with spinning compliant tools

8.1 Introduction

In order to utilise the advantages of aspheric optics, the production should be more cost-effective compared to predominant spherical optics production. It can be beneficial if an optical designer can choose one aspheric design which is more readily manufacturable over other aspheric designs, at the designing stage. The idea of index of manufacturability (IOM) is to help designers to consider the difficulty, and thus cost of production, at the design stage. Even if the performance of an optical design is exceptionally good, it is of little use if it is very difficult to manufacture.

The work in this chapter starts from the question: "how can an optical designer quantify how much more difficult aspheric design is more difficult to manufacture than other aspheres?" The limitations to an existing method to calculate index of manufacturability are raised, which was designed to be used with pitch tools. However, with the development of spinning compliant tools, by which the underlying hypothesis of Foreman's method is no longer appropriate, an alternative method to estimate the manufacturability in aspheric polishing with a spinning compliant tool is proposed and demonstrated.

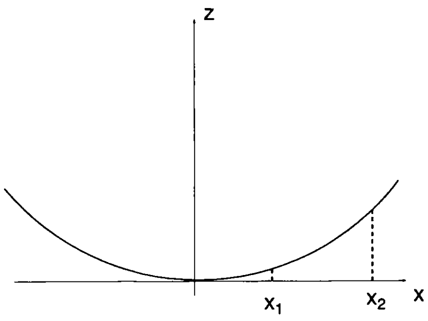

Figure 8.1: Geometry of an arbitrary concave aspheric surface

8.2 Index of manufacturability in the past

The pitch tool has been the dominant choice of tooling for polishing/figuring aspheric optics fabrications. Due to the varying radius of curvature of an aspheric design and the slow conformality of pitch, the pitch tool should be sufficiently small to minimise the mismatch problem.

Based on the slowly conforming characteristic of pitch tool, Foreman [28] had proposed a numerical measure of the manufacturability of aspheric optical surfaces as an objective measure of the degree of difficulty involved in manufacturing an optical element with an axially symmetric aspheric profile. Foreman's measure is based on the hypothesis that the difficulty involved in fabricating an aspheric surface is directly related to the rate at which the radius of curvature along a tangential profile of the surface changes with distance from the optical axis. Defined for the off-axis segment within the profile, the dimensionless index of manufacturability is mathematically defined as

$$\mu = \left(\frac{dR}{dx}\right)_{avg} = \left(\int_{x_1}^{x_2} \frac{dR}{dx} dx\right) / \left(\int_{x_1}^{x_2} dx\right) = \frac{R(x_2) - R(x_1)}{x_2 - x_1}, \tag{8.1}$$

where $R(x)$ is the radius of curvature of the tangential profile of an aspheric surface at a distance x from the optical axis. When $x_1 = 0$ and x_2 is the radius of the sample, the index for the whole radius of a symmetric aspheric surface can be calculated. The cross section of an aspheric surface when $y = 0$ is illustrated in Figure 8.1.

An aspheric surface[70] can generally be described as

IOM (μ) rage	Classification
5.0<	Extremely difficult; may challenge current state of the art
1.0 - 5.0	Quite difficult
0.1 - 1.0	Moderately difficult
0.01 - 0.1	Average difficulty
0.001 - 0.01	Simple

Table 8.1: Table of IOM classification by Foreman[28]

$$z = \frac{cs^2}{1+\sqrt{1-(K+1)c^2s^2}} + A_4 s^4 + A_6 s^6 + A_8 s^8 + \cdots, \tag{8.2}$$

where $s^2 = (x^2 + y^2)$ and A_4, A_6,$\cdots$ are the aspheric deformation constants. The constant c is the reciprocal of the on-axis radius of curvature $R(0)$, and K is the conic constant. $R(x)$ can be derived as follows (see for example [76]).

$$R(x) = \frac{\left[1+\left(\frac{dz}{dx}\right)^2\right]^{3/2}}{\frac{d^2z}{dx^2}}. \tag{8.3}$$

It is clear that $\mu = 0$ when the surface is a sphere, and μ becomes larger as the average of dR/dx between x_1 and x_2 increases.

Foreman built a table of IOM as shown in Table 8.1 based on the empirical estimations by experienced opticians, and aspheric designs with larger IOM are classified as more difficult to manufacture.

There exists a different method in measuring difficulties for aspheric production by Mercier [29] with a different approach, but it is limited to aspherics deformed only from spheres and applicable to narrower range of aspherics, hence it is not considered here.

8.3 Foreman's IOM and fundamental limitations

While applying the Foreman's definition of IOM on some example aspheric forms, it became evident that it could not give meaningful numbers for certain types of aspheric surfaces. In a case when $R(x_2)$ is smaller than $R(x_1)$, μ becomes negative.

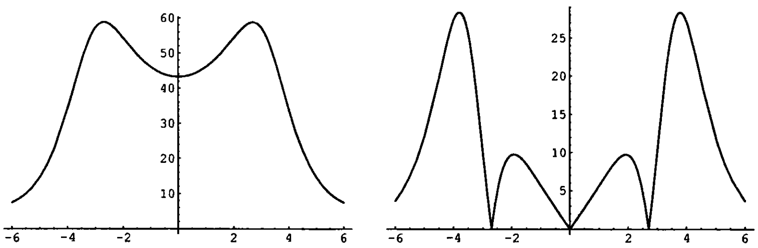

(a)$R(x)$ against x (b)$|dR/dx|$ against x

Figure 8.2: $R(x)$ and $|\frac{dR}{dx}|$ of aspheric surface Asph1 plotted against the distance x from the centre

Moreover, it was realised that simply averaging the dR/dx was not sufficient to describe the complexity of the profile. For instance, the real case of a 12 mm diameter aspheric mould sample with $c = 0.0231, K = -28.4, A_4 = -7.61 \times 10^{-5}, A_6 = 1.16 \times 10^{-6}, A_8 = 1.07 \times 10^{-7}, A_{10} = -1.04 \times 10^{-9}$, has $R(x)$ as shown in Figure 8.2 (a).

Not only is the Foreman's index μ negative in this case, but also the μ is not distinguishable with any other case with same endpoints $R(x_1)$ and $R(x_2)$. (e.g. a case when $R(x_1)$ and $R(x_2)$ respectively have the identical values as the above $R(x_1)$ and $R(x_2)$, but $R(x)$ is monotonically decreasing, which can have significant difference in difficulty of manufacturing.)

In order to avoid the above problem modifications to Foreman's definition were attempted. The assumption was made that dR/dx would equally contribute to the difficulty if the absolute value is the same, and the average of absolute values of dR/dx was considered so that all the $R(x)$ values contribute to the index, not only the two end points. The physical meaning is that both increase and decrease of the $R(x)$ contribute to the difficulties of fabrication since change in the radius of curvature requires different tools with different radius of curvature. Therefore the enhanced index of manufacturability μ' is defined as

$$\mu' = \left|\frac{dR}{dx}\right|_{avg} = \left(\int_{x_1}^{x_2} \left|\frac{dR}{dx}\right| dx\right) / \left(\int_{x_1}^{x_2} dx\right). \tag{8.4}$$

For the analytic calculation for $\frac{dR}{dx}$ and the numerical calculation of μ', Mathematica was used. While most of the examples passed the test, it was discovered that numerical calculation of μ' is not possible when there is a sharp valley in the graph

	⌀(mm)	c	K	A_4	A_6	A_8	A_{10}
Asph1	12	0.0231	-28.4	-7.61×10^{-5}	1.16×10^{-6}	1.07×10^{-7}	-1.04×10^{-9}
Asph2	65	9.22×10^{-3}	-1.53	-3.75×10^{-7}	0	0	0
Asph3	150	1.11×10^{-3}	-1	0	0	0	0
Asph4	850	2.68×10^{-4}	-2.86	0	0	0	0
Asph5	5	2.35×10^{-1}	-3.62	1.76×10^{-3}	-6.97×10^{-4}	2.38×10^{-5}	-1.17×10^{-5}

Table 8.2: Examples of aspheric designs

of $|\frac{dR}{dx}|$, such as in the Figure 8.2 (b). In the above case, $R(x)$ has a maximum between the centre and the edge, and this causes a sharp peak for $\left|\frac{dR}{dx}\right|$.

Taking the RMS average was next tried as an alternative, which does not give any sharp valley problem for numerical calculation. Therefore the new enhanced index of manufacturability η was defined as

$$\eta = \left(\frac{dR}{dx}\right)_{RMS} = \sqrt{\left(\int_{x_1}^{x_2} \left(\frac{dR}{dx}\right)^2 dx\right) / \left(\int_{x_1}^{x_2} dx\right)}. \tag{8.5}$$

The modified index of manufacturability η was tested on some actual aspheric designs in Table 8.2, where $c, K, A_4, A_6, A_8, \cdots$ are as described in Equation (8.2). The $R(x)$ of aspheric surface Asph2, Asph3, Asph4, and Asph5 are illustrated in Figure 8.3.

Asph1 is a case when the $R(x_2)$ is smaller than $R(x_1)$. Asph2 is an asphere deformed from a hyperboloid, Asph3 is a paraboloid, Asph4 is a hyperboloid, and Asph5 is a Schmidt plate. Since the RMS values are always greater or equal to average values, η tends to be greater than μ.

However, there is a fundamental limit to the method of Foreman's and its variants. For the case of Schmidt plate (Asph5), IOM can not be defined due to the singularity in $R(x)$. When a design has a point of inflection where the $R(x)$ changes its sign as in the Schmidt plate shown in Figure 8.3 (d), neither Foreman's index nor modified version can classify the surface correctly. The Foreman's definition of μ simply ignores the asymptotic change of the $R(x)$ in the middle, and the integration in the modified index η can not be defined for singular points when $R(x) = \pm\infty$.

In order to avoid the singularity problem, $C(x) = 1/R(x)$ was attempted to replace $R(x)$ in the definition η, thus using $\eta = \sqrt{\int_{x_1}^{x_2} \left(\frac{dC}{dx}\right)^2 dx / \int_{x_1}^{x_2} dx}$, but it was found

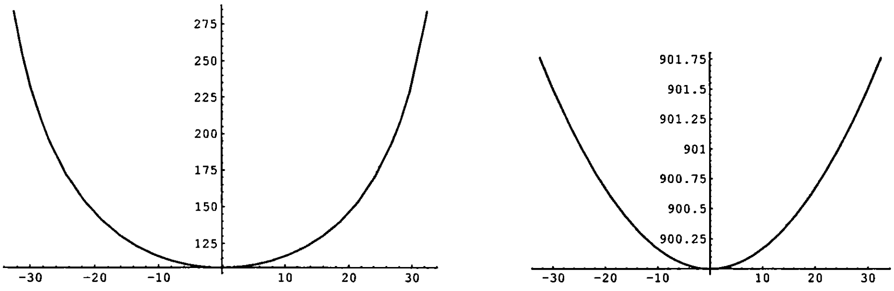

(a) $R(x)$ of Asph2 (b) $R(x)$ of Asph3

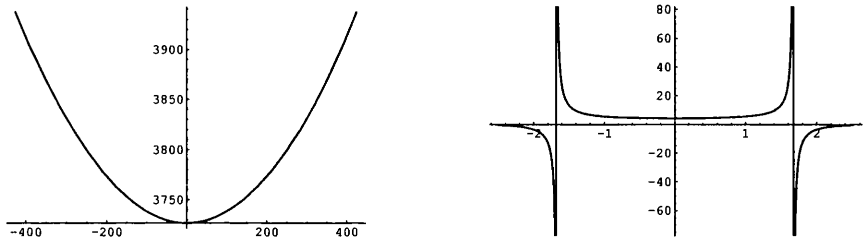

(c) $R(x)$ of Asph4 (d) $R(x)$ of Asph5 (Schmidt plate)

Figure 8.3: $R(x)$ of aspheric surfaces Asph2, Asph3, Asph4, and Asph5(Schmidt plate)

inappropriate since dC/dx is in fact $-\frac{1}{R^2}\frac{dR}{dx}$, which behaves differently from dR/dx, and thus looses the physical meaning unlike dR/dx does in Foreman's hypothesis.

8.4 Proposed index of manufacturability for compliant tool polishing

The limit comes from the underlying hypothesis in the Foreman's method that the manufacturing difficulty lies in the degree of change in the radius of curvature in an aspheric surface. This is the case with pitch tool polishing. More rapidly changing radius of curvature would require smaller pitch tool due to the slow conformality of pitch, hence longer manufacturing time.

However, when a spinning compliant tool is used, the degree of changing radius of curvature (dR/dx) of the target asphere hardly contributes to the manufacturing difficulty as the tool naturally conforms to the surface almost all the time. Therefore, a new method of measuring the difficulty in polishing aspheric optics with spinning compliant tool is proposed in this chapter.

The new *volumetric* index of manufacturability is defined as the volume to be removed - i.e. the volume difference between an initial surface and the target surface. With a spinning compliant tool and same polishing parameters (e.g. tool spinning RPM), the manufacturing time depends on the volume of material to be removed. Without the role of dR/dx, this simpler and more intuitive method is proposed as a new measure of manufacturability.

Unlike a pitch tool, a spinning compliant tool has an influence function, or volumetric removal rate, which is applicable even when there is no stroke. Once the volume to be removed is calculated, and a volumetric removal rate is given, it is possible to estimate the total polishing time as long as the tool is continuously polishing.

8.5 Selection of initial surfaces for polishing an aspheric surface

The choice of initial surface becomes of an interest in order to minimise the volume to be removed. There exist several methods to choose an initial surface from spheres of different definitions (or non-spherical surfaces) depending on the target asphere design and the polishing/figuring method. Different kinds of initial surfaces are reviewed before a method is chosen as suitable for spinning compliant tool.

8.5.1 Initial spheres

Traditionally, aspheres are manufactured from best-fit spheres since sphere can be manufactured using standard techniques. There exist different ways to calculate an initial sphere before aspherisation of the target asphere.

Minimum volume sphere

The most common practice used in industry to select an initial surface is to calculate the sphere, which gives the minimum volume to be removed, proposed by Unti [108]. It is defined for a general aspheric surface with axial symmetry. Unti's method to calculate the minimum volume sphere is to minimise both the deviation Δz, or the initial sphere profile minus the target asphere profile, and the volume V obtained by revolving the deviation around the axis.

However, Unti's method seems unnecessarily over-complicated as the solutions to the simultaneous equations ($\frac{d(\Delta z)}{dx} = 0, \frac{dV}{dR} = 0$) require complex calculations. More seriously, the former of the simultaneous equations, or $\frac{d(\Delta z)}{dx} = 0$, which is a condition to find a minimum deviation point, is not physically meaningful in the course of finding the minimum *volume* to be removed. It is discussed further later in this chapter (compare Figure 8.8 and 8.4) that the minimum deviation does not guarantee the minimum volume in rotationally symmetric surfaces.

In order to find an alternative method to calculate the minimum removal-volume sphere, a simpler numerical method was successfully developed with MATLAB. The algorithm of this method is explained later with examples. (See Figure 8.8.)

Minimum edge error sphere

Vázquez-Montiel *et al* [111] pointed out that the minimum volume sphere might not be always practical in terms of possible turned-down edge error in actual manufacturing.

For instance, a concave paraboloidal surface usually has the minimum volume sphere touching the conic surface at the 70% of the semi-diameter of the conic workpiece, which requires further polishing around the edge and can introduce turned-down edge.

The minimum edge error sphere is defined so that the initial sphere resembles the target asphere near the edge and reduce the volume to be removed near the edge lest it should be turned-down.

Mathematically expressed, the sphere touches the conic at the edge of the conic, and they both have identical tangent surface slope of tangent at the edge. The resulting sphere usually requires larger amount of material to be removed than that from the minimum volume sphere, but there is a trade-off between the risk of turned-down edge and larger amount of material to removed. Figure 8.4 compares an example of a minimum-volume sphere and a minimum edge error sphere. A disadvantage of this method is that it can not be used with a Schmidt type target asphere.

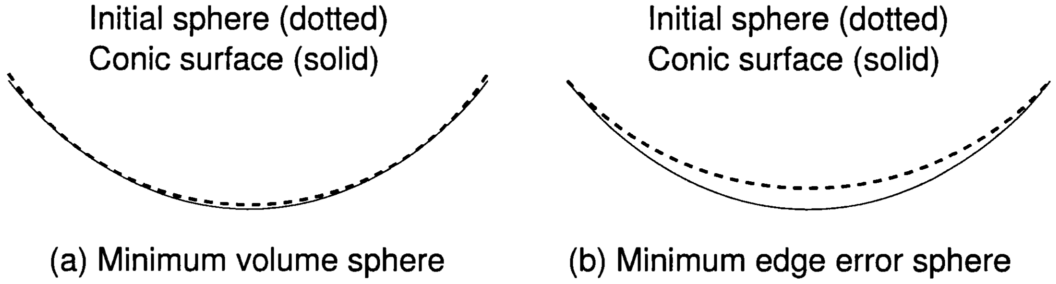

(a) Minimum volume sphere (b) Minimum edge error sphere

Figure 8.4: Minimum volume sphere and minimum edge error sphere

Envelope sphere

Briers [8] reported some occasions when an initial sphere called the "envelope sphere" gives a minimum *deviation* from an asphere, rather than minimum volume, which might be preferred for SPDT machining where machining time is governed by the deviation. An envelope sphere is defined as a sphere which touches the target asphere at the vertex and the edge. When the profile of an asphere is given, the envelope sphere can be calculated by solving simultaneous equations given by two points - the vertex and the edge.

It can be useful when the target asphere is a Schmidt plate. In fact, the envelope sphere for a Schmidt plate is also the minimum volume sphere, which should be self-evident. (See Figure 8.9 (a) for the profiles of a Schmidt plate and the envelope sphere. No other sphere can give smaller removal volume than envelope sphere.)

One explicit circle on the same axis is decided when two points are given. It can be also useful when the target asphere has a central hole. The two points for the simultaneous equations become the outer and inner edge.

Minimum least-mean square (LMS) deviation sphere

It is a method used by a number of optical designing software (e.g. Zemax [27]). This method is calculating the sphere with the minimum RMS deviation from the target asphere, literally the best-fit sphere. Although it can produce mathematically the closest fit to the target asphere, practically the volume of material to be removed may not be the minimum. Since the minimum LMS deviation sphere may give negative deviation, the whole sphere has to be elevated in order to give greater than zero deviation, and thus this method is not ideal to minimise the volume to be removed.

8.5.2 Miscellaneous initial surfaces

Non-spherical surfaces can also be used as initial surfaces, especially in case when SPDT or grinding machines are used to generate form.

Initial surface by multi-step spheres

Fähnle *et al* [24] reported a method to produce an optimum initial surface which can be used with tubular types of tools. A series of spheres with different radii are ground starting from a sphere which touches the edge of the target asphere. At each stage a different sphere is machined at the point with the maximum *normal* distance - not the maximum vertical deviation - between the current surface and the target asphere. The multi-step sphere grinding process is stopped once the amount of material left to be removed is smaller than a preset value. In the end, the optimum initial surface becomes like a gramaphone record disk (i.e. high-frequency error) rather than a sphere. There is also a trading off between the time grinding several different spheres and the time to polish the target asphere.

Initial surface by aspheric grinding machine

Recently, Ruckman *et al* [81, 96] have reported that CNC aspheric grinding machines are being developed, which directly grind aspheres before polishing stage. Therefore, the initial surface is not a sphere, but a near target asphere which should shorten the polishing time. For future work, this kind of initial asphere might be used if grinding capability is combined with the CCPM used in this thesis.

8.6 Volumetric index of manufacturing

Among the different kinds, the most appropriate initial surface should be used case by case as discussed above. However, as the minimum volume sphere method is directly related to the newly defined volumetric index of manufacturability with spinning compliant tool, and also as this method can safely handle Schmidt plate, this method is selected here.

Rather than using Unti's method [108] to calculate the minimum volume, a numerical method is developed for the reasons mentioned earlier.

With an asphere axially symmetric around z-axis, the volumetric index of manufacturing V, or the volume to be removed between the initial and target surfaces can be calculated as the solid of revolution of the deviation profile:

$$V = 2\pi \int_{0}^{D/2} x[z_i(x) - z_t(x)]dx, \tag{8.6}$$

where $D/2$ is the semi-diameter of the workpiece, $z_i(x) = b \pm (R^2 - x^2)^{1/2}$ is the profile of the initial sphere and $z_t(x)$ is the profile of the target asphere as described in Equation 8.2. b is the z-coordinate of the centre of the initial sphere, and R is the radius of the sphere.

Depending on whether the target asphere is concave or convex, and whether the first sphere with $R_0 = 1/c$ as its radius, touching the vertex of asphere is inside or outside of the asphere, the radius of sphere R is gradually increased or decreased to calculate V. For each radius of sphere, the sphere is lifted up above the asphere to give always non-negative volumes as the asphere is polished from the sphere. By doing so, the R and b of the initial sphere which gives minimum V can be found.

Figure 8.5 shows an example of the process. It shows the profiles of the target asphere and spheres. Figure 8.5 (a) shows the target asphere and the osculating sphere which has the same radius of curvature R as the asphere at its vertex. The R is gradually increased (Figure 8.5 (b)), and the sphere is lifted up (Figure 8.5 (c)) to give always non-negative volumes to be removed, and finally the sphere which gives the minimum volume is found(Figure 8.5 (d)). Figure 8.6 shows the plot of V against R, so that the R which gives the minimum V can be chosen.

In order to apply the minimum volume sphere method and volumetric index of manufacturability, a set of aspheres is examined. In Figure 8.7, it shows an example of lens system (a projection lens system [124]) obtained from a lens design database software LensView[84], which uses various plastic aspheres of similar sizes, including

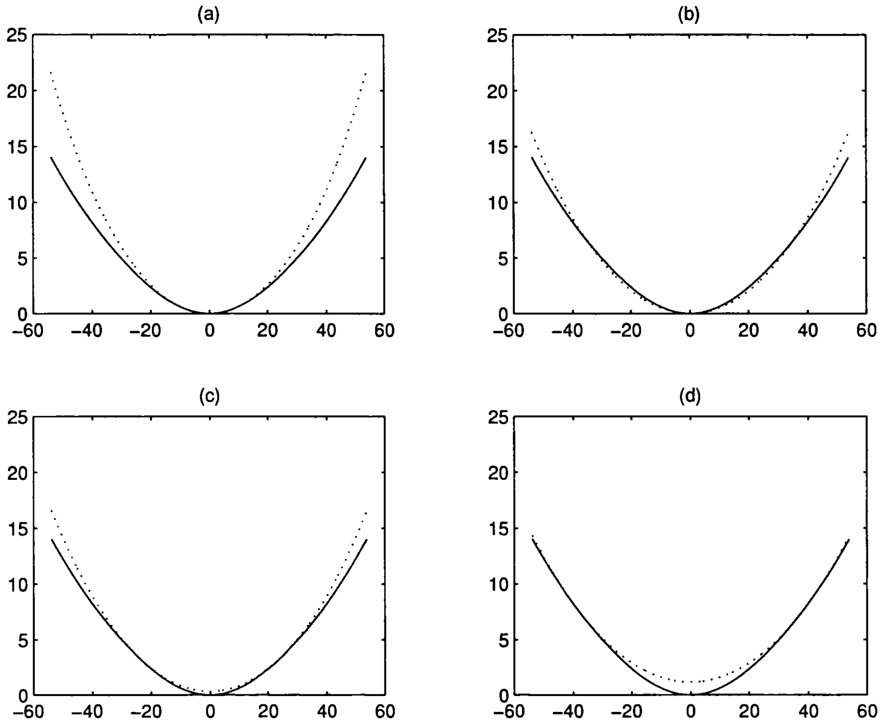

Figure 8.5: Process of finding the minimum volume sphere for Surf3 (solid: asphere, dotted: spheres evolving from (a) to (d))

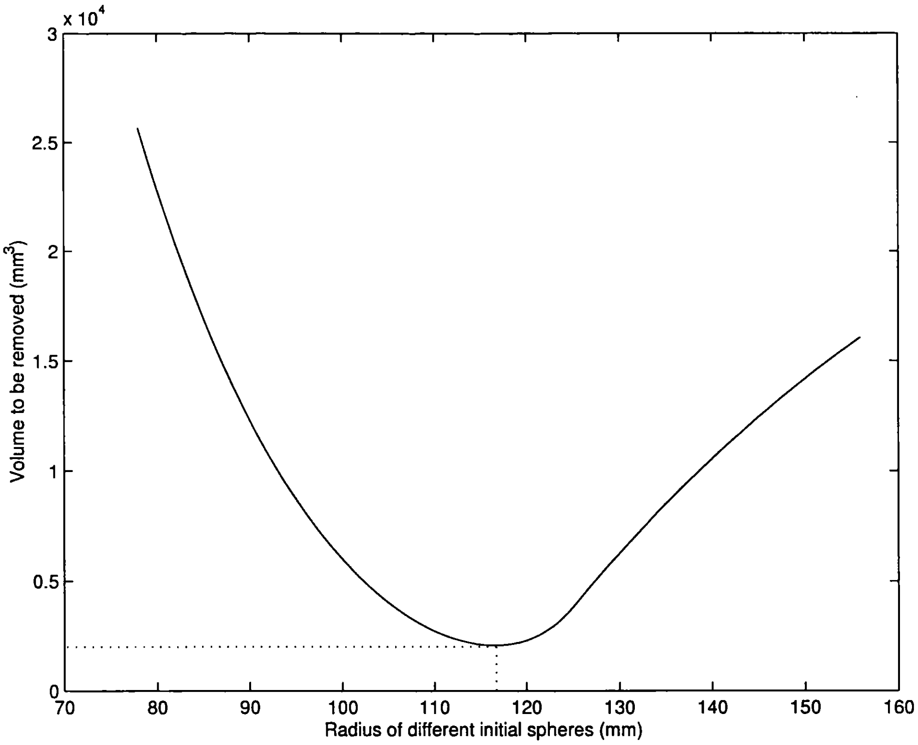

Figure 8.6: Choice of radius for the sphere as the minimum volume sphere for a concave asphere

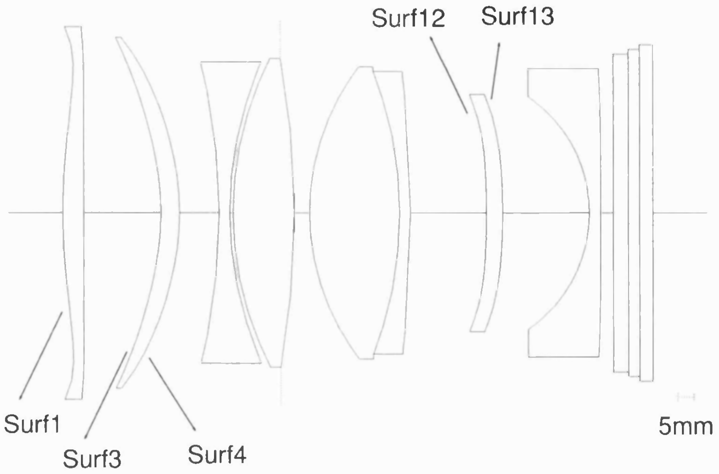

Figure 8.7: Example of an optical system utilising aspheres

	⌀ (mm)	c	K	A_4	A_6	A_8	A_{10}
Surf1	114	5.44×10^{-3}	0	-4.32×10^{-7}	-4.07×10^{-11}	-9.43×10^{-15}	-3.75×10^{-18}
Surf3	108	1.28×10^{-2}	0	1.59×10^{-6}	-4.10×10^{-10}	6.90×10^{-14}	-3.22×10^{-18}
Surf4	108	-1.30×10^{-2}	0	1.13×10^{-6}	-3.82×10^{-10}	6.45×10^{-14}	-4.80×10^{-18}
Surf12	72	-3.28×10^{-3}	0	-2.05×10^{-6}	1.62×10^{-10}	-7.65×10^{-15}	6.28×10^{-20}
Surf13	72	-5.45×10^{-3}	0	-1.17×10^{-6}	-6.40×10^{-11}	3.56×10^{-13}	-2.24×10^{-16}

Table 8.3: Prescriptions of the selected aspheric surfaces from Figure 8.7

a Schmidt plate. The optical prescriptions are tabulated in Table 8.3. Firstly, general types of concave and convex aspheric surfaces (Surf3, Surf4, Surf12, Surf13) are investigated, followed by the case of Schmidt plate (Surf1).

The aspheres are chosen so that comparison among them is more practical with similar workpiece diameters, rather than large range of sizes used previously in Figure 8.3.

In Figure 8.8, the general types of asphere profiles (Surf3, Surf4, Surf12, and Surf13) are shown with the profiles of the minimum volume spheres calculated by using this method, as well as the deviations. For each asphere, starting from the radius of curvature at the vertex as the radius of the sphere, minimum volume between the sphere and asphere was numerically calculated.

In Surf1 (counting from the left) which is the Schmidt plate, with workpiece size of ⌀114 mm, the vertex height at the convex centre is slightly higher than that at the edge, and so a convex envelope sphere is calculated. As pointed out earlier,

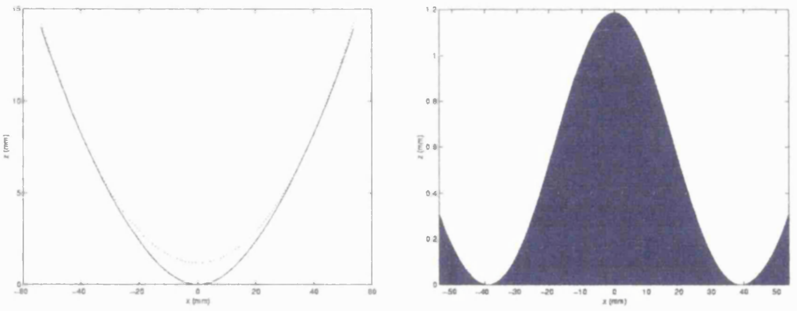

(a)Surf3 profiles (b)Surf3 deviation

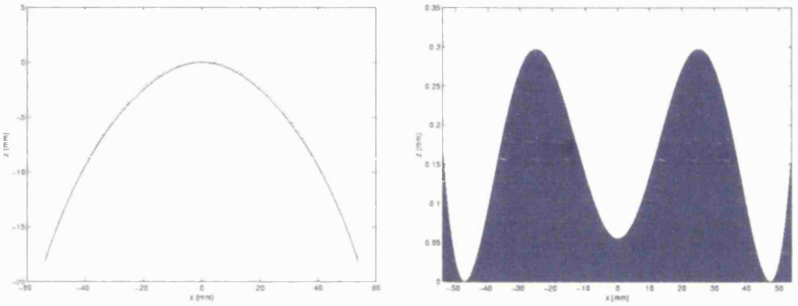

(c)Surf4 profiles (d)Surf4 deviation

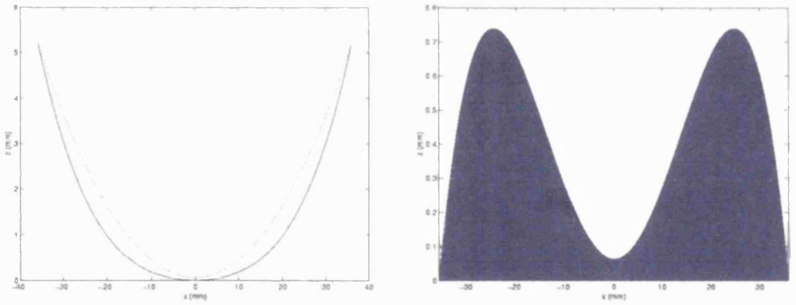

(e)Surf12 profiles (f)Surf12 deviation

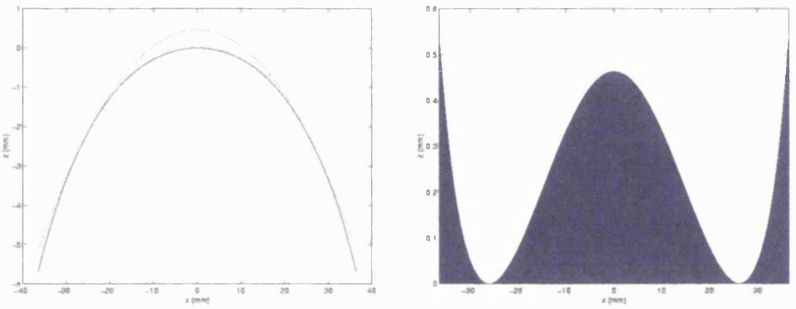

(g)Surf13 profiles (h)Surf13 deviation

Figure 8.8: General types of aspheres (solid in left column) from Figure 8.7 with the minimum volume spheres (dotted in left column), and deviations (area in right column

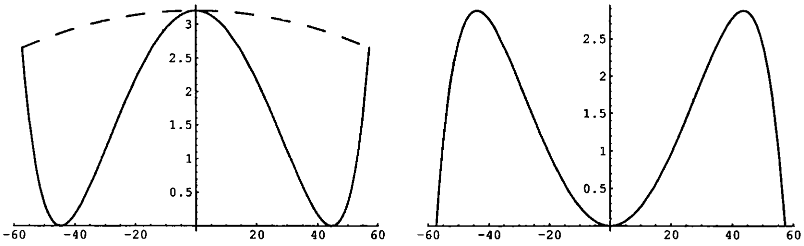

(a)Surf1 profiles (b)Surf1 deviation

Figure 8.9: (a)Schmidt plate(Surf1, solid) and the envelope sphere(dashed), (b)The deviation between the Schmidt plate and the envelope sphere

for a Schmidt plate, the envelope sphere is the minimum volume sphere, thus the volumetric index of manufacturability can be directly solved without using the numerical method developed. With the new volumetric index for spinning compliant tool, not only can it be clearly defined for a Schmidt plate, but in fact it becomes easier to calculate the volumetric index of manufacturability than to calculate the indices of general types of aspheres.

Surf1 and the initial envelope sphere are illustrated in Figure 8.9 (a). The deviation (envelope sphere - Surf1) is showed in Figure 8.9 (b).

By revolving the deviations around the z-axis, the volume to be removed, or volumetric manufacturability index V for each asphere of Figure 8.7 is calculated as in Table 8.4.

It should be notice that a asphere which has smaller maximum deviation to be removed does not guarantee smaller solid of revolution *volume* to be removed. For example, Surf13 has larger deviation to be removed (Figure 8.7 (h)) than that of Surf4 (Figure 8.7 (h)), but has the smaller volume to be removed. Regarding the revolution around the z-axis, large deviation near the edge gives larger volume than the same deviation near the z-axis.

Table 8.4 successfully compares the volumetric index of manufacturability including that of the Schmidt plate (Surf1). It shows that the volumes to be removed are in descending order of Surf1, Surf3, Surf12, Surf4, and Surf13.

If the volumetric material removal rate, or the influence function of a spinning compliant tool is given to polish these aspheres, the polishing time for each asphere can estimated. For example, Figure 8.10 shows the volume ($1.7\times10^7 \mu m^3$) of the removed

	V mm^3	R (mm)	TPT(min)	Type
Surf1	1.9573E+004	2980.25	5.76E+05	Schmidt
Surf3	2.0646E+003	116.9326	6.07E+04	CNCV
Surf4	1.2734E+003	-89.5107	3.75E+04	CNVX
Surf12	2.0310E+003	128.0512	5.97E+04	CNCV
Surf13	650.4719	-121.0613	1.91E+04	CNVX

Table 8.4: Volumetric indices of manufacturability and radii of minimum volume spheres for aspheres of Figure 8.7

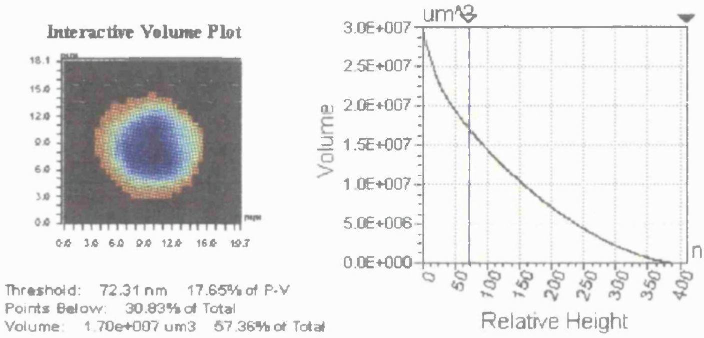

Threshold: 72.31 nm 17.65% of P-V
Points Below: 30.83% of Total
Volume: 1.70e+007 um3 57.36% of Total

Figure 8.10: Volume of the 3D influence function of the spinning compliant tool

material from Figure 7.3, which was used for the influence function measurement with the spinning compliant tool in the last chapter. Since the total polishing time was 30 seconds, it converts to 3.4×10^{-2} mm^3/min.

Consider a case when BK7 lenses with the above aspheric designs of Table 8.3. The total polishing time (TPT) values in Table 8.4 are obtained by using the above influence function from Figure 8.10, which naturally are in the same order as the volumetric index values. The required total polishing times are seemingly impractical, due to the extremely large asphericities. Since the lenses have severe asphericities and they are very thin, perhaps these are why the lenses comprised of the above surfaces are made in plastic for mass production by moulding. Conversely, the development of spinning compliant tools with even higher influence functions can be an incentive to using such severe aspherics made of glass. Negative figures for R, or the radius of minimum volume sphere indicate convenx surfaces. Table 8.4 also indicates that the back surfaces of meniscus lenses (Surf3-Surf4, Surf12-Surf13), which are convex aspheric surfaces are significantly simpler to manufacture than the corresponding concave front surfaces. The fact that similar aspheric profiles of different concavity result in such difference in manufacturing time shows another advantage of the volumetric index of manufacturability. With Foreman's method, the exactly same aspheric profiles with the opposite concavity would result in the identical manufacturability.

8.7 Conclusion and future work

As investigated in the previous chapters, with the advent of possible usage of spinning compliant tools for aspheric polishing, a method to measure the difficulty involved in polishing aspheres with this kind of tool was proposed in this chapter.

Starting from the inherent limits of the Foreman's [28] index of manufacturability for aspheric polishing, a volumetric index of manufacturability was proposed as an alternative method to measure the mafacturability in polishing aspheres. The Foreman's hypothesis: "the difficulty lies in the degree of change of the radius of curvature of the asphere" had been required for pitch tool polishing. However, for a spinning compliant tool, it is no longer bound to the hypothesis thanks to the compliant nature of the tool. Therefore, the volume to be removed from an initial surface was defined as the volumetric index of manufacturability.

In order to minimise the production time, the volume to be removed needs to be minimsed. A numerical method to calculate the volume to be removed, and to minimise it for an axially symmetric asphere was developed. This method was applied to different kinds of aspheres including general concave and convex aspheres, and a Schmidt plate. It was demonstrated that the newly proposed volumetric index of manufacturability was intuitively well defined for all the asphere samples, in contrast to Foreman's method.

As for the future work, the volumetric index of manufacturability could be extended for non-axially symmetric aspheric surfaces such as off-axis paraboloids, toroids, and saddle-shaped aspheres to be polished with spinning compliant tools.

In order to apply the same volumetric material removal rate, the future CCPM also has to provide continuous tilt control of the spinning compliant tool, so that the tool

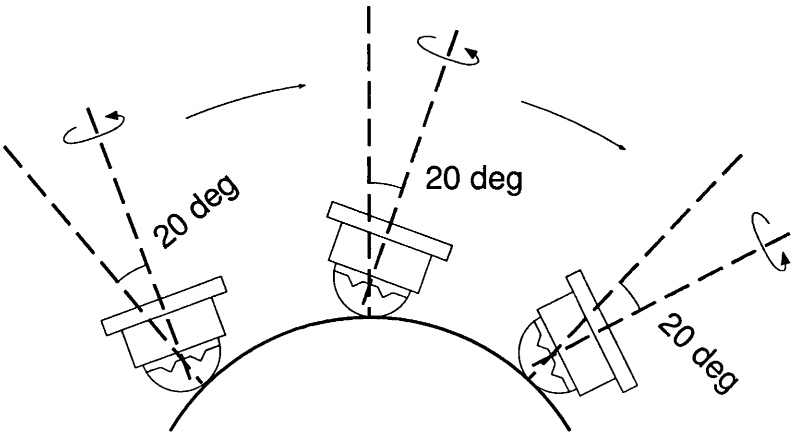

Figure 8.11: A spinning compliant tool always tilted 20° against the surface normal at any point on a concave asphere

spinning axis is tilted with the same angle against the workpiece surface anywhere on a workpiece. Figure 8.11 shows an example of spinning compliant tool always tilted 20° against the surface normal, sweeping on a concave asphere. In case of non-symmetrical aspheric surfaces, the tilt should be controlled in two directions.

If the volumetric removal rate and the cost of machining time using a spinning compliant tool can be defined, the volumetric index of manufacturability can also lead to production cost information for an asphere.

Chapter 9

Conclusion and future work

The approaches described in this thesis presented both theoretical and empirical ground for the development of economical manufacturing technique of aspheric optics. Three key areas of the work reported are as follows.

Firstly, the material removal characteristic was investigated with the active pressure servo mode pitch tool polishing. Pitch is still one of the most widely used polishing tool for high precision optics. With the help of a computer-controlled polishing machine, the relationship between the depth removal rate and some polishing parameters in pitch tool polishing was investigated. A small (20 mm) sub-diameter tool for polishing aspheric optics was used as the pitch tool. Among the various factors influencing the polishing, tool pressure and speed were systematically controlled by a CCPM. Particularly, the polishing pressure was actively monitored and controlled by the CCPM. Two empirical equations, which are the modified versions of the Preston's equation for predicting material removal rate, were presented for polishing a glass ceramic called Astrositall. An indeterministic process by nature, as it is known, the factor of 2.6 was observed between the maximum and the minimum material removal rate measured over the iterative polishing experiments with the identical tool pressure and speed parameters. Assuming the improvement factor is the characteristic uncertainty, the result of the experiment implies that the surface can be polished with at least 38% of an expected material removal, although this is for a point polishing rather than over an area. For the future research, an extensive database needs to be built empirically to understand the material removal characteristics of different materials.

Secondly, the OSL's novel approach using an spinning compliant tool to manufacture small aspheric surfaces was demonstrated. The advantages of spinning compliant polishing for aspheric surfaces are conformality and high removal rate due to the air/liquid-filled compliant material and the fast spinning of the tool. With the various spinning RPM of spinning compliant tools, two different pressures, and different precession angles, the surface texture of polished surface were investigated. The surface textures were observed to be comparable to those of near pitch tool polished surfaces regardless of the polishing parameters, which implies faster tool spinning RPM can be used without degradating the surface roughness quality. The implication of precessing a spinning compliant tool was also reported. A surface texture simulator based on a statistical model was developed and it was used to predict the influence of different types of precession on surface texture, which was confirmed by experiments.

A deconvolution algorithm was developed and applied for the spinning compliant tool polishing/figuring and used to predict the integrated dwell time, and thus the result surface. This experiment demonstrated a feasibility of rapid production of aspheric surfaces with near pitch tool polishing surface roughness.

For the future research, higher positioning accuracy is required for the spinning compliant tool polishing and automated continuous sweeping will enhance the speed of the over all aspheric polishing process. With an extension of the dwell time calculation to the whole area of a workpiece, the spinning compliant tool polishing technique can be used to polish non-rotationally symmetric aspheric surfaces. Development of a *compliant* bound-abrasive of various grade would be beneficial towards cost-effective spinning compliant tool polishing, with which one CCPM can be also used as a grinding machine. For the ultimate future work, an spinning compliant tool and CCPM which can run in active pressure servo mode are required to rapidly converge to a target aspheric surface.

Finally, a novel index of manufacturability for polishing aspheric surfaces was proposed, which can be used with spinning compliant tool polishing. The material removal in pitch tool polishing has been a time-consuming process. Particularly polishing an aspheric surface, whose radius of curvature varies over the radius of the surface, requires sub-diameter tools due to the hardness of the pitch. When polishing an asphere with a pitch tool, the more variant the radius of curvature of the aspheric design is, the smaller the tool size is required. The smaller the tool size is, the longer it takes to polish the surface, with the higher manufacturing costs. The enhanced index of manufacturability proposed in this thesis can be a useful relative reference for the pre-manufacture stage. Among similar aspheric designs, the index of manufacturability can tell which is more difficult, thus expensive to manufacture. The work in this thesis starts from the limitation of an existing index of manufacuturability to encompass wider range of aspheric designs.

If the work of this thesis could have been started again, a sufficient number of flat surfaces for initial surfaces of polishing experiments, or a planarisation machine to produce flats readily should be provided as a lot of sweat and time were spent for the sample preparations. For the active servo mode pitch polishing, the deconvolution method used in the spinning compliant tool polishing would have been used to polish an area rather than a single groove. For the work on spinning compliant tool polishing experiment, a development of an up-right polishing head with horizontal spinning axis of the complaint material would have made the tool speed calculation and positioning work much easier.

Continuous research on development of more cost-effective method of aspheric production are being continuously carried out world-wide. Since the author started this work in September 1995, for instance, the MRF aspheric polishing technique of COM was commercialised with impressive performances. Deterministic grinding techniques also have progressed, now there are prototype asphere or conformal[62] optics grinding machines are being introduced.[81] Traditionally, polishing and figuring started from the best-fit sphere of the target design, but with an asphere or conformal grinding machine, which should reduce the polishing and figuring time. Currently, at least typically 4-5 times of cost difference exist between an asphere comparable to a sphere.[20] It is hoped that with the progress of manufacturing techniques such as the spinning compliant tool demonstrated in this thesis, affordable aspheric surfaces can be used more widely in optical instruments. The question at the beginning of this thesis “why aspherics?” perhaps should be changed to “why not aspherics?”

Appendix A

Comprehensive material removal rate data of the pitch tool polishing

Table A.1, A.2, and A.3 show the comprehensive results from the polishing experiments set A, B, and C respectively. For each polishing run material removal rates of eight(four for set A) positions were collected around the groove as shown in Figure 3.8. The averaged values are shown in Table A.1, A.2, and A.3.

		Pressure(N/mm^2)			
		0.06	0.08	0.1	0.12
	25	1.04	1.17	1.60	2.54
Speed	50	1.92	1.83	3.19	3.06
(mm/s)	75	1.79	2.53	4.32	3.72
	100	3.14	3.98	4.24	4.08

Table A.1: Measured material removal rate (nm/s) for experiment set A

		Pressure(N/mm^2)			
		0.067	0.089	0.11	0.13
	25	1.90	3.29	4.39	5.39
Speed	50	3.75	5.83	6.83	9.96
(mm/s)	75	5.76	8.00	10.02	13.07
	100	7.90	11.33	14.76	19.97

Table A.2: Measured material removal rate (nm/s) for experiment set B

		Pressure(N/mm^2)			
		0.06	0.08	0.1	0.12
	25	1.14	1.47	1.56	2.98
Speed	50	1.48	3.88	4.89	5.36
(mm/s)	75	6.18	5.61	5.40	8.10
	100	5.90	7.44	9.01	11.22

Table A.3: Measured material removal rate (nm/s) for experiment set C

Appendix B

Velocity vector calculation of a tilted spinning tool

The geometry of the speed calculation of a tilted spinning tool from chapter 5 is presented and the speed components are derived.

Redrawn from Figure 4.10, Figure B.1 shows the detailed geometry of a spinning tool with a tilted axis, pressed on a flat surface.

In Figure B.1, $h = \sqrt{R^2 - r^2}$, where R is the radius of the sphere, $\varphi = \pi/2 - \theta$, $\rho = (h \tan\theta + x) \sin\phi$, where $-r \leq x \leq r$.

From Figure B.1, the footprint can be drawn as in Figure B.2. The arc inside the

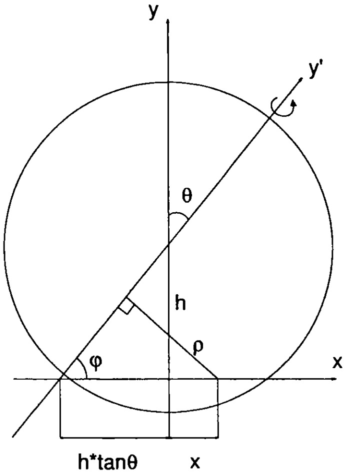

Figure B.1: Tilted spinning tool pressed against a flat surface

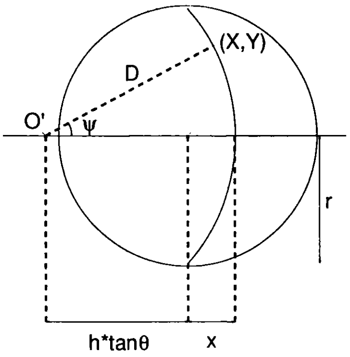

Figure B.2: Footprint of the tilted spinning tool pressed against a flat surface

circular footprint area represents an equi-speed contour. Along the arc, the magnitude of the tool velocity is constant, which is the tangential speed of an effective radius ρ spinning with an angular velocity ω. On the footprint, the arc can be considered as an locus of a radius D, centred at O', rotating with an angular velocity $d\psi/dt$. In fact, the two angular velocity is identical. Therefore, the spinning velocity components can be calculated as follows.

A point on the locus is $X = D\cos\psi, Y = D\sin\psi$, and the spinning velocity components are

$$dX/dt = -D\sin\psi\frac{d\psi}{dt}, \tag{B.1}$$

$$dY/dt = D\cos\psi\frac{d\psi}{dt}, \tag{B.2}$$

thus,

$$v_x = -Y\omega, \tag{B.3}$$

$$v_y = X\omega. \tag{B.4}$$

Appendix C

Integrated dwell time calculation

With a sub-diameter tool is swept on a radius of a workpiece, polishing occurs intermittently. Each time the tool passes a certain point on the workpiece the point is in contact with the tool only for a certain length of time. Integrated dwell time is the summation of all the contact times. With the size of the workpiece and tool, and the RPM of the turntable, the integrated dwell time per one sweep and thus the total integrated dwell time can be calculated.

From the simple geometry as drawn in Figure C.1 it can be calculated as follows. Consider a line between the centre of the workpiece and the centre of the tool.

If a point is in distance D away from the centre of the workpiece, the angle θ can

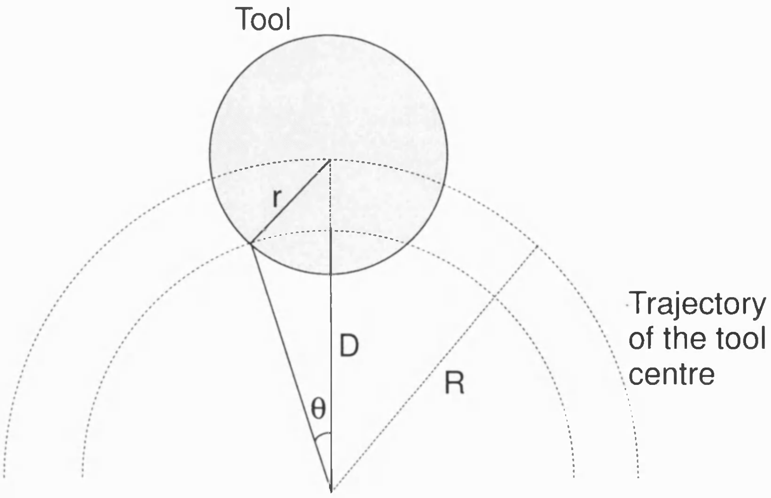

Figure C.1: Diagram of tool path and the arc swept by the tool centre

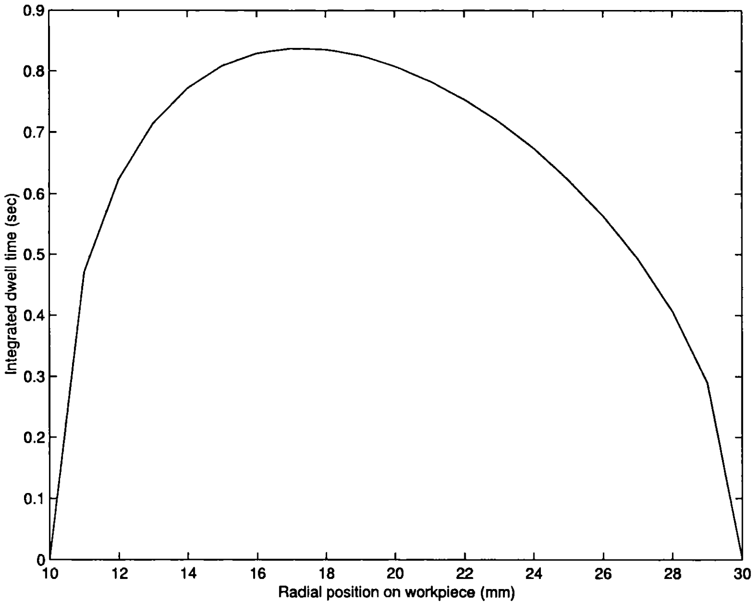

Figure C.2: Example of an integrated dwell time

be found with

$$cos\theta = \frac{D^2 + R^2 - r^2}{2DR}, \tag{C.1}$$

and the dwell time for one pass of the tool (dwell time per revolution of the tool) is

$$t_{one\ sweep} = \frac{\theta}{\pi}\frac{60}{RPM}, \tag{C.2}$$

where T is the period for one rotation of the turntable. Therefore the total integrated dwell time is

$$t_{total} = \frac{\theta}{\pi} \times TPT, \tag{C.3}$$

where TPT is the total polishing time given in seconds.

Figure C.2 shows an example of an integrated dwell time. A ⌀20 mm circular tool is swept once on a workpiece. The tool centre is swept 20 mm away from the workpiece centre, and the workpiece is rotated with 11.9 RPM. The maximum of integrated is slightly inside the centre of the tool as a result of the combination of the path length and tangential speed.

Bibliography

[1] L. N. Allen. Progress in ion figuring large optics. *Proc. SPIE*, 2428:237–247, 1995.

[2] D. Anderson, H. Martin, et al. Rapid fabrication strategies for primary and secondary mirrors atSteward observatory mirror laboratory. *Proc. SPIE*, 2199:199–210, 1994.

[3] T. Aquilina. Characterization of molded glass and plastic aspheric lenses. *Proc. SPIE*, 896:167–170, 1988.

[4] J. R. Barber. *Elasticity.* Kluwer Academic Publishers, 1993.

[5] B. V. Barlow. *The Astronomical Telescope.* Wykeham publications, 1975.

[6] I. Birch. Verbal communications. Dept. of Podiatry, Leaf Hospital, Univ. of Brighton (Eastbourne), 1998.

[7] D. Boning, W. Moyne, T. Smith, et al. Run by run control of chemical-mechanical polishing. In *IEEE/CHMT International Electronics Manufacturing Technology Symposium*, 1995.

[8] J. D. Briers. Best-fit spheres and conics as an aid in the manufacture and testing of diamond-turned aspheric optics. *Optica Acta*, 32:169–178, 1985.

[9] Britannica.com Inc., Britannica Centre, Customer Service Department, 310 S. Michigan Ave., Chicago, IL 60604. Encyclopædia britannica. On Shore scleroscope hardness tester.

[10] D. Brooks. Verbal communications. on fine grinding, 1997.

[11] D. Brooks. Verbal communications. on polishing cloths, 1998.

[12] D. Brooks. Verbal communications. On efficiency of different polishing abrasive compounds, 1998.

[13] D. S. Brown. The application of shearing interferometry to routine optical testing. *Journal of Scientific Instruments*, 32:137–139, 1955.

[14] M. Buijs and K. Korpel-Van Houten. Three-body abrasion of brittle materials as studied by lapping. *Wear*, 166:237–245, 1993.

[15] V. H. Bulsara et al. Polishing and lapping temperatures. *Journal of Tribology - Trans. of the ASME*, 119:163–170, 1997.

[16] V. H. Bulsara et al. Mechanics of polishing. *Trans. of the ASME*, 65:410–416, 1998.

[17] Marc Cayrel, P. Beraud, Jacques Paseri, and E. Dromas. Gemini 8.2-m primary mirror no. 1 polishing. *Proc. SPIE*, 3352:205–215, 1998.

[18] Center for Optics Manufacturing. COM brochure, 1999.

[19] R. Chauhan et al. Role of indentation fracture in free abrasive machining of ceramics. *Wear*, 162-164:246–257, 1993.

[20] Commission of Physical Sciences, Mathematics, and Applications (CPSMA). *Harnessing Light: Optical Science and Engineering for the 21st Century.* National Academy Press, 1998.

[21] M. J. Cumbo et al. Slurry particle size evolution during the polishing of optical glass. *App. Opt.*, 34(19):3743–3755, 1995.

[22] T. W. Drueding et al. Ion beam figuring of small optical components. *Opt. Eng.*, 34(12):3565–3571, 1995.

[23] O. W. Fähnle. *Shaping and Finishing of Aspherical Optical Surfaces.* PhD thesis, Delft University of Technology, 1998.

[24] O. W. Fähnle et al. Determination of the optimum starting surface for the generation of aspherical surfaces of revolution. *App. Opt.*, 36:9112–9114, 1997.

[25] O. W. Fähnle et al. Fluid jet polishing of optical surfaces. *App. Opt.*, 37:6771–6773, 1998.

[26] R. Florence. *The Perfect Machine: Building the Palomar Telescope.* HarperCollins, New York, 1994.

[27] Focus Software Inc., P. O. Box 18228, Tucson, AZ 85731. ZEMAX optical design program user's guide (ver. 8.0), 1999. On the LMS best-fit sphere algorithm in Zemax.

[28] J. W. Foreman, Jr. Simple numerical measure of the manufacturability of aspheric optical surfaces. *App. Opt.*, 25(6):826–827, 1986.

[29] J. W. Foreman, Jr. Mercier's aspheric manufacturability index. *App. Opt.*, 26(22):4711–4712, 1987.

[30] R. Geyl and J. Paseri. Optical polishing of the vlt 8.2 m primary mirrors - a report. *Proc. SPIE*, 2775:476–479, 1996.

[31] B. E. Gillman and S. D. Jacobs. Bound-abrasive polishers for optical glass. *App. Opt.*, 37(16):3498–3505, 1998.

[32] D. Golini. Improve your image with aspheres. *Optics & Photonics News*, 8:41–45, 1997.

[33] D. Golini. Magnetorheological finishing (MRF): A production-ready technology. *Convergence*, 6(2), 1998.

[34] D. Golini et al. Precision optics fabrication using magnetorheological finishing. *Critical Reviews of Optical Science and Technology*, CR67:251–274, 1997.

[35] D. Golini and S. D. Jacobs. Physics of loose abrasive microgrinding. *App. Opt.*, 30(19):2761–2777, 1991.

[36] A. J. Hand. Polishing system takes pressure off making aspheres. *Photonics*, pages 42–43, 1999.

[37] P. Hanke and J. P. Zaenkert. Exploiting the aspheric advantage. *EuroPhotonics*, Autumn:44–45, 1996.

[38] Hitachi Ltd., 6, Kanda-Surugadai 4-chome, Chiyoda-ku, Tokyo 101-8010, Japan. Hitachi SEM s-570.

[39] A. M. Hoff. Basic considerations for injection molding of plastic optics. *Proc. SPIE*, 2600:2–5, 1995.

[40] L. Holland. *The Properties of Glass Surfaces.* Chapman & Hill, 1966.

[41] D. F. Horne. *Optical Production Technology (2nd Ed.).* Adam Hilger, 1983.

[42] L. Hubbard. *New developments in profilometric measurement and testing.* PhD thesis, University of London, 1997.

[43] T. S. Izumitani. Polishing, lapping, and diamond grinding of optical glasses. *Treatise on Materials Science and Technology*, 17, Glass II:155, 1979.

[44] T. S. Izumitani. *Optical Glass.* AIP, 1986.

[45] S. D. Jacobs et al. Magnetorheological finishing: A deterministic process for optics manufacturing. *Proc. SPIE*, 2576:372–382, 1995.

[46] JEOL(Skandinaviska)AB, Vegagatan 19, S-172 34 Sundbyberg, SWEDEN. JEOL SEM JSM-35 CF.

[47] C. Jeynes, K. E. Puttick, et al. Laterally resolved crystalline damage in single-point-diamond-turned silicon. *Nucl. Inst. and Meth. in Phys. Research B*, 118:431–436, 1996.

[48] R. A. Jones. Fabrication of a large, thin, off-axis aspheric mirror. *Opt. Eng.*, 30(12):1962–1968, 1991.

[49] R. A. Jones. Fabrication of a large, thin, off-axis aspheric mirror. *Opt. Eng.*, 33(12):4067–4075, 1994.

[50] H. H. Karow. *Fabrication Methods for Precision Optics.* John Wiley & Sons, 1993.

[51] D. H. Kim. Literature survey on metal mirror. OSL internal report, 1997.

[52] D. H. Kim. Technical report on polishing with various cloths. Technical report, Optical science laboratory, 1998.

[53] J.-D. Kim and S.-R. Nam. Ductile regime grinding of ferrite with variation of grain size by a peizoelectric-driven micropositioning grinding table. *Proc. Instn. Mech. Engrs. Part B*, 211:487–493, 1997.

[54] S.-W. Kim. *Active production of large aspheric optics for astronomy.* PhD thesis, University of London, 1993.

[55] S. W. Kim. Verbal communications. On Small Patched Polishing Cloths on a Spherical Polishing Tool, 1998.

[56] S.-W. Kim. Verbal communications. On Tool RPM for Rotating Compliant Tool Polishing, 1998.

[57] S.-W. Kim, D. D. Walker, et al. OGLP-400 : An innovative computer controlled polishing machine. *Proc. SPIE*, 2775:491–496, 1996.

[58] Y.-S. Kim. *An Improved Geometric Test for Optical Surfaces.* PhD thesis, University of London, 1998.

[59] H. King. *The History of the Telescope.* Griffin, London, 1955.

[60] N. B. Kirk and J. V. Wood. Glass polishing. *British Ceramic Transactions*, 93(1):25–30, 1994.

[61] W. Kordonski et al. Magnetorheological suspension-based finishing technology. *Proc. SPIE*, 3326:527–535, 1998.

[62] E. Kreifeldt. DARPA turns researchers loose on new class of optics. *Optics and photonics news*, Jan. 1997.

[63] F. Laguarta et al. Optical glass polishing by controlled laser surface-heat treatment. *App. Opt.*, 33(27):6508–6513, 1994.

[64] F. Laguarta et al. Laser application for optical glass polishing. *Proc. SPIE*, 2775:603–610, 1996.

[65] J. C. Lambropolous et al. Surface microroughness of opitcal glasses under deterministic microgrinding. *App. Opt.*, 35(22):4448–4462, 1996.

[66] R. Learner. *Astronomy Through the Telescope.* Van Nostrand Reinhold Company, Ontario, 1981.

[67] J.-H. Lee, D.-H. Kim, H.-S. Yang, et al. Report for preliminary design review of SaTReC camera. Technical report, OSL, 1997.

[68] A. J. Leistner et al. Polishing study using teflon and pitch laps to produce flat and supersmooth surfaces. *App. Opt.*, 31(10):1472–1482, 1992.

[69] M. S. Longair. *Alice and the Space Telescope.* Johns Hopkins University Press, 1989.

[70] D. Malacara. *Optical Shop Testing.* John Wiley and Sons, 1978.

[71] H. M. Martin, R. G. Allen, et al. Fabrication and measured quality of the MMT primary mirror. *Proc. SPIE*, 3352:194–204, 1998.

[72] T. S. Mast and J. E. Nelson. Fabrication of large optical surfaces using a combination of polishing and mirror bending. *Proc. SPIE*, 1236:670–681, 1990.

[73] MathWorks, Inc., 3 Apple Hill Drive, Natick, MA 01760-2098. MATLAB 5 user manual, 1999. On 'fminsearch' function for Nelder-Mead simplex algorithm.

[74] J. T. McCann. The design, fabrication, and application of diamond machined null lenses for testing generalized aspheric surfaces. *Proc. SPIE*, 1531:134–146, 1992.

[75] Melles Griot Inc. *Melles Griot Optics Guide*, 1990.

[76] C. Menchaca and D. Malacara. Directional curvatures in a conic surface. *App. Opt.*, 23(19):3258–3260, 1984.

[77] R. Mercier. Holographic testing of aspherical surfaces. *Proc. SPIE*, 136:208–214, 1978.

[78] T. A. Michalske and B. C. Bunker. The fracturing of glass. *Scientific American*, 257:78–85, 1987.

[79] Micromeritics Instrument Corporation, One Micromeritics Drive, Norcross, GA 30093-1877. Sedigraph 5110. Regipol 990's particle size distribution measurement equipment.

[80] J.K. Myler, R.A. Parker, and Harrison. High quality diamond turning. *Proc. SPIE*, 1333:58–79, 1990.

[81] Nanotechnology Systems, LLC, 426A Winchester St., PO Box 605, Keene, NH 03431-0605. Nanotech 500FG, 1999. Brochure for the CNC asphere grinding machine.

[82] I. Newton. *Opticks.* Dover, 1952 (based on 1730 ed.).

[83] OpiPro Systems Inc. 6368 Dean Parkway, Ontario, NY 14519-8939. OptiPro series. CNC optical grinding and polishing machines.

[84] Optical Data Solutions, 350 Fifth Ave. - Suite 3304, New York, NY, 10118-0069. LensView, 1997. Lens design database software.

[85] Optical Generics Ltd. IRP-600, 1996. Computer-Controlled Polishing Machine.

[86] Optical Generics Ltd. Business plan 1999/2004. 1999.

[87] Optical Surface Technologies, 45 Wimbledon Hill Road, London SW19 7LZ. Regipol, 1996. Technical data sheet.

[88] J. A. Powell. Chemomechanical polishing of silicon carbide. *J. Electrochem. Soc.*, 144:L161–L163, 1997.

[89] Precitech, Taylor Hobson LTD.PO Box 36, 2 New Star RoadLeicester, LE49JQ UK. Microform 200. CNC aspheric polishing machine.

[90] F. W. Preston. *Trans. Opt. Soc. London*, 27:181–189, 1925.

[91] F. W. Preston. The theory and design of plate glass polishing machines. *J. Soc. Glass Technol.*, 11:214–256, 1927.

[92] K. E. Puttick et al. Single-point diamond machining of glasses. *Proc. R. Soc. Lond. A*, 426:19–30, 1989.

[93] J. S. Reed. *Principles of Ceramics Processing.* John Wiley and Sons, 1995.

[94] Rhone-Poulenc Chemicals. Safety data sheet for CEROX 1670.

[95] D. W. Richerson. *Modern Ceramic Engineering: Properties, Processing, and Use in Design.* Marcel Dekker, 1992.

[96] J. Ruckman, E. Fess, and D. Van Gee. Contour grinding results on the nanotech 150AG. *Convergence*, 7:1–4, 1999.

[97] S. R. Runnels and L. M. Eyman. Tribology analysis of chemical-mechanical polishing. *J. Electrochem. Soc.*, 141:1698–1701, 1994.

[98] Schott Glas. SCHOTT optical glass, 2000. Catalogue Product Range 2000.

[99] F. G. Shi and B. Zhao. Modeling of chemical-mechanical polishing with soft pads. *Appl. Phys. A*, 67:249–252, 1998.

[100] T. Smith and D. Boning. A self-tuning EWMA controller utilizing artificial neural network function approximation techniques. In *International Electronics Manufacturing Symposium, IEMT '96*, Oct. 1996.

[101] South Bay Technologies Ltd., 1120 Via Callejon, San Clemente, CA 92673. MultiTex.

[102] G. Stix. Faster, smaller, flatter. *Scientific American*, February 1998.

[103] TAYLOR HOBSON LIMITED, 2 New Star Road, PO Box 36, Leicester, LE4 9JQ, UK. *Form Talysurf Opterator's Handbook*, 1989.

[104] TEKSCAN, INC.307 West First StreetS. Boston, MA 02127. F-scan brochure.

[105] M. Tomozawa. Oxide cmp mechanisms. *Solid State Technology*, pages 169–175, 1997.

[106] M. Tubridy. *Reconstruction of the Rosse Six Foot Telescope.* Brosna press, 1998.

[107] F. Twyman. *Prism and lens making (2nd ed.).* Adam Hilger, 1952.

[108] T. W. J. Unti. Best-fit sphere approximation to a general aspheric surface. *App. Opt.*, 5:319–321, 1966.

[109] D. P. Updike and A. Kalnins. Contact pressure between an elasticspherical shell and a rigid plate. *Jrnl. of App. Mech.*, pages 1110–1114, Dec 1972.

[110] D. E. Vandenberg et al. Quantitative evaluation of optical surfaces by means of an improved foucault test approach. *Optical Engineering*, 32:1951–1954, 1993.

[111] S. Vázquea-Montiel et al. The initial sphere in the fabrication of conic surfaces with small focal ratio. *App. Opt.*, 38:7171–7173, 1999.

[112] Veeco Metrology, 2650 East Elvira Road, Tucson, AZ 85706, USA. *WYKO 6000 user manual.*

[113] Veeco Metrology, 2650 East Elvira Road, Tucson, AZ 85706, USA. WYKO IR3 infrared laser interferometer.

[114] Veeco Metrology, 2650 East Elvira Road, Tucson, AZ 85706, USA. *WYKO RST 500 User Manual.*

[115] D. D. Walker. Verbal communications, 1998. On the constant pressure characteristics of balls as compliant polishing tool.

[116] D. D. Walker et al. The production of highly aspheric secondary mirrors using active laps. *Proc. of ESO Conf.*, (42):215–218, 1992.

[117] D. D. Walker et al. Method and apparatus for optical polishing, 1997. World Pat. 9700155.

[118] D. D. Walker, S.-W. Kim, R. G. Bingham, D.-H. Kim, et al. Computer controlled polishing of moderate-sized general asphericsfor instrumentation. *Proc. SPIE*, 3355:947–954, 1998.

[119] W. Wei et al. Method for eliminating the system errors inaspheric surfaces test by using computer-generated holograms. *Proc. SPIE*, 1531:303–311, 1992.

[120] S. C. West et al. Practical design and performance of the stressed-lap polishing tool. *App. Opt.*, 33(34):8094–8100, 1994.

[121] S. C. West et al. Progress at the vatican advanced technology telescope. *Proc. SPIE*, 2871:74–85, 1996.

[122] WYKO, 2650 East Elvira Road, Tucson, AZ 85706, USA. PhaseII, 1992. v4.31.

[123] Y. Xie and B. Bhushan. Effects of particle size, polishing pad and contact pressure in free abrasive polishing. *Wear*, 200:281–295, 1996.

[124] H. Yamada. Prejection lens system for projectors, 1993. US Pat. 5,212,597.

[125] H. S. Yang. *Developments in Stylus Profilometry.* PhD thesis, University College London, 1999.

[126] W. H. Zachariasen. *J. Am. Chem. Soc.*, 54:3841–3851, 1932.

Acknowledgements

I wish to thank "once again" all the people who have supported this work, directly and indirectly. The foremost and utmost thanks go to my wife, Hyun Joo Cho - my personal Goddess of encouragement. She was the one incessantly supporting and encouraging me, throughout this aberrated endeavour. Perpetual thanks go to my parents and parents-in-law, for their absolute trust and support throughout this study. Without the love and encouragement of my family, this thesis could never have seen the light.

My sincere and deep thanks go to Prof. S. D. Choi, the founder and the former director of SaTReC in KAIST, who initiated the project and granted me the opportunity to pursue my Ph.D. at OSL in UCL. Special acknowledgement must also go to SaTReC for the financial support of my tuition fees and living expenses throughout the study.

Bona fide thanks to Dr. D. D. Walker, my primary supervisor, who is the director of OSL and co-founder of OGL. He guided me to research aspheric optics manufacturing. His encouragements always awakened me whenever I had to confront the unexpected difficulties in doing this research, and his insights both in the research and business let me "see the wood out of the trees." I must also deeply thank my secondary supervisor Dr. S.-W. Kim, then the head of research and development division at OGL, who vigorously guided me day by day during the most of the research. It was Dr. Kim who showed me the diligent and thorough approaches to the subject of the thesis. He had done so much work on the subject, and his work provided me the guideline to my own work. I also thank Dr. R. G. Bingham, the co-founder of OSL, for the comments and discussions on my work, help on spinning compliant tools and the relevant references.

I also thank Dr. Y.-S. Kim, formerly the OSL member, for his kind support not only for study but also for many other things throughout our staying. I can not miss out the more-than-comradeship and the shower of help from Dr. H. S. Yang, Dr. E.-E. Kim, and Dr. J. H. Lee, who are ex-members at OSL.

I am also much obliged to D. Brooks, the master optician at OSL. Countless practical help on A-to-Z of optical manufacturing techniques he spared me despite the annoyance I often caused. Dr. H. Jamshidi and G. Nixon of OSL also gave me invaluable help on the construction and repair of the electronics for the experiments. Many thanks to T. Savidge, Dr. A. Charalambous, and the rest of the mechanical design office people, who spared the numerous tips on mechanical drawing, and some humour. I am also grateful to Dr. F. Diego, Dr. P. D'Arrigo, Dr. P. Doel, and R. Howes and other OSL colleagues for the great colleagueship.

I would also like to thank Prof. T. Rehren and the staffs of Institute of Archaeology for kindly letting me use the SEM, and P. Hinder of Optical Surface Technologies for the supply of the abrasive slurry with custom data.

Finally but not the least, I would like to thank all the other SaTReC members and the compatriots of the UCL Union Korean Society who shared the precious moments with my wife and me in London, for their kindness throughout my study.